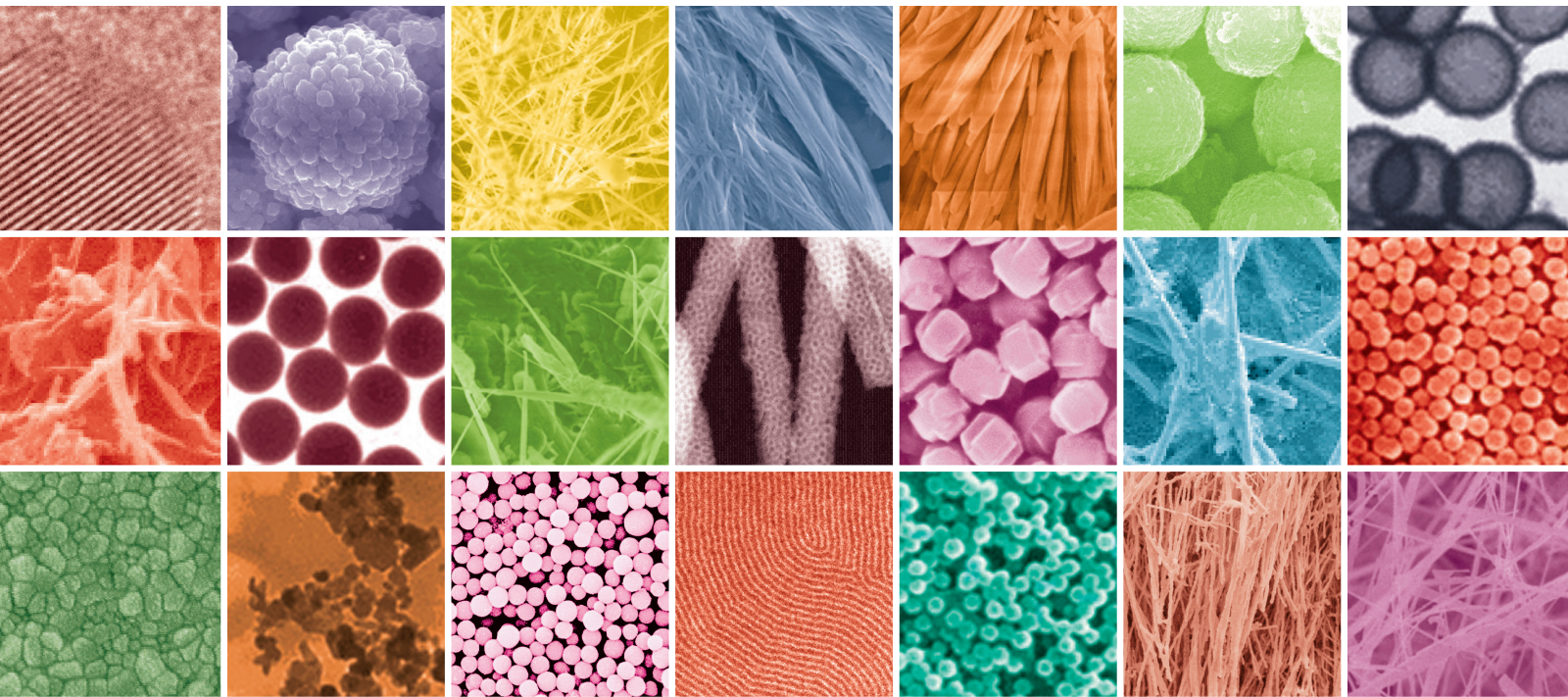


Nanomaterials for Renewable Energy

Guest Editors: Shimou Chen, Liang Li, Hanwen Sun, Jian Sun,
and Baowang Lu





Nanomaterials for Renewable Energy

Journal of Nanomaterials

Nanomaterials for Renewable Energy

Guest Editors: Shimou Chen, Liang Li, Hanwen Sun,
Jian Sun, and Baowang Lu



Copyright © 2015 Hindawi Publishing Corporation. All rights reserved.

This is a special issue published in "Journal of Nanomaterials." All articles are open access articles distributed under the Creative Commons Attribution License, which permits unrestricted use, distribution, and reproduction in any medium, provided the original work is properly cited.

Editorial Board

- Domenico Acierno, Italy
Katerina Aifantis, USA
Sheikh Akbar, USA
Nageh K. Allam, USA
Margarida Amaral, Portugal
Jordi Arbiol, Spain
Raul Arenal, Spain
Ilaria Armentano, Italy
Lavinia Balan, France
Thierry Baron, France
Andrew R. Barron, USA
Hongbin Bei, USA
Stefano Bellucci, Italy
Enrico Bergamaschi, Italy
D. Bhattacharyya, New Zealand
Giovanni Bongiovanni, Italy
Theodorian Borca-Tasciuc, USA
Mohamed Bououdina, Bahrain
Torsten Brezesinski, Germany
C. Jeffrey Brinker, USA
Christian Brosseau, France
Yibing Cai, China
Chuanbao Cao, China
Victor M. Castaño, Mexico
Albano Cavaleiro, Portugal
Bhanu P. S. Chauhan, USA
Yuan Chen, Singapore
Wei Chen, China
Tupei Chen, Singapore
Shafiul Chowdhury, USA
Kwang-Leong Choy, UK
Jin-Ho Choy, Korea
Yu-Lun Chueh, Taiwan
Elisabetta Comini, Italy
Giuseppe Compagnini, Italy
David Cornu, France
Miguel A. Correa-Duarte, Spain
P. Davide Cozzoli, Italy
Majid Darroudi, Iran
Shadi A. Dayeh, USA
Luca Deseri, USA
Yong Ding, USA
Bin Dong, China
Zehra Durmus, Turkey
Joydeep Dutta, Oman
- Ali Eftekhari, USA
Samy El-Shall, USA
Farid El-Tantawy, Egypt
Ovidiu Ersen, France
Claude Estournès, France
Andrea Falqui, Saudi Arabia
Xiaosheng Fang, China
Bo Feng, China
Matteo Ferroni, Italy
Wolfgang Fritzsche, Germany
Alan Fuchs, USA
Peng Gao, China
Miguel A. Garcia, Spain
Siddhartha Ghosh, Singapore
P. K. Giri, India
Russell E. Gorga, USA
Jihua Gou, USA
Alexander Govorov, USA
Jean M. Greneche, France
Changzhi Gu, China
Lin Guo, China
John Zhanhu Guo, USA
Smrati Gupta, Germany
Kimberly Hamad-Schifferli, USA
Michael Harris, USA
Jr-Hau He, Taiwan
Nguyen D. Hoa, Vietnam
Michael Z. Hu, USA
Shaoming Huang, China
Nay Ming Huang, Malaysia
Qing Huang, China
David Hui, USA
Zafar Iqbal, USA
Balachandran Jeyadevan, Japan
Xin Jiang, Germany
Rakesh Joshi, Australia
Myung-Hwa Jung, Korea
Jeong-won Kang, Korea
Hassan Karimi-Maleh, Iran
Antonios Kelarakis, UK
Alireza Khataee, Iran
Ali Khorsand Zak, Iran
Dojin Kim, Korea
Wonbaek Kim, Korea
Philippe Knauth, France
- Ralph Krupke, Germany
Christian Kübel, Germany
Sanjeev Kumar, India
Sushil Kumar, India
Prashant Kumar, UK
Subrata Kundu, India
Michele Laus, Italy
Eric Le Bourhis, France
Burtrand Lee, USA
Jun Li, Singapore
Meiyong Liao, Japan
Silvia Licoccia, Italy
Wei Lin, USA
Jun Liu, USA
Zainovia Lockman, Malaysia
Songwei Lu, USA
Jue Lu, USA
Ed Ma, USA
Malik Maaza, South Africa
Lutz Mädler, Germany
Gaurav Mago, USA
Morteza Mahmoudi, Iran
Mohammad A. Malik, UK
Devanesan Mangalaraj, India
Sanjay R. Mathur, Germany
Paulo Cesar Morais, Brazil
Mahendra A. More, India
Paul Munroe, Australia
Jae-Min Myoung, Korea
Rajesh R. Naik, USA
Albert Nasibulin, Russia
Toshiaki Natsuki, Japan
Koichi Niihara, Japan
Sherine Obare, USA
Won-Chun Oh, Republic of Korea
Atsuto Okamoto, Japan
Abdelwahab Omri, Canada
Ungyu Paik, Republic of Korea
Edward A. Payzant, USA
Ton Peijs, UK
Oscar Perales-Pérez, Puerto Rico
Wenxiu Que, China
Peter Reiss, France
Orlando Rojas, USA
Marco Rossi, Italy



Cengiz S. Ozkan, USA
Vladimir Šepelák, Germany
Huaiyu Shao, Japan
Prashant Sharma, USA
Donglu Shi, USA
Bhanu P. Singh, India
Surinder Singh, USA
Vladimir Sivakov, Germany
Yanlin Song, China
Ashok Sood, USA
Marinella Striccoli, Italy
Jing Sun, China
Xuping Sun, Saudi Arabia
Ashok K. Sundramoorthy, USA

Sabine Szunerits, France
Nyan-Hwa Tai, Taiwan
Bo Tan, Canada
Ion Tiginyanu, Moldova
Valeri P. Tolstoy, Russia
Muhammet S. Toprak, Sweden
Ramon Torrecillas, Spain
Takuya Tsuzuki, Australia
Tamer Uyar, Turkey
Bala Vaidhyanathan, UK
Luca Valentini, Italy
Rajender S. Varma, USA
Antonio Villaverde, Spain
Ajayan Vinu, Australia

Shiren Wang, USA
Ruibing Wang, Macau
Yong Wang, USA
Magnus Willander, Sweden
Zhi Li Xiao, USA
Ping Xiao, UK
Yangchuan Xing, USA
Doron Yadlovker, Israel
Piaoping Yang, China
Yoke K. Yap, USA
Ramin Yousefi, Iran
William W. Yu, USA
Kui Yu, Canada
Renyun Zhang, Sweden

Contents

Nanomaterials for Renewable Energy, Shimou Chen, Liang Li, Hanwen Sun, Jian Sun, and Baowang Lu
Volume 2015, Article ID 143697, 2 pages

All-Polymer Solar Cells Based on Fully Conjugated Donor-Acceptor Block Copolymers with Poly(naphthalene bisimide) Acceptor Blocks: Device Performance and Thin Film Morphology, Kazuhiro Nakabayashi and Hideharu Mori
Volume 2015, Article ID 826985, 7 pages

Theoretical Study on Cyclopeptides as the Nanocarriers for Li^+ , Na^+ , K^+ and F^- , Cl^- , Br^- , Lili Liu and Shimou Chen
Volume 2015, Article ID 276191, 7 pages

Influence of Nanocomposites of LDPE Doped with Nano-MgO by Different Preparing Methods on Its Dielectric Properties, Wenlong Zhang, Yajie Dai, Hong Zhao, and Lidong Zhong
Volume 2015, Article ID 146260, 6 pages

Mussel-Inspired Polydopamine Coated Iron Oxide Nanoparticles for Biomedical Application, Xiangling Gu, Yancong Zhang, Hanwen Sun, Xinfeng Song, Chunhua Fu, and Pingxuan Dong
Volume 2015, Article ID 154592, 12 pages

A Green and Facile Synthesis of Carbon-Incorporated Co_3O_4 Nanoparticles and Their Photocatalytic Activity for Hydrogen Evolution, Libo Gao, Jiangtao Diwu, Qiang Zhang, Hongyan Xu, Xiujian Chou, Jun Tang, and Chenyang Xue
Volume 2015, Article ID 618492, 7 pages

Study of Phase Change Materials Applied to CPV Receivers, Zun-Hao Shih, Ke-Jen Chain, and Hwen-Fen Hong
Volume 2015, Article ID 672328, 5 pages

***Ab Initio* Theoretical Investigation on the Geometrical and Electronic Structures of Gallium Aurides: $\text{GaAu}_n^{0/-}$ and $\text{Ga}_2\text{Au}_n^{0/-}$ ($n = 14$)**, Wen-Zhi Yao, Jian-Bin Yao, and Si-Dian Li
Volume 2015, Article ID 406314, 10 pages

Microstructure and Thermal Properties of Polypropylene/Clay Nanocomposites with $\text{TiCl}_4/\text{MgCl}_2/\text{Clay}$ Compound Catalyst, Limei Wang and Aihua He
Volume 2015, Article ID 591038, 5 pages

Editorial

Nanomaterials for Renewable Energy

Shimou Chen,¹ Liang Li,² Hanwen Sun,³ Jian Sun,⁴ and Baowang Lu⁵

¹*Institute of Process Engineering, Chinese Academy of Sciences, Beijing 100190, China*

²*Department of Physics, Jiangsu Key Laboratory of Thin Films, Soochow University, Suzhou 215006, China*

³*College of Medicine and Nursing, Dezhou University, Dezhou 253023, China*

⁴*Sandia National Laboratories, Livermore, CA 94550, USA*

⁵*Graduate School of Environmental and Life Science, Okayama University, 3-1-1 Tsushima-naka, Kita-ku, Okayama-shi 7008530, Japan*

Correspondence should be addressed to Shimou Chen; chenshimou@ipe.ac.cn

Received 12 May 2015; Accepted 19 May 2015

Copyright © 2015 Shimou Chen et al. This is an open access article distributed under the Creative Commons Attribution License, which permits unrestricted use, distribution, and reproduction in any medium, provided the original work is properly cited.

With demand for sustainable energy, resource, and environment protection, new material technologies are constantly expanding during the last few couple of decades. An intensive attention has been given by the scientific communities. In particular, nanomaterials are increasingly playing an active role either by increasing the efficiency of the energy storage and conversion processes or by improving the device design and performance. This special issue presents recent research advances in various aspects of energy storage technologies, advanced batteries, fuel cells, solar cell, biofuels, and so on. Design and synthesis of novel materials have demonstrated great impact on the utilization of the sustainable energy, which need to solve the increasing shortage of resource and the issues of environmental pollution.

The special issue contains eight papers; the selected topic and the papers are not an exhaustive representation of nanomaterials for renewable energy applications. Nonetheless, they represent a broad range of knowledge on functional nanomaterials in chemistry, physics, biochemistry, materials science, engineering, and so forth, which are very helpful to share with the readers.

A review article titled “Mussel-Inspired Polydopamine Coated Iron Oxide Nanoparticles for Biomedical Application” is authored by X. Gu et al. In this review, the synthesis of iron oxide nanoparticles, the mechanism of dopamine self-oxidation, the interaction between iron oxide and dopamine, the functionality and the safety assessment of dopamine modified iron oxide nanoparticles, and the biomedical application of such nanoparticles are discussed.

The paper titled “A Green and Facile Synthesis of Carbon-Incorporated Co_3O_4 Nanoparticles and Their Photocatalytic Activity for Hydrogen Evolution” is authored by L. Gao et al. They found that the carbon-incorporated Co_3O_4 nanoparticles were able to split pure water into hydrogen under visible light irradiation without any cocatalyst, which is mainly due to the enhanced light absorption behavior. This facile method provided a potential strategy for applying narrow bandgap semiconductors in pure water splitting.

The paper titled “Study of Phase Change Materials Applied to CPV Receivers” is authored by Z.-H. Shih et al. They focused on finding new materials to enhance the thermal spreading and keep the temperature of solar cell as low as possible. They applied electric forward bias on solar cells to simulate the heat contributed from the concentrated sunlight and observed the thermal distribution of these three kinds of thermal spreading materials. Two levels of forward biases were chosen to test the samples and analyze the experiment results.

The paper titled “All-Polymer Solar Cells Based on Fully Conjugated Donor-Acceptor Block Copolymers with Poly(naphthalene bisimide) Acceptor Blocks: Device Performance and Thin Film Morphology” is authored by K. Nakabayashi et al. They fabricated all-polymer solar cells by using poly(3-hexylthiophene) (P3HT) and fully conjugated donor-acceptor (D-A) block copolymer (P3HT-PNBI-P3HT) as donor and acceptor materials, respectively. Atomic force microscopy (AFM) and grazing incidence wide angle X-ray scattering (GIWAXS) analyses reveal that device

performance strongly depends on the P3HT:P3HT-PNBI-P3HT thin film morphology. Their results suggest that P3HT-PNBI-P3HT has the huge potentials for the usage as a nonfullerene acceptor material.

L. Wang and A. He synthesized polypropylene (PP)/clay nanocomposites by in situ intercalative polymerization with $\text{TiCl}_4/\text{MgCl}_2/\text{clay}$ compound catalyst. Their paper is titled "Microstructure and Thermal Properties of Polypropylene/Clay Nanocomposites with $\text{TiCl}_4/\text{MgCl}_2/\text{Clay}$ Compound Catalyst." In this paper, microstructure and thermal properties of PP/clay nanocomposites were studied by FTIR, XRD, TEM, TGA, and DSC, respectively, in detail. They found that clay layers in composites were exfoliated into nanometer size and dispersed uniformly in the PP matrix. The clay can enhance the thermal stability of PP materials efficiently.

W. Zhang et al. reported that when nano-MgO was prepared by the microwave-assisted method, the electric properties of its LDPE nanocomposite were obviously better than those of nano-MgO prepared by traditional heating method. Their paper titled "Influence of Nanocomposites of LDPE Doped with Nano-MgO by Different Preparing Methods on Its Dielectric Properties." In this paper, the influence of nano-MgO on several properties of LDPE nanocomposite was discussed, such as the space charge, volume resistivity as well as DC breakdown strength.

The paper titled "Theoretical Study on Cyclopeptides as the Nanocarriers for Li^+ , Na^+ , K^+ and F^- , Cl^- , Br^- " is reported by L. Liu and S. Chen. The authors designed a series of experiments to compare the different capabilities of the different cyclopeptides in ions transport. The interaction process between a series of cyclopeptide compounds cyclo(gly) n ($n = 4, 6, 8$) and monovalent ions (Li^+ , Na^+ , K^+ , F^- , Cl^- , and Br^-) was studied using theoretical calculations. The mechanism of combination between the cyclo(gly) n and ions was discussed through binding energy, Mulliken electron population, and hydrogen bond.

Another theoretical paper titled "*Ab Initio* Theoretical Investigation on the Geometrical and Electronic Structures of Gallium Aurides: $\text{GaAu}_n^{0/-}$ and $\text{Ga}_2\text{Au}_n^{0/-}$ ($n = 1-4$)" is reported by W.-Z. Yao et al. They found that $\text{GaAu}_n^{0/-}$ ($n = 1-4$) clusters with n -Au terminals and $\text{Ga}_2\text{Au}_n^{0/-}$ ($n = 1-4$) clusters with bridged Au atoms possess geometric structures and bonding patterns similar to those of the corresponding gallium hydrides $\text{GaH}_n^{0/-}$ and $\text{Ga}_2\text{H}_n^{0/-}$. In contrast to the highly symmetric ground states of C_{2v} Ga_2Au , C_{2v} Ga_2Au_2 , and D_{3h} Ga_2Au_3 , C_{3v} Ga_2Au_4 is composed of strong interactions between a Ga^+ cation and the face of a tetrahedral GaAu_4^- anion. The adiabatic and vertical detachment energies of the anions under study are calculated to facilitate their experimental characterization.

Acknowledgments

We would like to thank the authors who have submitted a manuscript to this special issue. Secondly, the fundamental work of all the reviewers of these papers is also very warmly acknowledged. Lastly, the lead editor thanks all the editors for

their contribution in reviewing and assigning reviews for the submitted manuscripts.

Shimou Chen
Liang Li
Hanwen Sun
Jian Sun
Baowang Lu

Research Article

All-Polymer Solar Cells Based on Fully Conjugated Donor-Acceptor Block Copolymers with Poly(naphthalene bisimide) Acceptor Blocks: Device Performance and Thin Film Morphology

Kazuhiro Nakabayashi and Hideharu Mori

Department of Polymer Science and Engineering, Graduate School of Science and Engineering, Yamagata University, 4-3-16 Jonan, Yonezawa 992-8510, Japan

Correspondence should be addressed to Kazuhiro Nakabayashi; nakabayashi.k@yz.yamagata-u.ac.jp

Received 29 August 2014; Revised 24 October 2014; Accepted 29 October 2014

Academic Editor: Shimou Chen

Copyright © 2015 K. Nakabayashi and H. Mori. This is an open access article distributed under the Creative Commons Attribution License, which permits unrestricted use, distribution, and reproduction in any medium, provided the original work is properly cited.

All-polymer solar cells are fabricated by using poly(3-hexylthiophene) (P3HT) and fully conjugated donor-acceptor (D-A) block copolymer (P3HT-PNBI-P3HT) as donor and acceptor materials, respectively. Atomic force microscopy (AFM) and grazing incidence wide angle X-ray scattering (GIWAXS) analyses reveal that device performance strongly depends on the P3HT:P3HT-PNBI-P3HT thin film morphology. Indeed, the π - π stacking nanomorphology rich in the edge-on orientation is formed in the P3HT:P3HT-PNBI-P3HT thin film by optimizing the fabrication conditions, for example, thermal annealing temperature and cast solvent. Consequently, the power conversion efficiency (PCE) of 1.60% is achieved with an open-circuit voltage (V_{oc}) of 0.59 V, short-current (J_{sc}) of 4.43 mA/cm², and fill factor (FF) of 0.61. These results suggest that P3HT-PNBI-P3HT has the huge potential for the usage as a nonfullerene acceptor material.

1. Introduction

Over the last decade, polymer/fullerene organic solar cells (OSCs), in which active layers are composed of polymeric donor and fullerene-based acceptor materials, have been extensively investigated as revolutionary renewable energy sources because of their advantages (e.g., low cost, light weight, flexibility, and facile large scale fabrication) compared to silicon-based solar cells [1–4]. To date, PCEs of around 10% have been achieved in OSCs [5], mainly through the development of various specialized polymeric donor materials (e.g., low bandgap polymers). However, acceptor materials are, compared to donor materials, far less developed, and the fullerene derivative, [6, 6]-phenyl C₆₁ butyric acid methyl ester (PCBM), is the only conventional acceptor material for OSCs. One of the major reasons using PCBM as an acceptor material in OSCs is its high electron mobility (ca. 0.002 cm²/V·s) [6]. On the other hand, there are considerable

drawbacks for the use of PCBM in OSCs: (i) negligible light absorption in the visible-near IR regions, (ii) relatively poor photochemical and chemical stability, (iii) low miscibility with donor polymeric materials, and (iv) high cost for synthesis and purification. In recent years, high-performance OSCs, which depend on the development of polymeric donor materials, have reached a critical limit. To resolve the current situation, novel acceptor materials other than fullerene-based materials are necessary; in this regard, polymer/polymer OSCs based on nonfullerene polymeric acceptor materials, the so-called all-polymer solar cells, are receiving increased attention [7–12]. Regardless of such attention, the PCEs of all-polymer solar cells reported in many previous studies are quite low compared to fullerene-based OSCs [13–15]. Thus, further development of specialized acceptor materials for OSCs is imperative for realizing high-performance all-polymer solar cells. For example, arylene bisimide-based, for example, naphthalene bisimide (NBI) and perylene

bisimide-based, acceptor materials are considered to be promising candidates because of their high stability, excellent acceptor properties due to well-placed LUMO levels, and high electron mobilities [16–23]. Indeed, several all-polymer solar cells based on those acceptor materials accomplished excellent PCEs (2–4%) [20–24].

In previous work, we developed a novel fully conjugated D-A block copolymer with NBI-based acceptor blocks (P3HT-PNBI-P3HT) for a nonfullerene acceptor material [16]. The fusion of the fully conjugated D-A structure and NBI-based acceptor blocks provided ideal characteristics for OSC acceptor materials, that is, broad light absorption, favorable LUMO level, good miscibility with P3HT, and so on. Furthermore, the all-polymer solar cell with the P3HT:P3HT-PNBI-P3HT blend active layer achieved a PCE over 1.0%. The previous work is the first example of the use of fully conjugated D-A block copolymers as acceptor materials for all-polymer solar cells, and the obtained device performances demonstrated that the fully conjugated D-A block copolymer, P3HT-PNBI-P3HT, had a potential to serve as a nonfullerene acceptor material.

Toward the higher performance of all-polymer solar cells based on fully conjugated D-A block copolymers, we herein investigated the in-depth relationship between device performance and thin film morphology in the P3HT:P3HT-PNBI-P3HT blend active layer by a combination of AFM and GIWAXS analyses. By optimizing the device fabrication conditions, the P3HT:P3HT-PNBI-P3HT blend active layer with π - π stacking nanostructure could be prepared, and a PCE as high as 1.60% was achieved.

2. Experimental

2.1. Materials. Fully conjugated D-A block copolymers (P3HT-PNBI-P3HT) were synthesized according to the previous literature [17]. Poly(3-hexylthiophene) (regioregularity = 91–94%, M_w = 50000–70000) was purchased from Rieke Metals, Inc.

2.2. All-Polymer Solar Cell Fabrication and Measurements. The typical procedure of ITO/PEDOT:PSS/P3HT:P3HT-PNBI-P3HT/Ca/Al architecture is as follows: commercially available prepatterned $15 \Omega/\square$ sheet resistance indium tin oxide (ITO) substrates ($2.0 \text{ cm} \times 1.5 \text{ cm}$) were cleaned and plasma-etched. Then poly(3,4-ethylenedioxythiophene):poly(styrenesulfonate) (PEDOT:PSS) aqueous solution (Clevios P VP AI 4083) was spin-coated at 4000 rpm for 40 s and subsequently annealed under flowing nitrogen at 120°C for 10 min. Substrates were allowed to cool under nitrogen atmosphere and then transferred to a glovebox. P3HT:P3HT-PNBI-P3HT blend chlorobenzene solution was spin-coated at 700 rpm for 90 s, and the active layer was annealed for 15 min. The blend solution that 5 mg of each polymer dissolved in 1 mL of chlorobenzene (1:1 by weight, conc. = 10 mg/mL) was prepared in a glovebox. Then the top electrode consisted of Ca interlayer (20 nm) and Al electrode (80 nm) was vacuum-deposited. The J - V characteristics of the devices were measured by using a direct-current voltage

and a current source/monitor (Bunko-Keiki, BSO-X500L) in nitrogen atmosphere under AM1.5G simulated solar light at $100 \text{ mW}/\text{cm}^2$. The light intensity was corrected with a calibrated silicon photodiode reference cell (Bunko-Keiki, BS-520).

3. Results and Discussion

3.1. Performance of All-Polymer Solar Cells with P3HT-PNBI-P3HT. All-polymer solar cells with the P3HT:P3HT-PNBI-P3HT blend active layers were fabricated by using P3HT-PNBI-P3HTs with different molecular weights and compositions of each block (P1 and P2, see Figure 1(a) for details). The device architecture is as follows: ITO/PEDOT:PSS/P3HT:P3HT-PNBI-P3HT (1:1 by weight)/Ca/Al. The device performances are summarized in Table 1. In the P3HT:P1 system, a PCE of 0.50% with V_{oc} of 0.51 V, J_{sc} of $2.12 \text{ mA}/\text{cm}^2$, and FF of 0.47 was obtained without thermal annealing. The PCE gradually improved with an increase in the thermal annealing temperature and finally reached 1.20% with V_{oc} of 0.59 V, J_{sc} of $3.28 \text{ mA}/\text{cm}^2$, and FF of 0.62 when annealed at 200°C (Figure 2(a)). In the P3HT:P2 system, the high PCE of 1.28% was also obtained with thermal annealing at 200°C (V_{oc} of 0.56 V, J_{sc} of $4.57 \text{ mA}/\text{cm}^2$, and FF of 0.50). Furthermore, the best PCE of 1.60% was achieved when using dichlorobenzene (DCB) instead of chlorobenzene (CB) as the cast solvent (Table 1 in Entry 7 and Figure 2(b)). This PCE improvement was attributed to two factors: (1) enhanced light absorption of the P3HT:P3HT-PNBI-P3HT blend film due to thermal annealing (Figure 1(b)) and (2) a significant increase in J_{sc} values. Considering that J_{sc} values are closely related to the thin film morphology with nanoscale, thermal annealing and the cast solvent should lead to morphological changes in the blend active layer, as discussed in many previous works, resulting in the improvement of PCEs [25, 26].

For comparison with the P3HT:P3HT-PNBI-P3HT system, the performance of an all-polymer solar cells with the P3HT:PNBI blend active layer was then evaluated; consequently, the PCE of that cell was 0.49% (the PCE of the P3HT:P3HT-PNBI-P3HT system was 1.60% under the same conditions). Considering that the optical and electrochemical properties of PNBI were almost same as those of P3HT-PNBI-P3HT, the other factor such as the nanomorphology in the P3HT:PNBI blend active layer might cause the quite lower device performance compared to that of the P3HT:P3HT-PNBI-P3HT system (see Figure 3(d) and Figure S1 in Supplementary Material available online at <http://dx.doi.org/10.1155/2014/826985> for details).

3.2. Nanomorphology Observation by AFM Measurement. To understand the difference in the device performance, the surface morphology of the P3HT:P3HT-PNBI-P3HT blend films was investigated by AFM measurements. As depicted in Figures 3(a)–3(c), no significant differences in the sizes of the bright and dark domains were found, regardless of the thermal annealing and cast solvent conditions, whereas the average root-mean-square (rms) roughness tended to be largely dependent on the fabrication conditions. The device

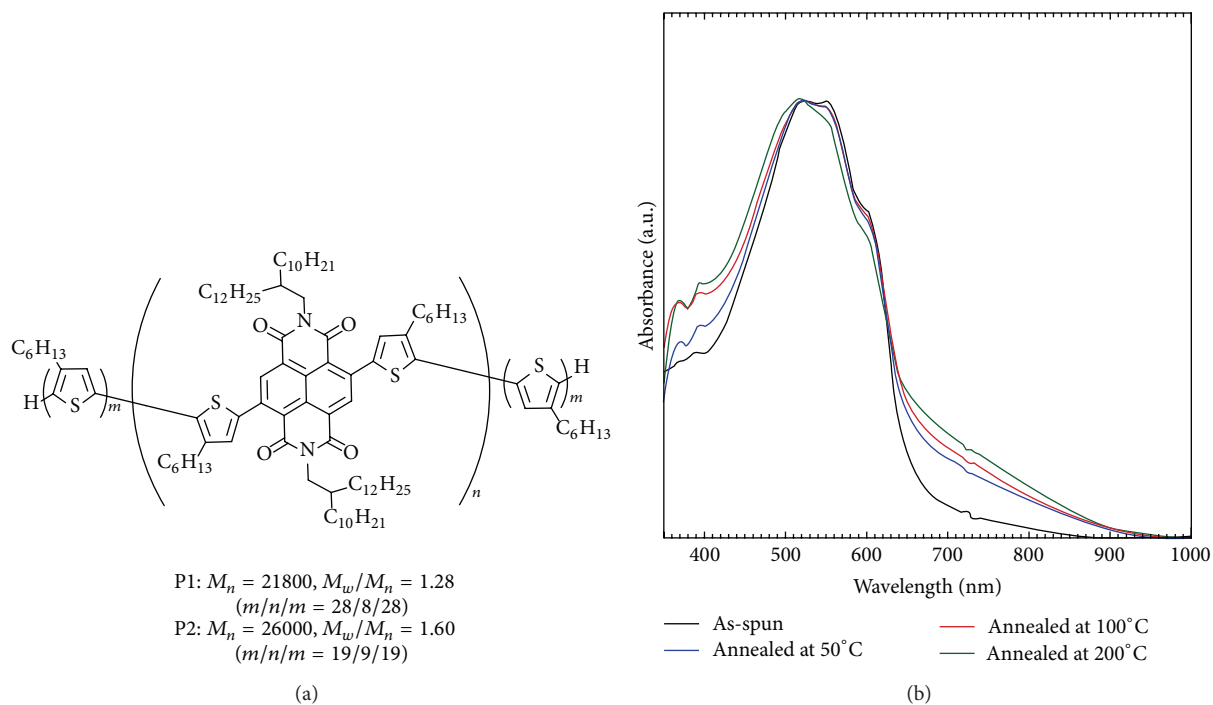


FIGURE 1: (a) Structural information of P3HT-PNBI-P3HT and (b) UV-vis absorption spectra of the P3HT:P1 blend film. The thermal annealing was carried out under nitrogen atmosphere for 30 min.

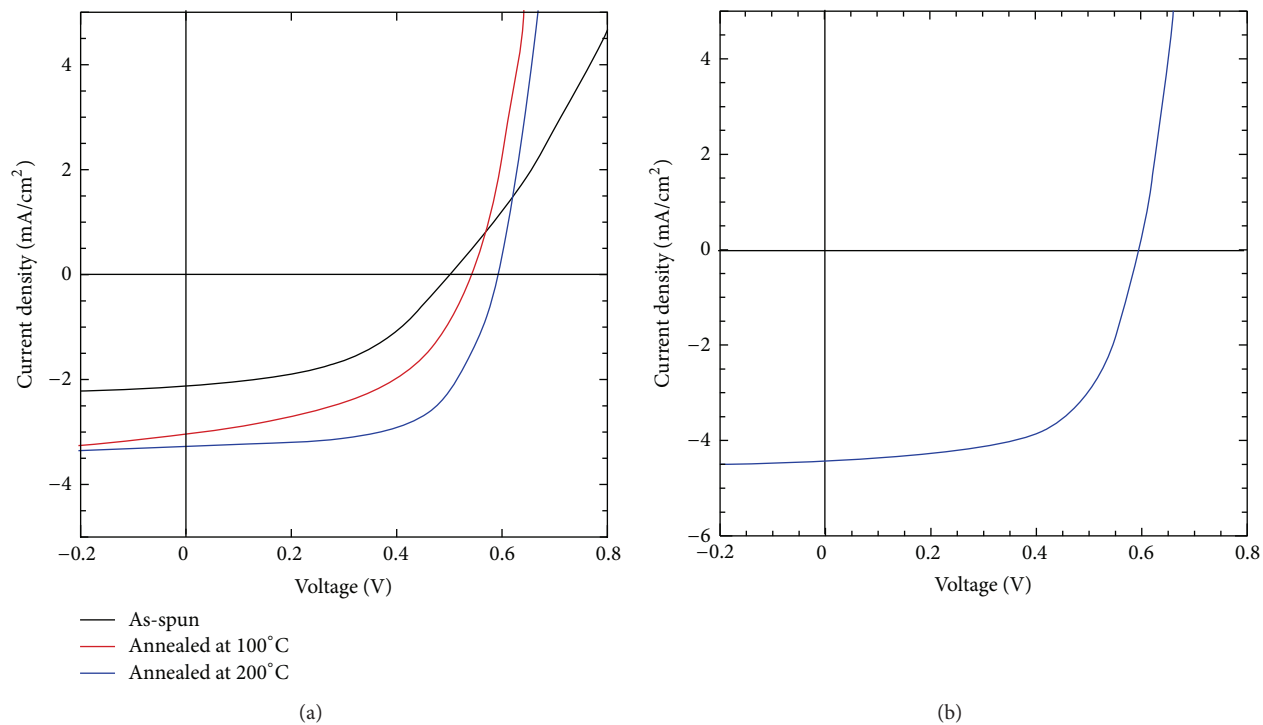


FIGURE 2: J - V characteristics of (a) P3HT:P1 system and (b) highest-performance device with P3HT:P2 system under AM1.5G (100 mW/cm²) illumination.

TABLE 1: Results of device performance.

| Entry | Compositions ^a | Conditions (solvent/annealing temperature) ^{b,c} | V_{oc} (V) | J_{sc} (mA/cm ²) | FF | PCE (%) ^d |
|-------|---------------------------|--|--------------|--------------------------------|------|----------------------|
| 1 | P3HT:P1 | CB/as-spun | 0.51 | 2.12 | 0.47 | 0.50 |
| 2 | | CB/100°C | 0.54 | 3.03 | 0.48 | 0.79 |
| 3 | | CB/200°C | 0.59 | 3.28 | 0.62 | 1.20 |
| 4 | P3HT:P2 | CB/as-spun | 0.49 | 1.60 | 0.47 | 0.37 |
| 5 | | CB/100°C | 0.53 | 3.53 | 0.39 | 0.74 |
| 6 | | CB/200°C | 0.56 | 4.57 | 0.50 | 1.28 |
| 7 | | DCB/200°C | 0.59 | 4.43 | 0.61 | 1.60 |

^a1:1 by weight. ^bCB: chlorobenzene; DCB: *o*-dichlorobenzene. ^cThermal annealing was carried out under nitrogen atmosphere for 30 minutes. ^dAverage values of eight devices.

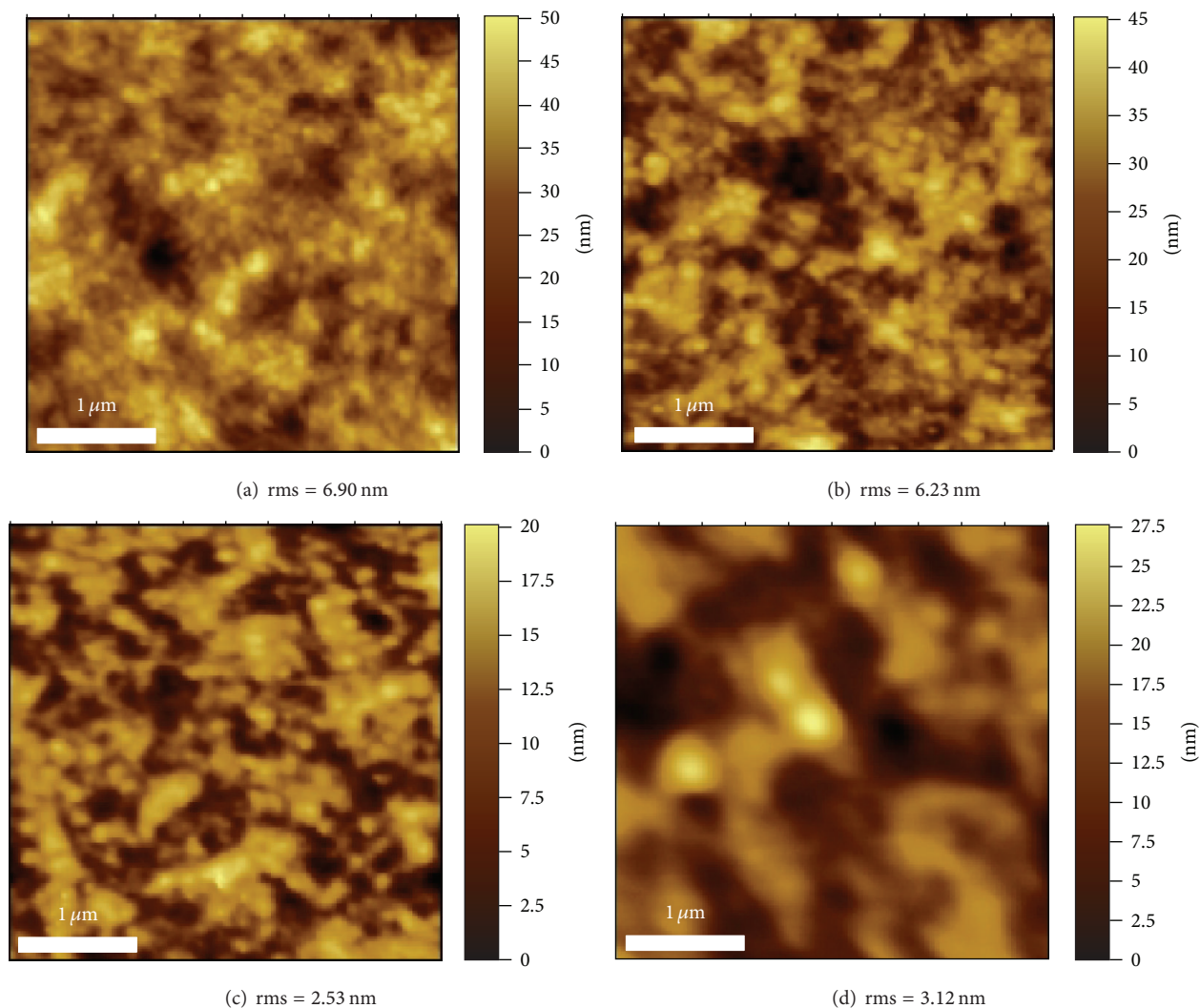


FIGURE 3: AFM height images of P3HT:P2 ((a) Entry 4, (b) Entry 6, and (c) Entry 7 in Table 1) and (d) P3HT:PNBI blend thin films (3 μm × 3 μm).

with a low PCE (PCE = 0.73%, Entry 4 in Table 1) exhibited a relatively large rms roughness (6.90 nm), and in contrast, the highest-performance device (PCE = 1.60%, Entry 7 in Table 1) exhibited the smallest rms roughness (2.53 nm). Even though the nanomorphology inside the active layer is the most

important factor when discussing device performance [26–28], the AFM analysis indicated that there was a clear relationship between device performance and surface roughness. As for the P3HT:PNBI blend film (Figure 3(d)), phase separation was quite larger due to the aggregation of NBI

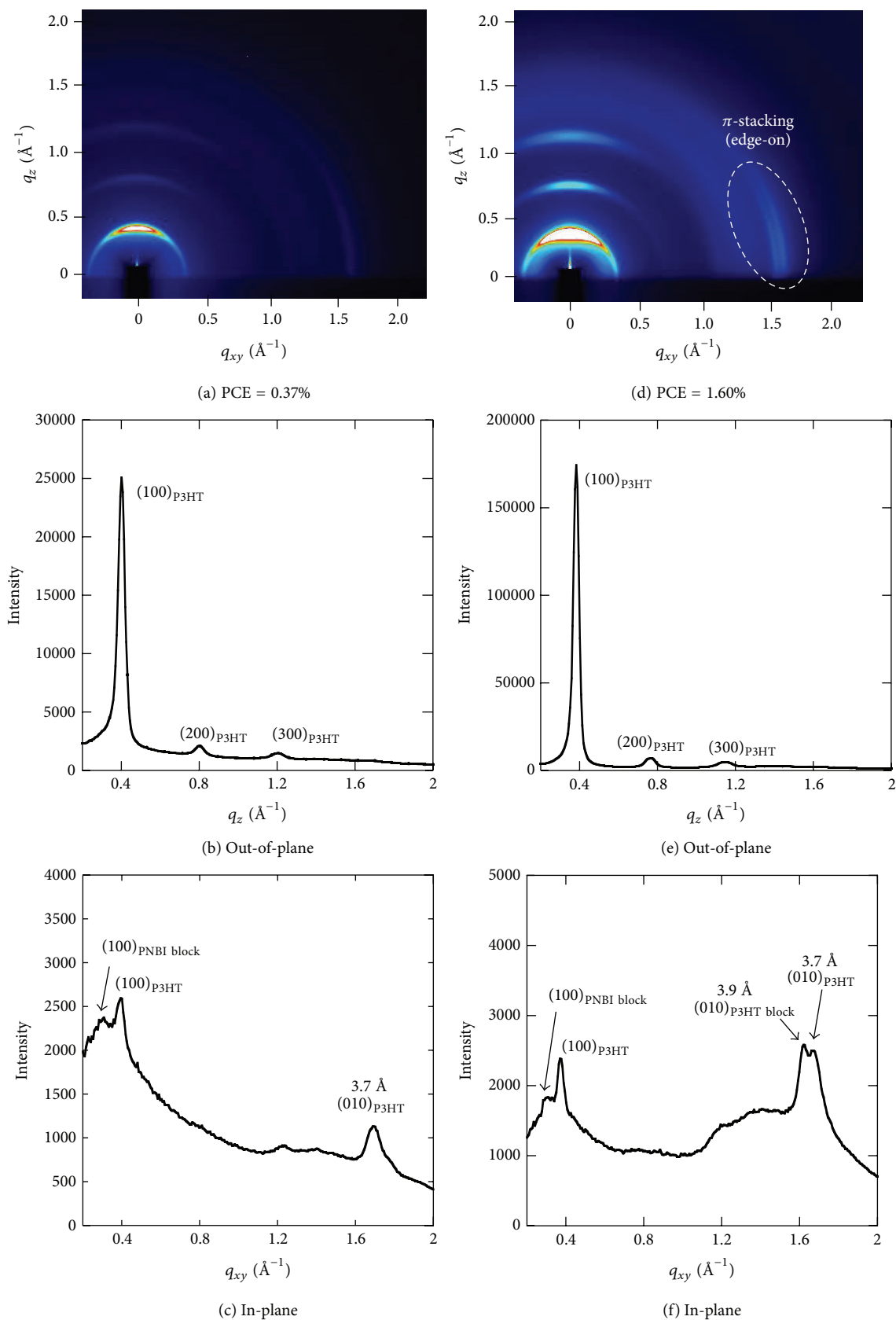


FIGURE 4: GIWAXS images and profiles of as-spun P3HT:P2 (a)–(c) and thermal annealed P3HT:P2 blend films (d)–(f).

units compared to the P3HT:P3HT-PNBI-P3HT blend films; such large phase separation is not suitable for photoelectric conversion process because it brought about self-trapping of excitons, resulting in a low PCE. In the reported all-polymer solar cells using NBI-based polymers [29], the importance to prevent the self-aggregation was mentioned for minimizing self-trapping of excitons. It is likely that good miscibility of P3HT-PNBI-P3HT with P3HT provided the blend active layers which mixed well without self-aggregation of NBI units; this is major advantage of P3HT-PNBI-P3HT over other NBI-based polymers.

3.3. Nanomorphology Observation by GIWAXS Measurement.

Next, GIWAXS measurements were carried out to investigate the in-depth study of the nanomorphology in the P3HT:P3HT-PNBI-P3HT blend films. The as-spun blend film exhibited the (h00) diffractions due to P3HT in the q_z axis (Figure 4(b)). In the q_{xy} axis (Figure 4(c)), three diffractions, which corresponded to the (100) diffraction due to P3HT (15.9 Å), (100) diffraction due to PNBI blocks (20.3 Å), and (010) diffraction (i.e., π - π stacking) due to P3HT (3.7 Å), were clearly observed. After thermal annealing at 200°C, the stronger (h00) diffractions due to P3HT were observed in the q_z axis compared to the as-spun film (Figure 4(e)). In the q_{xy} axis, two kinds of diffractions derived from π - π stacking were observed at 3.9 and 3.7 Å in addition to the (100) diffractions due to P3HT and PNBI (17.0 and 20.3 Å, resp.). Given that the diffraction at 3.7 Å is corresponding to π - π stacking distance between P3HT homopolymers (Figure S3), the other diffraction at 3.9 Å might correspond to π - π stacking of P3HT blocks in P3HT-PNBI-P3HT. Furthermore, intensities of the diffractions due to P3HT in the q_z axis and π - π stacking in the q_{xy} axis were clearly increased by thermal annealing, which suggested that thermal annealing triggered rearrangement of the polymer chains. Eventually, both P3HT homopolymers and P3HT blocks in P3HT-PNBI-P3HT were preferentially oriented in the edge-on manner whereas PNBI blocks were likely to orient in the face-on manner although the clear diffraction derived from π - π stacking of PNBI blocks was not detected because of the low crystallinity. Quiet recently, the GIWAXS study of a similar fully conjugated diblock copolymer composed of PNBI and P3HT blocks was investigated by Wang et al. [30]. Although their block copolymer had the higher crystallinity than that of P3HT-PNBI-P3HT because of the less alkyl solubilized chains, no diffraction derived from π - π stacking of PNBI blocks was observed. Face-on π - π stacking of polymer chains is an ideal nanomorphology for the efficient photoelectric conversion process (e.g., efficient exciton diffusion and charge transportation). Indeed, several recent reports demonstrated the drastic improvements of PCEs were achieved by the face-on π - π stacking nanomorphology in active layers compared to the devices with the edge-on nanomorphology [26–28]. Even though the P3HT:P3HT-PNBI-P3HT blend film had the nanomorphology rich in the edge-on orientation, enhanced polymer-polymer stacking in the thermal annealed film may attribute to the efficient photoelectric conversion process to give a high PCE of 1.60% compared to the as-spun film.

4. Conclusions

An all-polymer solar cell with a high PCE of 1.60% was successfully developed by using fully conjugated D-A block copolymers with NBI-based acceptor blocks (P3HT-PNBI-P3HT) as a nonfullerene acceptor material. AFM and GIWAXS analyses demonstrated that the P3HT:P3HT-PNBI-P3HT blend film could form π - π stacking nanomorphology without large aggregates, resulting in high device performance. This is the major advantage of P3HT-PNBI-P3HT because poor device performance caused by self-aggregation of NBI-based polymers in the blend film is a major problem in several all-polymer solar cells using NBI-based polymers. These results revealed the huge potential for the fully conjugated D-A block copolymer, P3HT-PNBI-P3HT, to be used as a nonfullerene acceptor material in OSCs, and we believe that further improvement of all-polymer solar cells based on P3HT-PNBI-P3HT is possible by fine-tuning of the chemical structure, more precise control of nanomorphology, device fabrication conditions, and so on.

Conflict of Interests

The authors declare that there is no conflict of interests regarding the publication of this paper.

Acknowledgments

This work is supported by Grant-in-Aid for Research Activity Start-up (23850004) provided by the Japan Society for the Promotion of Science (JSPS) and Inamori Foundation. The authors would like to thank Dr. Tomoaki Koganezawa for GIWAXS measurements.

References

- [1] S. Günes, H. Neugebauer, and N. S. Sariciftci, “Conjugated polymer-based organic solar cells,” *Chemical Reviews*, vol. 107, no. 4, pp. 1324–1338, 2007.
- [2] B. C. Thompson and J. M. J. Fréchet, “Polymer-fullerene composite solar cells,” *Angewandte Chemie*, vol. 47, no. 1, pp. 58–77, 2007.
- [3] G. Dennler, M. C. Scharber, and C. J. Brabec, “Polymer-fullerene bulk-heterojunction solar cells,” *Advanced Materials*, vol. 21, no. 13, pp. 1323–1338, 2009.
- [4] H. Zhou, L. Yang, and W. You, “Rational design of high performance conjugated polymers for organic solar cells,” *Macromolecules*, vol. 45, no. 2, pp. 607–632, 2012.
- [5] J. You, L. Dou, K. Yoshimura et al., “A polymer tandem solar cell with 10.6% power conversion efficiency,” *Nature Communications*, vol. 4, article 1446, 2013.
- [6] V. D. Mihailetschi, J. K. J. Van Duren, P. W. M. Blom et al., “Electron transport in a methanofullerene,” *Advanced Functional Materials*, vol. 13, no. 1, pp. 43–46, 2003.
- [7] A. Facchetti, “Polymer donor-polymer acceptor (all-polymer) solar cells,” *Materials Today*, vol. 16, no. 4, pp. 123–132, 2013.
- [8] J. Wang and T. Higashihara, “Synthesis of all-conjugated donor-acceptor block copolymers and their application in all-polymer solar cells,” *Polymer Chemistry*, vol. 4, no. 22, pp. 5518–5526, 2013.

- [9] D. Mori, H. Benten, H. Ohkita, S. Ito, and K. Miyake, "Polymer/polymer blend solar cells improved by using high-molecular-weight fluorene-based copolymer as electron acceptor," *ACS Applied Materials and Interfaces*, vol. 4, no. 7, pp. 3325–3329, 2012.
- [10] E. Zhou, K. Tajima, C. Yang, and K. Hashimoto, "Band gap and molecular energy level control of perylene diimide-based donor-acceptor copolymers for all-polymer solar cells," *Journal of Materials Chemistry*, vol. 20, no. 12, pp. 2362–2368, 2010.
- [11] N. Zhou, H. Lin, S. J. Lou et al., "Morphology-performance relationships in high-efficiency all-polymer solar cells," *Advanced Energy Materials*, vol. 4, no. 3, Article ID 1300785, 2014.
- [12] D. Mori, H. Benten, I. Okada, H. Ohkita, and S. Ito, "Low-bandgap donor/acceptor polymer blend solar cells with efficiency exceeding 4%," *Advanced Energy Materials*, vol. 4, no. 3, Article ID 1301006, 2014.
- [13] S. Fabiano, Z. Chen, S. Vahedi, A. Facchetti, B. Pignataro, and M. A. Loi, "Role of photoactive layer morphology in high fill factor all-polymer bulk heterojunction solar cells," *Journal of Materials Chemistry*, vol. 21, no. 16, pp. 5891–5896, 2011.
- [14] Y. Kim, S. Cook, S. A. Choulis, J. Nelson, J. R. Durrant, and D. D. C. Bradley, "Organic photovoltaic devices based on blends of regioregular poly(3-hexylthiophene) and poly(9,9-dioctylfluorene-co-benzothiadiazole)," *Chemistry of Materials*, vol. 16, no. 23, pp. 4812–4818, 2004.
- [15] H. J. Snaith, A. C. Arias, A. C. Morteani, C. Silva, and R. H. Friend, "Charge generation kinetics and transport mechanisms in blended polyfluorene photovoltaic devices," *Nano Letters*, vol. 2, no. 12, pp. 1353–1357, 2002.
- [16] K. Nakabayashi and H. Mori, "All-polymer solar cells based on fully conjugated block copolymers composed of poly(3-hexylthiophene) and poly(naphthalene bisimide) segments," *Macromolecules*, vol. 45, no. 24, pp. 9618–9625, 2012.
- [17] M. Yuan, M. M. Durban, P. D. Kazarinoff et al., "Synthesis and characterization of fused-thiophene containing naphthalene diimide n-type copolymers for organic thin film transistor and all-polymer solar cell applications," *Journal of Polymer Science, Part A: Polymer Chemistry*, vol. 51, no. 19, pp. 4061–4069, 2013.
- [18] M. Schubert, D. Dolfen, J. Frisch et al., "Influence of aggregation on the performance of all-polymer solar cells containing low-bandgap naphthalenediimide copolymers," *Advanced Energy Materials*, vol. 2, no. 3, pp. 369–380, 2012.
- [19] Y.-J. Hwang, G. Ren, N. M. Murari, and S. A. Jenekhe, "N-type naphthalene diimide-biselenophene copolymer for all-polymer bulk heterojunction solar cells," *Macromolecules*, vol. 45, no. 22, pp. 9056–9062, 2012.
- [20] E. Zhou, J. Cong, J. Q. Wei, K. Tajima, C. Yang, and K. Hashimoto, "All-polymer solar cells from perylene diimide based copolymers: material design and phase separation control," *Angewandte Chemie*, vol. 123, pp. 2851–2855, 2011.
- [21] X. Zhang, Z. Lu, L. Ye et al., "A potential perylene diimide dimer-based acceptor material for highly efficient solution-processed non-fullerene organic solar cells with 4.03% efficiency," *Advanced Materials*, vol. 25, no. 40, pp. 5791–5797, 2013.
- [22] N. Zhou, H. Lin, S. J. Lou et al., "Morphology-performance relationships in high-efficiency all-polymer solar cells," *Advanced Energy Materials*, vol. 4, no. 3, Article ID 1300785, 2014.
- [23] T. Earmme, Y.-J. Hwang, N. M. Murari, S. Subramanian, and S. A. Jenekhe, "All-polymer solar cells with 3.3% efficiency based on naphthalene diimide-selenophene copolymer acceptor," *Journal of the American Chemical Society*, vol. 135, no. 40, pp. 14960–14963, 2013.
- [24] D. Mori, H. Benten, J. Kosaka, H. Ohkita, S. Ito, and K. Miyake, "Polymer/polymer blend solar cells with 2.0% efficiency developed by thermal purification of nanoscale-phase-separated morphology," *ACS Applied Materials and Interfaces*, vol. 3, no. 8, pp. 2924–2927, 2011.
- [25] E. Verploegen, R. Mondal, C. J. Bettinger, S. Sok, M. F. Toney, and Z. Bao, "Effects of thermal annealing upon the morphology of polymer-fullerene blends," *Advanced Functional Materials*, vol. 20, no. 20, pp. 3519–3529, 2010.
- [26] I. Osaka, T. Kakara, N. Takemura, T. Koganezawa, and K. Takimiya, "Naphthodithiophene-naphthobisthiadiazole copolymers for solar cells: alkylation drives the polymer backbone flat and promotes efficiency," *Journal of the American Chemical Society*, vol. 135, no. 24, pp. 8834–8837, 2013.
- [27] I. Osaka, M. Shimawaki, H. Mori et al., "Synthesis, characterization, and transistor and solar cell applications of a naphthobisthiadiazole-based semiconducting polymer," *Journal of the American Chemical Society*, vol. 134, no. 7, pp. 3498–3507, 2012.
- [28] M. S. Chen, J. R. Niskala, D. A. Unruh, C. K. Chu, O. P. Lee, and J. M. J. Fréchet, "Control of polymer-packing orientation in thin films through synthetic tailoring of backbone coplanarity," *Chemistry of Materials*, vol. 25, no. 20, pp. 4088–4096, 2013.
- [29] J. R. Moore, S. Albert-Seifried, A. Rao et al., "Polymer blend solar cells based on a high-mobility naphthalenediimide-based polymer acceptor: device physics, photophysics and morphology," *Advanced Energy Materials*, vol. 1, no. 2, pp. 230–240, 2011.
- [30] J. Wang, M. Ueda, and T. Higashihara, "Synthesis and morphology of all-conjugated donor-acceptor block copolymers based on poly(3-hexylthiophene) and poly(naphthalene diimide)," *Journal of Polymer Science, Part A: Polymer Chemistry*, vol. 52, no. 8, pp. 1139–1148, 2014.

Research Article

Theoretical Study on Cyclopeptides as the Nanocarriers for Li^+ , Na^+ , K^+ and F^- , Cl^- , Br^-

Lili Liu¹ and Shimou Chen²

¹ Department of Chemistry, School of Science, Beijing Technology and Business University, Beijing 100048, China

² Key Laboratory of Green Process and Engineering, Institute of Process Engineering (IPE), Chinese Academy of Sciences (CAS), Beijing 100190, China

Correspondence should be addressed to Shimou Chen; chenshimou@ipe.ac.cn

Received 6 July 2014; Accepted 7 October 2014

Academic Editor: Hanwen Sun

Copyright © 2015 L. Liu and S. Chen. This is an open access article distributed under the Creative Commons Attribution License, which permits unrestricted use, distribution, and reproduction in any medium, provided the original work is properly cited.

The interaction process between a series of cyclopeptide compounds $\text{cyclo}(\text{Gly})_n$ ($n = 4, 6, 8$) and monovalent ions (Li^+ , Na^+ , K^+ , F^- , Cl^- , and Br^-) was studied using theoretical calculation. The mechanism of combination between the $\text{cyclo}(\text{Gly})_n$ and ions was discussed through binding energy, Mulliken electron population, and hydrogen bond. It was found that for the same cyclopeptide the binding energy has the order of $\text{cyclo}(\text{Gly})_n-\text{Li}^+ > \text{cyclo}(\text{Gly})_n-\text{Na}^+ > \text{cyclo}(\text{Gly})_n-\text{K}^+$ and $\text{cyclo}(\text{Gly})_n-\text{F}^- > \text{cyclo}(\text{Gly})_n-\text{Br}^- > \text{cyclo}(\text{Gly})_n-\text{Cl}^-$. The binding energy manifests the stable complex of $\text{cyclo}(\text{Gly})_n$ and ions can be formed, and the different energy shows the potential use of $\text{cyclo}(\text{Gly})_n$ as nanocarriers for metal ions or the extractant for ions separation.

1. Introduction

As an important family of host-guest complexation, ion carriers play an important role in various biological processes [1]. In particular, in biomedical research, the controlled delivery of drugs to specific tissues in the body is an ongoing challenge. Ion carriers are promising delivery vehicles that offer increased drugs circulation times and enhanced dissolution rates and bioavailability. Macrocyclic compound is one of the best choices as ion carriers because of its special structure. For example, crown ether [2, 3], cyclopeptide [4–9], and calixarene [10–12] can combine with alkali metal ions or alkaline-earth metal ions to form a dissolvable complex or act as ion and neutral molecular carriers. Since the 1940s, when the first cyclopeptide gramicidin was found [13], due to its similar structure to macrocyclic compound, the cyclopeptide aroused much interest in host-guest chemistry. It is demonstrated that cyclopeptides are promising materials as carriers, antibiotics, regulators of membrane ion and systems for specific guest recognition, and so forth [5, 14]. Many theoretical calculations on cyclopeptides-ions complex were performed in order to direct the construction of ion-assisted cyclopeptide system [15–17]. Owing to the metabolism

stability and the high bioavailability, many of them could be used as prodrugs, medicament, and ion carriers [18, 19]. It is believed that the biological activities of cyclopeptide with metal ion are of much potential application in medical and biological chemistry.

In all subjects related to cyclopeptide or modified cyclopeptide as ion carriers, the stereoselectivity on ions becomes the focus of the experimental and theoretical studies. This selectivity is due to the special structure of the cyclopeptide. Cyclopeptide has a cavity structure with restricted carbonyl group and amino group on inner side of the molecule and a rigid molecule skeleton that can support the molecule cavity. Tan et al. [20] have studied the cyclopeptide composed of $\text{cyclo}[(\beta^3\text{-Hgly})_4^-]$ through computational method. Huang et al. [21] have designed and synthesized a cystine-bearing pseudo-cyclopeptide as amphireceptor; it binds to cations or anions through the carbonyl or amino groups, respectively. Using ab initio calculations, Kim and coworkers [22] proposed that cyclic peptides may be able to serve as good amphi-ionophores because of the availability of both amide and crown-like structures within the molecule. However, to design useful cyclopeptide carrier and shed light on the related organic synthesis, various factors such as the

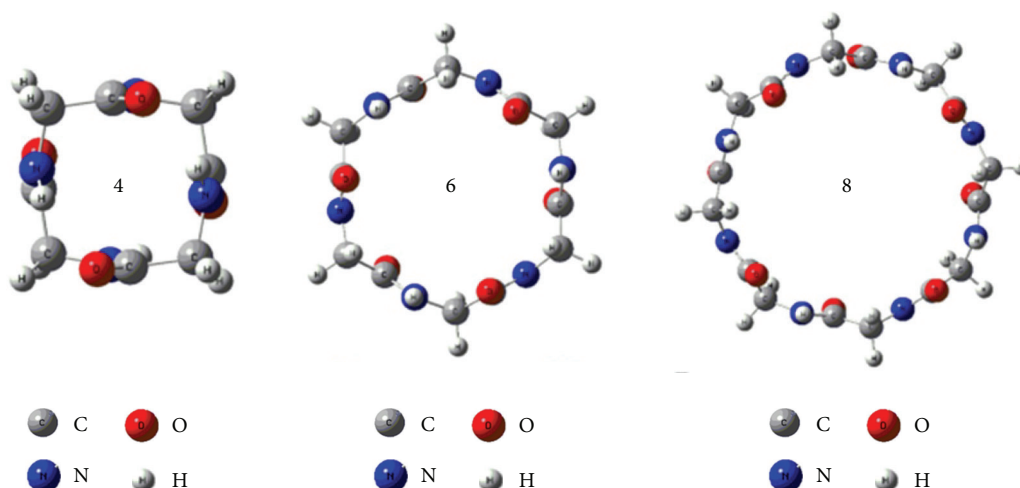


FIGURE 1: The most stable conformation of cyclo(Gly)_n ($n = 4, 6, \text{ and } 8$).

structure of the component peptide, peptide number, and the interaction of the ions and peptide should be studied carefully.

In the previous work reported by Zhu et al. [23], the preferred conformations of cyclic dipeptides were first studied using the density functional theory (DFT). Herein, we take a systematically theoretical study on the conformation and complexation of cyclo(Gly)_n ($n = 4, 6, \text{ and } 8$) and monovalent ions (Li^+ , Na^+ , K^+ , F^- , Cl^- , and Br^-) using the DFT B3LYP method at 6-31G(d) level. To the best of our knowledge, the study of interaction of the cycloquadpeptide, cyclohexapeptide, and cyclooctopeptide with both anions and cations synchronously would be the first report in the literature. It should be mentioned that only the cases of one cyclopeptide carrying one ion were discussed in this paper; that is, the ratio of the cyclopeptide carrier to the ions receptor is 1:1. The cyclopeptide carrying multi-ions will be reported in the future.

2. Computational Methods

Glycine (Gly) was chosen as monomer to form cyclopeptide because of its simple structure. We begin our research with the construction of cyclohexapeptide; there are 8 different isomerides of Gly cyclohexapeptide: all of them were optimized by HF/STO-3G method and the most stable ones were selected as ion carrier for further study. Based on the stable configuration of three kinds of cyclopeptide, the complexes of three kinds of cyclopeptide with cations K^+ , Li^+ , and Na^+ and anions F^- , Cl^- , and Br^- were optimized at B3LYP/6-31G level, respectively. All computations were carried out using the Gaussian 03 package [24].

3. Results and Discussion

3.1. The Optimum Conformations. The conformations of the most stable cyclohexapeptide are shown in Figure 1; all of them were optimized by HF/STO-3G method. It has a

transconfiguration structure. In order to obtain a deep understanding of the characteristic of the cycloquadpeptide, cyclohexapeptide, and cyclooctopeptide, the three cyclopeptides were further optimized at B3LYP/6-31G level to guarantee that the configuration is the most stable one [25, 26].

The optimum conformations of the cation-cyclopeptide complexes were shown in Figure 2. Both the top view and side view were given considering the complicated geometry of {cyclo(Gly)_n-M⁺} ($n = 4, 6, 8; M = \text{Li, Na, K}$).

From Figure 2, the {cyclo(Gly)₄} complexes hold a C_1 : the symmetry group after combining a cation to form {cyclo(Gly)₄-M⁺} ($M = \text{Li, Na, K}$) complexes. All three cations hover outside the cyclopeptide for the small space of the cycloquadpeptide cavity (as shown in Figure 2). The two carbonyl groups of the cycloquadpeptide turn towards the cation ion from original position. The configuration of cyclopeptide was distorted to a boat form, and the ions lay over the boat. The average distance between the cation ion and the carbonyl oxygen is 0.186 nm, 0.222 nm, and 0.285 nm for Li^+ , Na^+ , and K^+ , respectively.

Comparing the {cyclo(Gly)₆} with {cyclo(Gly)₆-M⁺} ($M = \text{Li, Na, K}$), it can be found that all those complexes keep C_1 symmetry group, and the three cation ions stay in the center of cyclohexapeptide cavity. All the six carbonyl groups on the peptide turn towards the cation. The distance between the cation and the carbonyl oxygen is 0.221 nm, 0.236 nm, and 0.267 nm for Li^+ , Na^+ , and K^+ , respectively.

As for cyclooctopeptide complexes, the conformation changes greatly after forming {cyclo(Gly)₈-M⁺} ($M = \text{Li, Na, K}$). The {cyclo(Gly)₈} in Figure 1 is C_4 symmetry group, and symmetry of {cyclo(Gly)₈-M⁺} ($M = \text{Li, Na, K}$) in Figure 2 degenerates to C_1 . The cation was packaged up completely by the cyclooctopeptide because of the larger cavity of the cyclopeptide, and four carbonyl groups turn towards the cation. The average distance between the cation and the carbonyl oxygen is 0.193 nm, 0.241 nm, and 0.280 nm for Li^+ , Na^+ , and K^+ , respectively.

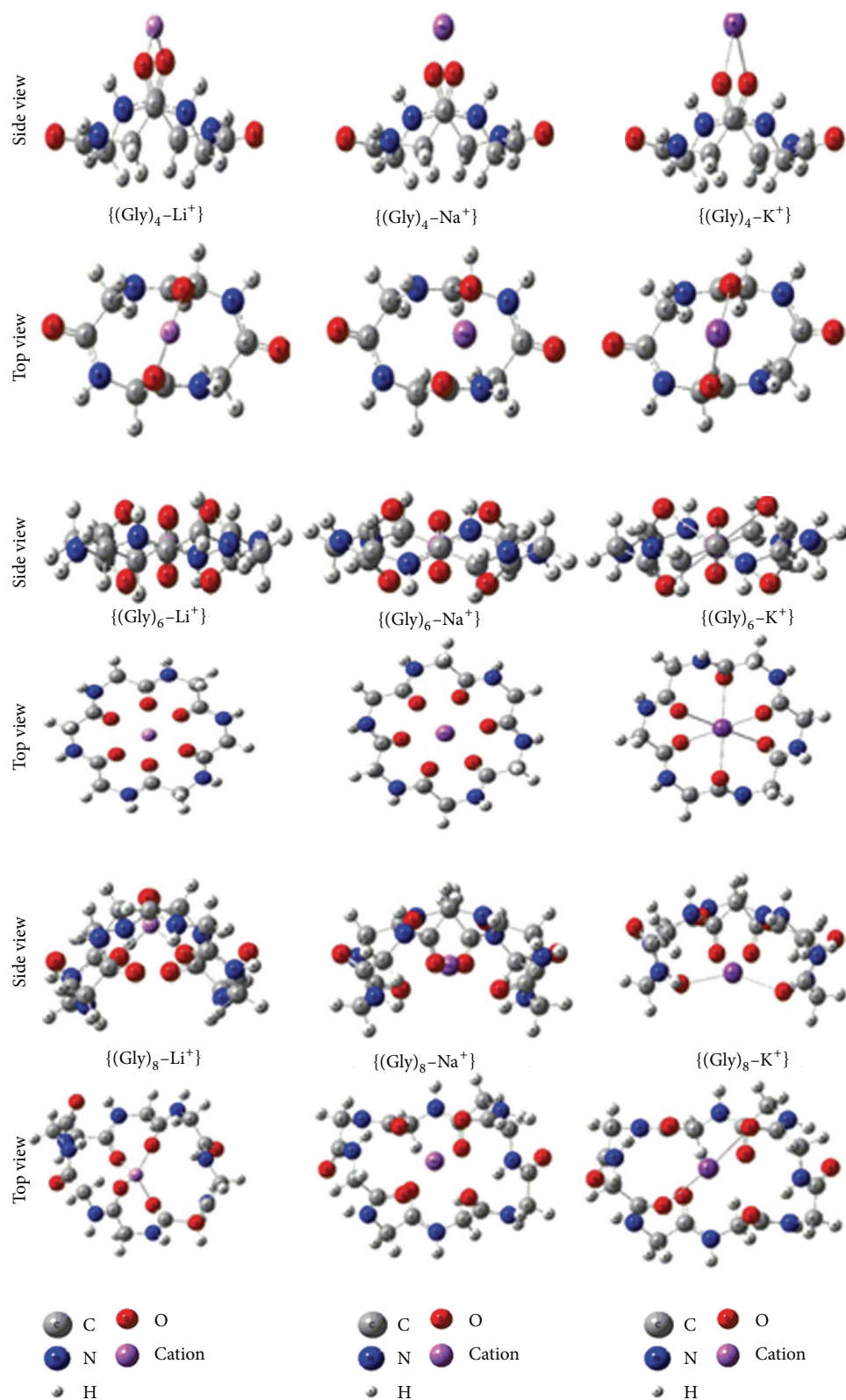


FIGURE 2: The conformation of cyclopeptide with Li^+ , Na^+ , and K^+ after optimization. Every structure was shown from side view and top view.

TABLE 1: The bond length (nm) and binding energy ($\text{kJ}\cdot\text{mol}^{-1}$) of $\{\text{cyclo}(\text{Gly})_n-\text{M}^+\}$.

| Complex | $\text{M}^+-\text{O}/\text{nm}$ | Binding energy/ $\text{kJ}\cdot\text{mol}^{-1}$ |
|--|---------------------------------|---|
| $\{\text{cyclo}(\text{Gly})_4-\text{Li}^+\}$ | 0.186 | 207.123 |
| $\{\text{cyclo}(\text{Gly})_4-\text{Na}^+\}$ | 0.222 | 118.326 |
| $\{\text{cyclo}(\text{Gly})_4-\text{K}^+\}$ | 0.265 | 44.523 |
| $\{\text{cyclo}(\text{Gly})_6-\text{Li}^+\}$ | 0.221 | 490.967 |
| $\{\text{cyclo}(\text{Gly})_6-\text{Na}^+\}$ | 0.236 | 399.866 |
| $\{\text{cyclo}(\text{Gly})_6-\text{K}^+\}$ | 0.267 | 241.546 |
| $\{\text{cyclo}(\text{Gly})_8-\text{Li}^+\}$ | 0.193 | 548.325 |
| $\{\text{cyclo}(\text{Gly})_8-\text{Na}^+\}$ | 0.241 | 415.457 |
| $\{\text{cyclo}(\text{Gly})_8-\text{K}^+\}$ | 0.280 | 324.474 |

The optimized structures of $\{\text{cyclo}(\text{Gly})_n-\text{X}^-\}$ ($n = 4, 6, 8$; $\text{X} = \text{F}, \text{Br}, \text{Cl}$) were shown in Figure 3. Each complex has $\text{X}^- \cdots \text{H}-\text{N}$ hydrogen bonds, and all hydrogen atoms on the amino group turn towards the anion in $\{\text{cyclo}(\text{Gly})_n-\text{X}^-\}$ ($n = 4, 6$; $\text{X} = \text{F}, \text{Br}, \text{Cl}$). The complex $\{\text{cyclo}(\text{Gly})_4-\text{X}^-\}$ ($\text{X} = \text{F}, \text{Br}, \text{Cl}$) has C_1 symmetry group like the original cycloquadpeptide. Symmetry group of $\{\text{cyclo}(\text{Gly})_6-\text{X}^-\}$ ($\text{X} = \text{Br}, \text{Cl}$) is C_6 , but, for the $\{\text{cyclo}(\text{Gly})_6-\text{X}^-\}$ ($\text{X} = \text{F}$) complex, the symmetry group is C_3 after complexation. The symmetry group of the cyclooctopeptide degenerate from C_4 to C_1 after forming the complex $\{\text{cyclo}(\text{Gly})_8-\text{X}^-\}$ ($\text{X} = \text{F}, \text{Br}, \text{Cl}$).

3.2. Binding Energy and the Distance of the Ion and Cyclopeptide Analysis. Binding energy is a vital standard in evaluating the stability of the complex compound. Table 1 shows the energy and the distance between the cation and the carbonyl oxygen on the cyclopeptide. From the analysis of the data, for the same cyclopeptide, the average distance between cation and the carbonyl oxygen is in the order of $\text{K}^+ > \text{Na}^+ > \text{Li}^+$; however, the binding energy has the order of $\text{Li}^+ > \text{Na}^+ > \text{K}^+$ (see Figure 4). It means that the distance between the cation and the cyclopeptide is smaller; the binding energy of the compound is larger. On the other hand, for the same cation in the different cyclopeptide, the binding energy reduced in order of $\{\text{cyclo}(\text{Gly})_8-\text{M}^+\} > \{\text{cyclo}(\text{Gly})_6-\text{M}^+\} > \{\text{cyclo}(\text{Gly})_4-\text{M}^+\}$.

Table 2 shows the energies and the distances between the anions and H atoms on the amino groups. The results indicated that, for the same cyclopeptide, the average distance between anion and the amino hydrogen reduced in order of $\text{Br}^- > \text{Cl}^- > \text{F}^-$, and the binding energy increased in the order of $\text{Cl}^- < \text{Br}^- < \text{F}^-$ (Figure 6). For the same anion in the different cyclopeptide, the binding energy reduced in order of $\{\text{cyclo}(\text{Gly})_8-\text{X}^-\} > \{\text{cyclo}(\text{Gly})_6-\text{X}^-\} > \{\text{cyclo}(\text{Gly})_4-\text{X}^-\}$ ($\text{X} = \text{Br}, \text{Cl}$), but, for $\text{X} = \text{F}$, the order is $\{\text{cyclo}(\text{Gly})_6-\text{X}^-\} > \{\text{cyclo}(\text{Gly})_8-\text{X}^-\} > \{\text{cyclo}(\text{Gly})_4-\text{X}^-\}$ due to the strong electrostatic interactions between H and F^- . Considering the large difference of the binding energy value illustrated in Table 1 and Table 2, the cyclopeptides should have the potential application as ions extractant.

TABLE 2: The bond length (nm) and binding energy ($\text{kJ}\cdot\text{mol}^{-1}$) of $\{\text{cyclo}(\text{Gly})_n-\text{X}^-\}$.

| Complex | X-H | N-H | H-Bond | Binding energy |
|--|-------|-------|--------|----------------|
| $\{\text{cyclo}(\text{Gly})_4-\text{F}^-\}$ | 0.144 | 0.108 | 0.249 | 394.185 |
| $\{\text{cyclo}(\text{Gly})_4-\text{Br}^-\}$ | 0.228 | 0.104 | 0.325 | 139.792 |
| $\{\text{cyclo}(\text{Gly})_4-\text{Cl}^-\}$ | 0.222 | 0.104 | 0.317 | 115.136 |
| $\{\text{cyclo}(\text{Gly})_6-\text{F}^-\}$ | 0.186 | 0.102 | 0.288 | 541.121 |
| $\{\text{cyclo}(\text{Gly})_6-\text{Br}^-\}$ | 0.244 | 0.102 | 0.346 | 276.245 |
| $\{\text{cyclo}(\text{Gly})_6-\text{Cl}^-\}$ | 0.240 | 0.102 | 0.341 | 219.198 |
| $\{\text{cyclo}(\text{Gly})_8-\text{F}^-\}$ | 0.153 | 0.107 | 0.257 | 531.038 |
| $\{\text{cyclo}(\text{Gly})_8-\text{Br}^-\}$ | 0.230 | 0.103 | 0.331 | 287.230 |
| $\{\text{cyclo}(\text{Gly})_8-\text{Cl}^-\}$ | 0.221 | 0.103 | 0.322 | 246.257 |

TABLE 3: Orbital overlap population of $\{\text{cyclo}(\text{Gly})_n-\text{X}^-\}$ and $\{\text{cyclo}(\text{Gly})_n-\text{M}^+\}$.

| Complex | M^+-O (e) | | | X-H (e) | | |
|---------|---------------------------|---------------|--------------|--------------|---------------|---------------|
| | Li^+ | Na^+ | K^+ | F^- | Br^- | Cl^- |
| $n = 4$ | 0.175 | 0.117 | 0.07 | 0.276 | 0.224 | 0.195 |
| $n = 6$ | 0.652 | 0.502 | 0.317 | 0.378 | 0.341 | 0.296 |
| $n = 8$ | 0.502 | 0.458 | 0.299 | 0.246 | 0.212 | 0.196 |

TABLE 4: The quantity of electricity of anion X^- in $\{\text{cyclo}(\text{Gly})_n-\text{X}^-\}$.

| Cyclo(Gly) _n | Atomic charges (e) | | |
|-------------------------|--------------------|---------------|---------------|
| | F^- | Br^- | Cl^- |
| $n = 4$ | -0.578 | -0.716 | -0.768 |
| $n = 6$ | -0.526 | -0.604 | -0.683 |
| $n = 8$ | -0.548 | -0.659 | -0.727 |

3.3. Mulliken Electron Population. The strength of the covalent bond between the two atoms A and B can be obtained from the Mulliken electron population analysis [27–29]. If the overlapping electron has a large population between A and B, the covalent bond between the two atoms A and B will be stronger, the binding energy will have a larger value, and the compound should be more stable. The electron overlapping populations were shown in Table 3.

It can be found that the electron overlapping population value has the order of $\text{cyclo}(\text{Gly})_n-\text{Li}^+ > \text{cyclo}(\text{Gly})_n-\text{Na}^+ > \text{cyclo}(\text{Gly})_n-\text{K}^+$ and $\text{cyclo}(\text{Gly})_n-\text{F}^- > \text{cyclo}(\text{Gly})_n-\text{Br}^- > \text{cyclo}(\text{Gly})_n-\text{Cl}^-$. This order is the same as the order of the binding energy (see Figures 5 and 7) and the distance of M^+-O .

In addition, it is very interesting that the order of the binding energy is $\text{cyclo}(\text{Gly})_n-\text{F}^- > \text{cyclo}(\text{Gly})_n-\text{Br}^- > \text{cyclo}(\text{Gly})_n-\text{Cl}^-$ and the order of the electron overlapping populations is $\text{F}^- > \text{Br}^- > \text{Cl}^-$; this is different from the order of the distance of the X^--H and the order of the three atoms F, Cl, and Br in periodic table. Therefore, we carried out the electric quantity calculation of the three halogen ions and cyclopeptides. From the analysis of the data in Table 4, the anion Br^- has more electrons than Cl^- and the order of the electronic quantity is $\text{F}^- > \text{Br}^- > \text{Cl}^-$. Considering the electrostatic interactions between negatively charged X^- and

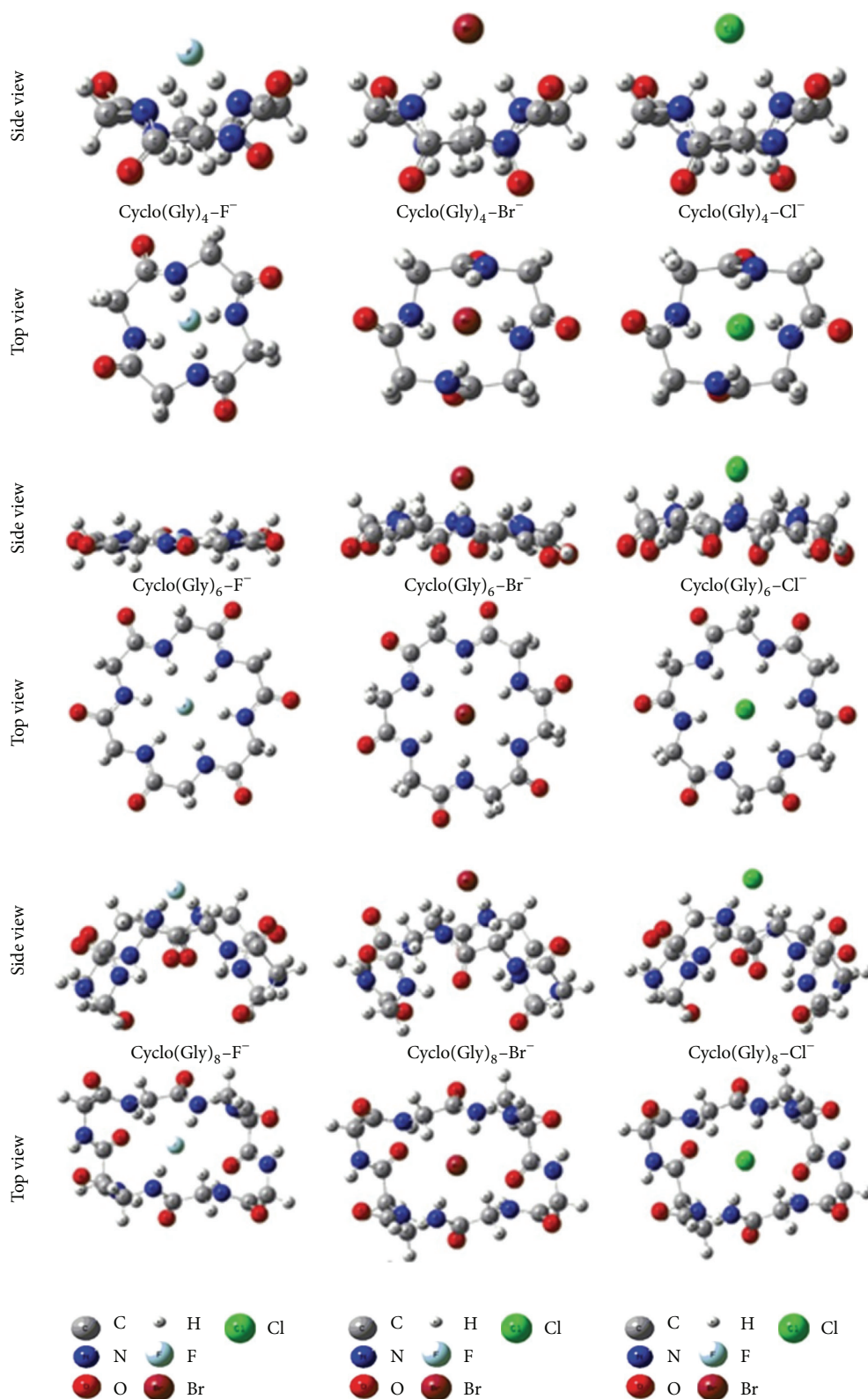


FIGURE 3: The optimizing conformation of cyclopeptide with F⁻, Cl⁻, and Br⁻. The side view and top view structure of all of the complexes were presented for better geometry understanding.

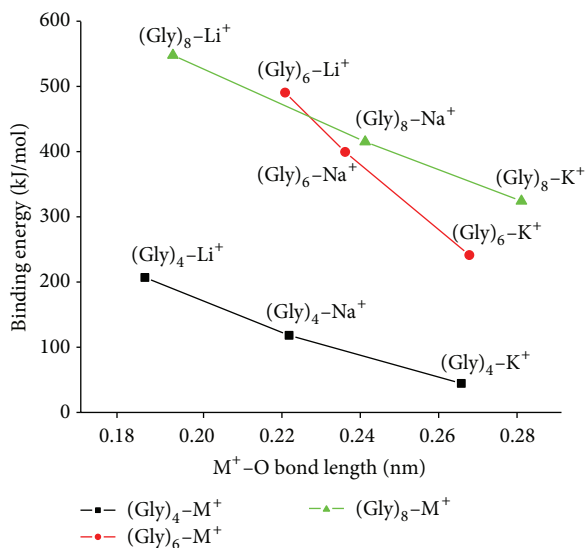


FIGURE 4: The relationship between the M^+ -O bond length and the binding energy of {cyclo (Gly)_n-M⁺}.

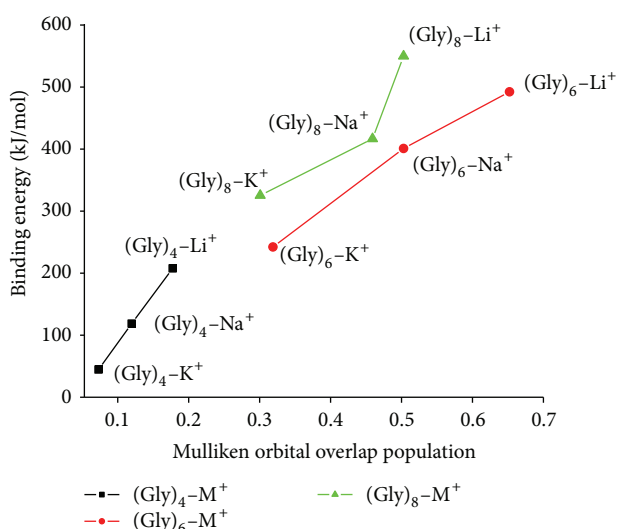


FIGURE 5: The relationship between the orbital overlap population and the binding energy of {cyclo (Gly)_n-M⁺}.

positively charged amino H^+ atoms, the abnormal order of binding energy can be expected [14, 22].

4. Conclusions

The cyclopeptides as ion nanocarriers for cations (Li^+ , Na^+ , and K^+) and anions (F^- , Cl^- , and Br^-) were studied carefully by theoretical calculation. The optimum conformation of cation-cyclopeptides and anion-cyclopeptides complexes was obtained by HF/STO-3G method and then further optimized at B3LYP/6-31G level. Both the cation and anion have a strong interaction with the cyclopeptide indicating that the cyclopeptides can act as amphi-ions carriers. The binding energy has the order of cyclo(Gly)_n-Li⁺ >

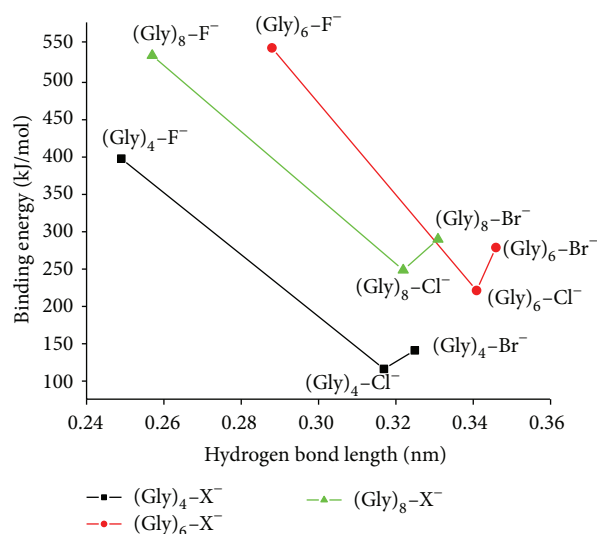


FIGURE 6: The relationship between the hydrogen bond length and the binding energy of {cyclo (Gly)_n-X⁻}.

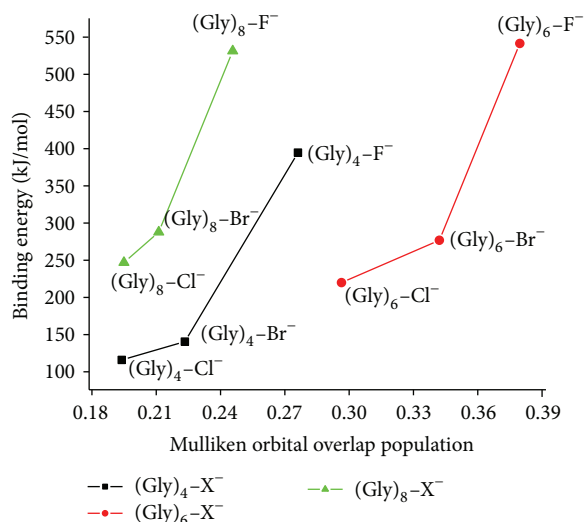


FIGURE 7: The relationship between the orbital overlap population and the binding energy of {cyclo (Gly)_n-X⁻}.

cyclo(Gly)_n-Na⁺ > cyclo(Gly)_n-K⁺ and cyclo(Gly)_n-F⁻ > cyclo(Gly)_n-Br⁻ > cyclo(Gly)_n-Cl⁻ for the different cyclopeptide. For cation ions Li^+ , Na^+ , and K^+ , the binding energy of the different cyclopeptide is {cyclo (Gly)₈-M⁺} > {cyclo (Gly)₆-M⁺} > {cyclo (Gly)₄-M⁺}. For anions Br^- and Cl^- , the binding energy has an order of {Cyclo (Gly)₈-X⁻} > {cyclo (Gly)₆-X⁻} > {cyclo (Gly)₄-X⁻}; for F^- , {cyclo (Gly)₆-F⁻} > {cyclo (Gly)₈-F⁻} > {cyclo (Gly)₄-F⁻} due to the strong electrostatic interactions between hydrogen bond and F^- . The different value of the binding energy illustrated that the cyclopeptide should have the potential application as ions extractants.

Conflict of Interests

The authors declare that there is no conflict of interests regarding the publication of this paper.

Acknowledgments

The work described in this paper was supported by the National Natural Science Foundation of China (no. 21276257) and the Research Foundation for Youth Scholars of Beijing Technology and Business University (no. QNJJ2014-14).

References

- [1] S. K. Kim and J. L. Sessler, "Ion pair receptors," *Chemical Society Reviews*, vol. 39, no. 10, pp. 3784–3809, 2010.
- [2] Y. Kobuke, K. Kobubo, and M. Munakata, "Cooperative metal ion binding by metal organized crown ether," *Journal of the American Chemical Society*, vol. 117, no. 51, pp. 12751–12758, 1995.
- [3] C. A. Kozłowski and J. Kozłowska, "PNP-16-crown-6 derivatives as ion carriers for Zn(II), Cd(II) and Pb(II) transport across polymer inclusion membranes," *Journal of Membrane Science*, vol. 326, no. 1, pp. 215–221, 2009.
- [4] M. Tang, J. F. Fan, J. Liu, L. J. He, and K. He, "Applications of cyclic peptide nanotubes," *Progress in Chemistry*, vol. 22, no. 4, pp. 648–653, 2010.
- [5] D. Ranganathan, "Designer hybrid cyclopeptides for membrane ion transport and tubular structures," *Accounts of Chemical Research*, vol. 34, no. 11, pp. 919–930, 2001.
- [6] O. Renaudet, G. Dasgupta, I. Bettahi et al., "Linear and branched glyco-lipopeptide vaccines follow distinct cross-presentation pathways and generate different magnitudes of antitumor immunity," *PLoS ONE*, vol. 5, no. 6, Article ID e11216, 2010.
- [7] L. Wanka, K. Iqbal, and P. R. Schreiner, "The lipophilic bullet hits the targets: medicinal chemistry of adamantane derivatives," *Chemical Reviews*, vol. 113, no. 5, pp. 3516–3604, 2013.
- [8] A. Späth and B. Knig, "Molecular recognition of organic ammonium ions in solution using synthetic receptors," *Beilstein Journal of Organic Chemistry*, vol. 6, article 32, 2010.
- [9] D. Ranganathan, A. Thomas, V. Haridas et al., "Design, synthesis, and characterization of a novel family of macrocyclic membrane ion-transporting depsipeptides," *Journal of the American Chemical Society*, vol. 120, pp. 11578–11584, 1998.
- [10] C. C. Tong, R. Quesada, J. L. Sessler, and P. A. Gale, "meso-Octamethylcalix[4]pyrrole: an old yet new transmembrane ion-pair transporter," *Chemical Communications*, no. 47, pp. 6321–6323, 2008.
- [11] P. K. Lo and M. S. Wong, "Extended calix[4]arene-based receptors for molecular recognition and sensing," *Sensors*, vol. 8, no. 9, pp. 5313–5335, 2008.
- [12] H. Chen, L. Gu, Y. Yin, K. Koh, and J. Lee, "Molecular recognition of arginine by supramolecular complexation with calixarene crown ether based on surface plasmon resonance," *International Journal of Molecular Sciences*, vol. 12, no. 4, pp. 2315–2324, 2011.
- [13] Y. A. Ovchinnikov and V. T. Ivanov, "Conformational states and biological activity of cyclic peptides," *Tetrahedron*, vol. 31, no. 18, pp. 2177–2209, 1975.
- [14] I. Sainis, D. Fokas, K. Vareli, A. G. Tzakos, V. Kounnis, and E. Briasoulis, "Cyanobacterial cyclopeptides as lead compounds to novel targeted cancer drugs," *Marine Drugs*, vol. 8, no. 3, pp. 629–657, 2010.
- [15] S. Kirmizialtin and R. Elber, "Computational exploration of mobile ion distributions around RNA duplex," *The Journal of Physical Chemistry B*, vol. 114, no. 24, pp. 8207–8220, 2010.
- [16] S. Chowdhury, G. Schatte, and H. B. Kraatz, "A cyclic Fc-histidine conjugate: Synthesis and properties—interactions with alkali metal ions," *European Journal of Inorganic Chemistry*, no. 5, pp. 988–993, 2006.
- [17] A. C. Gucinski, J. Chamot-Rooke, E. Nicol, Á. Somogyi, and V. H. Wysocki, "Structural influences on preferential oxazolone versus diketopiperazine b_2^+ ion formation for histidine analogue-containing peptides," *The Journal of Physical Chemistry A*, vol. 116, no. 17, pp. 4296–4304, 2012.
- [18] N. Graf and S. J. Lippard, "Redox activation of metal-based prodrugs as a strategy for drug delivery," *Advanced Drug Delivery Reviews*, vol. 64, no. 11, pp. 993–1004, 2012.
- [19] T. G. Flick, W. A. Donald, and E. R. Williams, "Electron capture dissociation of trivalent metal ion-peptide complexes," *Journal of the American Society for Mass Spectrometry*, vol. 24, no. 2, pp. 193–201, 2013.
- [20] H. Tan, W. Qu, G. Chen, and R. Liu, "Theoretical investigation of the self-assembly of cyclo[(- β^3 -HGly) $_4$ -]," *Chemical Physics Letters*, vol. 369, no. 5–6, pp. 556–562, 2003.
- [21] H. Huang, L. Mu, J. He, and J.-P. Cheng, "A cystine-bearing pseudo-cyclopeptide as a new amphi-receptor," *Tetrahedron Letters*, vol. 43, no. 12, pp. 2255–2258, 2002.
- [22] K. S. Kim, C. Cui, and S. J. Cho, "Novel amphi-ionophores," *The Journal of Physical Chemistry B*, vol. 102, no. 2, pp. 461–463, 1998.
- [23] Y. Zhu, M. Tang, X. Shi, and Y. Zhao, "Quantum chemical study of cyclic dipeptides," *International Journal of Quantum Chemistry*, vol. 107, no. 3, pp. 745–753, 2007.
- [24] M. J. Frisch, G. W. Trucks, H. B. Schlegel et al., *Gaussian 03, revision C.02*, Gaussian, Inc., Wallingford, Conn, USA, 2004.
- [25] A. D. Becke, "Density-functional exchange-energy approximation with correct asymptotic behavior," *The Journal of Chemical Physics*, vol. 98, pp. 5648–5652, 1993.
- [26] C. Lee, W. Yang, and R. G. Parr, "Development of the Colle-Salvetti correlation-energy formula into a functional of the electron density," *Physical Review B*, vol. 37, no. 2, pp. 785–789, 1988.
- [27] R. S. Mulliken, "Electronic population analysis on LCAO–MO molecular wave functions. I," *The Journal of Chemical Physics*, vol. 23, no. 10, pp. 1833–1840, 1955.
- [28] G. Scalmani and V. Barone, "Use of molecular symmetry in the computation of solvation energies and their analytical derivatives by the polarizable continuum model," *Chemical Physics Letters*, vol. 301, no. 3–4, pp. 263–269, 1999.
- [29] M. W. Wong, B. K. Wiberg, and M. J. Frisch, "Medium effect on the structure, energy, charge density, and vibrational frequencies of sulfamic acid," *Journal of the American Chemical Society*, vol. 114, pp. 523–529, 1992.

Research Article

Influence of Nanocomposites of LDPE Doped with Nano-MgO by Different Preparing Methods on Its Dielectric Properties

Wenlong Zhang,^{1,2} Yajie Dai,^{1,2} Hong Zhao,^{1,3} and Lidong Zhong⁴

¹Key Laboratory of Engineering Dielectric and Its Application, Ministry of Education, Harbin University of Science and Technology, Harbin, Heilongjiang 150080, China

²College of Material Science & Engineering, Harbin University of Science and Technology, Harbin, Heilongjiang 150040, China

³College of Electrical and Electronic Engineering, Harbin University of Science and Technology, Heilongjiang 150080, China

⁴Zhongtian Technology Group Ltd., Nantong, Jiangsu 226000, China

Correspondence should be addressed to Hong Zhao; hongzhao@hrbust.edu.cn

Received 20 August 2014; Revised 2 November 2014; Accepted 18 November 2014

Academic Editor: Jian Sun

Copyright © 2015 Wenlong Zhang et al. This is an open access article distributed under the Creative Commons Attribution License, which permits unrestricted use, distribution, and reproduction in any medium, provided the original work is properly cited.

LDPE doped with nano-MgO can effectively suppress the space charge accumulation in the nanocomposite under DC applied field, and this suppression was affected greatly by the prepared nano-MgO particles. In this paper, the influence of nanocomposite of LDPE doped with nano-MgO by using different preparation methods on their space charge, and volume resistivity as well as DC breakdown strength was researched. The results showed that size of nano-MgO prepared by the traditional heating method was about 22.74 nm, while being only about 12.76 nm by the microwave-assisted method. When the nano-MgO content in the composite was 2 wt% by weight, the space charge accumulation in this composite was obviously reduced; meanwhile both the volume resistivity and DC breakdown strength were enhanced. When nano-MgO was prepared by the microwave-assisted method, the electric properties of its LDPE nanocomposite were obviously better than those of nano-MgO prepared by traditional heating method.

1. Introduction

The contradiction between urban expansion and electricity demand is becoming more prominent. Long distance and effective and safe power transmission are the main developing direction to solve the conflict. Comparing direct current (DC) transmission with alternative current (AC) transmission, it has advantages of the lower line cost, lower power loss, transmission system stability, and so forth. But DC transmission of cross-linked polyethylene (XLPE) cable was hampered by its own shortcomings in which there is a lot of space charge accumulation leading to distorting electric field and even local electric breakdown of insulator of XLPE cable [1, 2]. It was surprising that base polyethylene (base PE) doped with nano-MgO particles can effectively suppress the space charge accumulation. At the same time the composite still has excellent electrical properties. So researches of the dielectric polymer nanocomposite have become one of hot spots in electric power field [3].

Nanoparticles are generally agglomerated as a result of their high surface energy and therefore the disaggregation of nanoparticles in nanocomposites proves to be a key issue in obtaining good filler dispersion and to bring the nanoparticles into full play. However, there is different dispersion effect for the nanoparticles with different preparation methods. Nano-MgO particles prepared with direct precipitation method and homogeneous precipitation method as well as microwave-assisted method were researched in this paper. Nano-MgO particles prepared with direct precipitation method and homogeneous precipitation method have poor dispersion and serious aggregation. However, the microwave-assisted method has been used to prepare nanooxides, which has good dispersion and disaggregation, and so forth [4–6]. This paper systematically researched the fact that nano-MgO particle was prepared by microwave-assisted method and the influence of nano-MgO particles by different preparation methods on size, dispersion of nano-MgO, and dielectric properties of its nanocomposite.

2. Experimental Procedure

2.1. Experimental Raw Materials. Magnesium nitrate hexahydrate ($\text{MgNO}_3 \cdot 6\text{H}_2\text{O}$) (Tianjin Guangfu Fine Chemical Research Institute, China), aqueous ammonia (37 wt%) (Bazhou Chemical Plants, China), polyethylene glycol (PEG200) (Tianjin Regent Chemicals Co., Ltd.), urea [$\text{CO}(\text{NH}_2)_2$] (Tianjin Chemical Reagent Co., Ltd., China), ammonium bicarbonate (Bazhou City Chemical Plant, Hubei China), LDPE (BW150, BASF YPC Co., Ltd., China), and EVA (EF-443, 14%, LG Chemical Company, South Korea) are used in this research.

2.2. Preparation of $\text{Mg}(\text{OH})_2$

2.2.1. Direct Precipitation Method. $\text{MgNO}_3 \cdot 6\text{H}_2\text{O}$ was dissolved in distilled water (200 mL) to prepare a solution of certain concentration (0.2 mol/L) in a three-necked bottle. Then appropriate amount of aqueous ammonia was put into the three-necked bottle drop by drop at starting heating by a sheathed heater. White precipitate powder began to occur after dropwise addition of aqueous ammonia in the solution of the flask. After maintaining a certain period of time for heating the solution, the white precipitate powder was washed with water and alcohol and then $\text{Mg}(\text{OH})_2$ powder was obtained. See [7, 8].

2.2.2. Homogeneous Precipitation Method. $\text{MgNO}_3 \cdot 6\text{H}_2\text{O}$ was dissolved in distilled water (200 mL) to prepare a solution of certain concentration (0.2 mol/L) in a three-necked bottle. Then, magnesium nitrate aqueous solution was put into a three-necked flask. Once heated, a small amount of PEG dispersant (0.1 mL) was added into the flask and then stirred for 5 min; finally, urea (1.0 g) was added according to the predetermined ratio. After 6 h reaction at 125°C , a white precipitate was formed which was washed by water and alcohol, respectively, with filtration devices. Then the precipitate was put into a vacuum dry oven (at 80°C , 24 h) to dry to obtain $\text{Mg}(\text{OH})_2$ powder. See [9].

2.2.3. Microwave-Assisted Method. A certain amount of ammonium bicarbonate accompanied with a small amount of PEG200 (1 mL) was dissolved in distilled water (20 mL). Then the three-necked flask containing the solution was heated by microwave oven under 80°C , 625 W for 30 min. Then, magnesium nitrate solution was added into the flask step by step with a separatory funnel at a fixed speed of dropping in accordance with the addition of molar ratio (1 : 4) of magnesium nitrate and ammonium bicarbonate. A white precipitate was produced at 50 min and 80°C . And washed it with water and alcohol, respectively, with suction device. Finally, the precipitate was put into a vacuum dry oven (at 80°C , 24 h) to dry to obtain $\text{Mg}(\text{OH})_2$ powder.

2.3. Preparation of Surface Coupling Treatment of Nano-MgO. Nano-MgO was prepared by stepwise calcination. First, $\text{Mg}(\text{OH})_2$ was put into the muffle furnace and calcinated at the temperature of $300\text{--}400^\circ\text{C}$ for 1 hour. Then, it was taken out for ball milling in planetary ball mill at rotating speed of

200 rpm for 20 min (forward 10 min, reverse 10 min, resp.). Secondly, it was put into muffle furnace and calcinated again at the temperature of 500°C for 2 hours. Then it was fetched out and the nano-MgO powder was obtained. Nano-MgO particles' surface was treated with silane coupling agent [KH-550, $\text{NH}_2\text{CH}_2\text{CH}_2\text{CH}_2\text{Si}(\text{OC}_2\text{H}_5)_3$, 2 wt% of the particle loading] at about 60°C for 16 min (forward 8 min, reverse 8 min, resp.) using ball milling at a ball speed of 140 rpm.

2.4. Preparation of LDPE Nanocomposite. LDPE (40 g) and nano-MgO particle treated by using silane coupling agent (2 wt%, nano-MgO prepared by microwave-assisted method or direct precipitation method or homogeneous precipitation method, resp.) were blended to prepare three kinds of nanocomposites at 150°C and 80 rpm for 15 min in the mixer of torque rheometer. During the blending process, ethylene-vinyl-acetate copolymer (EVA, 9 wt% of LDPE loading) was added into the mixer in order to further improve the dispersibility between nano-MgO and LDPE in the nanocomposite.

2.5. Analysis by SEM. As for sample of the composite, it must be broken into small pieces, whereas the powder of MgO can be used directly. The brittle fracture processing of the composite sample was carried out in liquid nitrogen. After that, the fragments of nanocomposite sample or the nano-MgO powders were fixed on the tin block with conductive adhesive and then coated with gold. Finally, the dispersion and size of nano-MgO particles were observed by using a scanning electron microscope (SEM, FEI Sirion 200, Dutch Philips Co., Ltd.).

2.6. XRD Test Method. The size of nano-MgO powder was analyzed by X-ray diffractometer (XRD, model D/max 2500, Rigaku Co., Ltd., Japan), whose scanning speed was $4^\circ/\text{min}$ and angle range was $10^\circ\text{--}90^\circ$. The size of nano-MgO powder was calculated according to the Scherrer formula:

$$D = \frac{K\lambda}{(L \cos \theta)}. \quad (1)$$

In the formula, $K = 0.89$ and $\lambda = 0.15406 \text{ nm}$. L stands for width at half-intensity diffraction line degree; θ for a diffraction angle ($^\circ$); D for grain size (nm).

2.7. Volume Resistivity Test. Volume resistance test of the composite specimen slice which was about 1 mm in thickness was carried by digital resistance meter (ZC-36) under testing voltage being 1000 V applied to specimen slice at three-electrode system (Figure 1), and the volume resistivity was calculated according to formula (2), in which ρ_v ($\Omega \cdot \text{m}$) was the resistivity, R_v (Ω) the composite volume resistance, d_1 (m) the protested electrode diameter, g (m) the electrode gap between the protested electrode and the shield electrode, and h (m) the specimen thickness:

$$\rho_v = R_v \frac{\pi (d_1 + g)^2}{4h}. \quad (2)$$

TABLE 1: The volume resistivity of the composites.

| Item | Base LDPE | LDPE doped with MgO prepared by microwave method | LDPE doped with MgO prepared by direct precipitation method | LDPE doped with MgO prepared by homogeneous precipitation method |
|---|-----------------------|--|---|--|
| Volume resistivity/ $\Omega\cdot\text{m}$ | 8.49×10^{12} | 1.23×10^{15} | 1.27×10^{14} | 2.33×10^{14} |

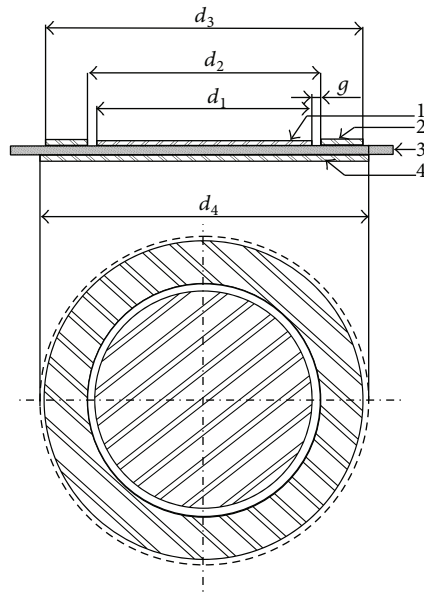


FIGURE 1: Three-electrode system. (1) Protected electrode, (2) shield electrode, (3) specimen slice, and (4) no protecting electrode; (d_1) protected electrode diameter (50 mm), (d_2) shield electrode inner diameter (54 mm), (d_3) shield electrode external diameter (74 mm), and (d_4) no protecting electrode diameter (≥ 74 mm). (g) electrode gap between the protected electrode and shield electrode (2 mm).

2.8. DC Breakdown Strength Test. The composite circular specimen slice (the sample thickness of $100 \mu\text{m}$, the diameter of about 10 cm) was put into transformer oil. Breakdown field value was detected by the breakdown voltage tester (HT-100) and at continuous elevating speed voltage of 3 kV/s.

2.9. Space Charge Test. Space charge in the sample was tested by pulsed electro-acoustic-01 (PEA-01) under the strength of electric field being 40 kV/mm.

3. The Results and Discussion

3.1. SEM Analysis of Nano-MgO. Nano-MgO was made from $\text{Mg}(\text{OH})_2$ by two-step calcination method in muffle furnace, whereas the $\text{Mg}(\text{OH})_2$ was made by microwave-assisted method, direct precipitation method, and homogenous precipitation method, respectively. The dispersion and size of the nano-MgO particles made by three methods were observed by using scanning electron microscope (SEM), as shown in Figures 2(a), 2(b), and 2(c). The results indicated that the diameter size of MgO particle prepared by microwave-assisted method was about 49 nm, which was the minimum

of the nano-MgO particles and disperses uniformly among three methods. In addition, the particles agglomeration phenomenon was not obvious (see Figure 2(a)), while the diameter size of MgO particle prepared by direct precipitation method was beyond the nanometer size, and it had serious agglomeration phenomenon (see Figure 2(b)).

The diameter size of MgO powder prepared by homogeneous precipitation method ranges from 70 to 90 nm and it had obvious agglomeration (see Figure 2(c)). The reasons may be that the uniformity of particle size is influenced by multiple nucleation of precipitate phase. Different from the direct precipitation method and homogeneous precipitation method, the microwave-assisted method can provide uniform heat in a very short period of time to greatly eliminate the temperature gradient and instantaneously nucleate for precipitate phase of $\text{Mg}(\text{OH})_2$ which was calcined by two-step method in muffle furnace to obtain uniform distribution and dispersion of nano-MgO particles.

3.2. XRD Analysis of Nano-MgO. The nano-MgO powder prepared by microwave-assisted was compared with conventional heating methods by using X-ray diffraction (XRD) in Figure 3. The 2θ values of the diffraction peaks of nano-MgO particles prepared by microwave-assisted method and conventional method were basically the same and the crystals were both cubic crystal structure from Figure 3. According to Scherer formula (1) calculation, the size of nano-MgO prepared by microwave-assisted method was about 12.76 nm, and the traditional one was 22.74 nm.

3.3. Influence of Nano-MgO Preparation Method on the Volume Resistivity of Composites. The nano-MgO loading was fixed at 2 wt%, and nano-MgO prepared by different methods was doped into LDPE. The impact on the volume resistivity of composites was investigated and the results were shown in Table 1.

As can be seen from Table 1, after LDPE doped with MgO nano-MgO was prepared by microwave-assisted method, the volume resistivity of composites was the maximum. The reason may be attributed to the good dispersion of nano-MgO in LDPE matrix. Nano-MgO can limit the movement of molecular chain effectively, forming a lot of traps, and enhance the ability to capture charge under applying the electric field. Therefore, the volume resistivity of composites was higher than other nano-MgO composites [10, 11].

3.4. Effect of Nano-MgO by Prepared Methods on the DC Breakdown Strength of Composite. The nano-MgO loading was fixed as 2 wt%; using nano-MgO by different preparation methods in LDPE matrix, the impact on DC breakdown

TABLE 2: DC breakdown strength of the composites.

| Item | Base LDPE | LDPE doped with MgO prepared by microwave method | LDPE doped with MgO prepared by direct precipitation method | LDPE doped with MgO prepared by homogeneous precipitation method |
|--------------------------|-----------|--|---|--|
| Breakdown strength/kV/mm | 260.9 | 310.0 | 263.3 | 270.4 |

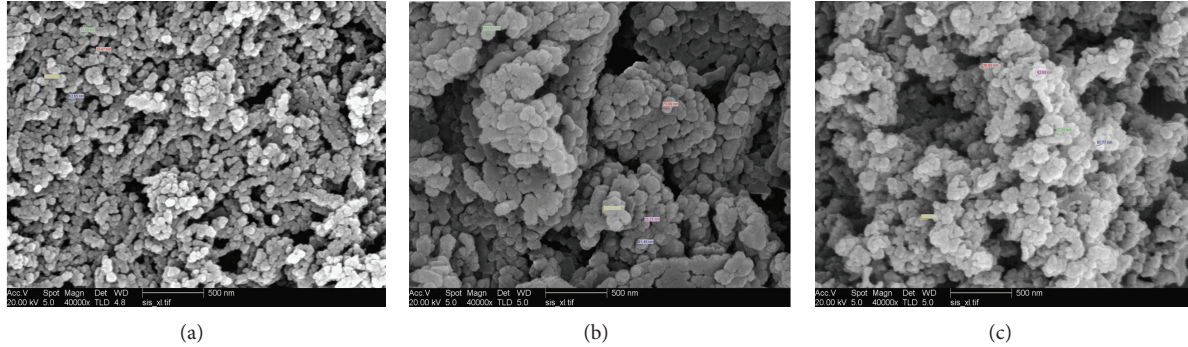


FIGURE 2: (a) Nano-MgO by microwave-assisted method; (b) nano-MgO by direct precipitation method; (c) nano-MgO by homogenous precipitation method.

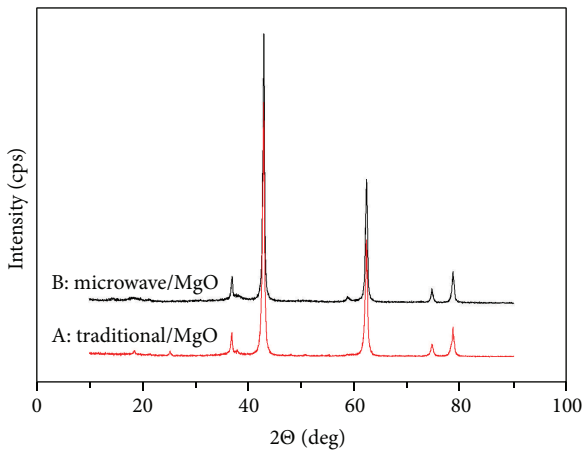


FIGURE 3: XRD pattern of nano-MgO prepared by microwave-assisted and conventional methods, respectively.

strength of the composite was investigated. The results were shown in Table 2.

As can be seen from Table 2, DC breakdown strength of the composites has increased in comparison with LDPE without adding nano-MgO. However, the LDPE blended with MgO prepared by microwave-assisted method has the maximum DC breakdown field strength due to its perfect dispersion. There was the Coulomb blockade effect, which will limit the directional movement of carriers. On the other hand, it will result in LDPE matrix stretched to a certain extent. Stretching causes the lattice of LDPE dislocations which produce more and deeper traps. At the same time, the ability to trap electrons will be enhanced [12].

3.5. Influences of Nano-MgO Preparation Methods on Space Charge in the Composites. Nano-MgO was fixed at 2 wt% by

weight. Using of nano-MgO blended with LDPE to form the composite, the effect of the space charge distribution on the composite was investigated. The experimental results were shown in Figure 4.

From Figure 4(a), it can be seen that base LDPE has a large number of homocharges injected near the cathode and anode. Comparing Figure 4(b) with Figures 4(c) and 4(d), composite doped with nano-MgO prepared by microwave-assisted method has the anode and cathode without the homocharges injected. It almost has no space charge in the sample with effective effect to suppress space charge in composite. This may be attributed to the fact that the diameter of nano-MgO prepared by microwave-assisted method was small and well distributed in the composite due to good compatibility with LDPE matrix. It will enhance the charge injection barrier and at the same time reduce the mobility of the charge because of the particle surface charge layer effects. So the effect of space charge suppression was the best [2, 3].

4. Conclusions

In this paper, nano-MgO prepared by microwave-assisted method was compared with ones prepared by conventional methods. The former has smallest particle size and no obvious agglomeration. Electric properties of LDPE doped with the nano-MgO prepared by microwave-assisted method have been greatly improved by contrast with LDPE doped with the nano-MgO prepared by conventional method.

Conflict of Interests

The authors declare that there is no conflict of interests regarding the publication of this paper.

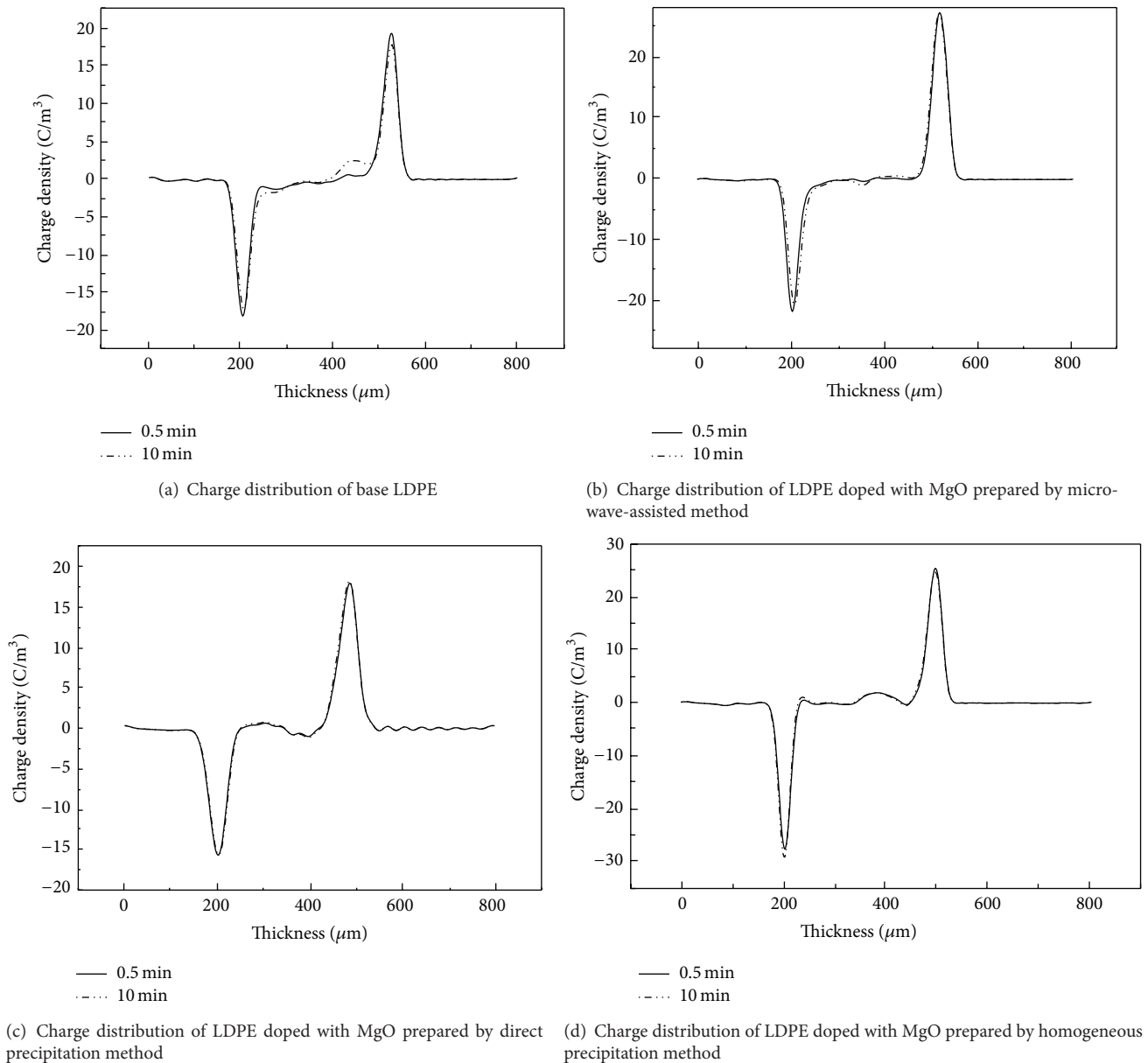


FIGURE 4: Charge distribution of base LDPE and its nano-MgO composite.

Acknowledgment

The authors thank National Science Foundation of China (Grant no. 51337002) for their financial support.

References

- [1] I. L. Hosier, A. S. Vaughan, and S. G. Swingler, "An investigation of the potential of ethylene vinyl acetate/polyethylene blends for use in recyclable high voltage cable insulation systems," *Journal of Materials Science*, vol. 45, no. 10, pp. 2747–2759, 2010.
- [2] G. C. Montanari and P. H. F. Morshuis, "Space charge phenomenology in polymeric insulating materials," *IEEE Transactions on Dielectrics and Electrical Insulation*, vol. 12, no. 4, pp. 754–767, 2005.
- [3] K. Wu, X. Chen, X. Wang et al., "Research of polyethylene nanocomposites for HVDC cables," *Insulation Materials*, vol. 43, no. 4, pp. 1–2, 2010.
- [4] D.-z. Wang, Y.-j. Sun, X.-y. Liu et al., "The process research on preparation of nano-Magnesia," *Powder Metallurgy Industry*, vol. 22, no. 6, pp. 49–52, 2012.
- [5] Y. Li, P. Wang, and H. L. Cao, "Microwave assisted synthesis of n-butyl lactate catalyzed by acid-activated montmorillonite clay," *Material Science and Technology*, vol. 20, no. 1, pp. 49–57, 2012.
- [6] H. Wang, P. Wang, and J.-F. Zhang, "Photocatalysis activity and preparation of Fe-doped TiO₂ hydrosol by microwave irradiation peptization," *Material Science and Technology*, vol. 18, no. 4, pp. 545–554, 2010.

- [7] Z.-Q. Liu, L.-J. Li, Z.-M. Zeng, F. Nie, L.-Y. Chai, and Y.-F. Chen, "Preparation of monodispersed and hexagonal magnesium hydroxide from bischofite," *Materials Science and Technology*, vol. 19, no. 8, pp. 138–143, 2011.
- [8] K. Xu, B.-L. Zhang, C.-H. Hou et al., "Review on nano-magnesia preparation technology," *Inorganic Chemicals Industry*, vol. 39, no. 6, pp. 7–9, 2007.
- [9] W.-L. Zhang, J.-W. Xu, C. Ji et al., "Preparation of nano-magnesia by homogeneous precipitation," *Journal of Harbin University of Science and Technology*, vol. 15, no. 6, pp. 112–115, 2010.
- [10] S.-Q. Chen, X. Chen, X. Wang et al., "Study of space charge distribution and volume resistivity in composite of polyethylene/nano zinc oxide," *Insulation Materials*, vol. 40, no. 2, pp. 48–53, 2007.
- [11] Y. Murakami, M. Nemoto, S. Okuzumi et al., "DC conduction and electrical breakdown of MgO/LDPE nanocomposite," *IEEE Transactions on Dielectrics and Electrical Insulation*, vol. 15, no. 1, pp. 33–38, 2008.
- [12] Y. Wang, M. Xu, Y. Sun et al., "Study on the resistance and electrical breakdown properties of nano silver/epoxy resin composite," *Insulation Materials*, vol. 39, no. 4, pp. 37–40, 2006.

Review Article

Mussel-Inspired Polydopamine Coated Iron Oxide Nanoparticles for Biomedical Application

Xiangling Gu, Yancong Zhang, Hanwen Sun, Xinfeng Song, Chunhua Fu, and Pingxuan Dong

Shandong Provincial Engineering Laboratory of Novel Pharmaceutical Excipients, Sustained and Controlled Release Preparations, Dezhou University, Dezhou 253023, China

Correspondence should be addressed to Hanwen Sun; hanwen916@163.com

Received 16 October 2014; Revised 25 December 2014; Accepted 25 December 2014

Academic Editor: William W. Yu

Copyright © 2015 Xiangling Gu et al. This is an open access article distributed under the Creative Commons Attribution License, which permits unrestricted use, distribution, and reproduction in any medium, provided the original work is properly cited.

Mussel-inspired polydopamine (PDA) coated iron oxide nanoparticles have served as a feasible, robust, and functional platform for various biomedical applications. However, there is scarcely a systemic paper reviewed about such functionalising nanomaterials to date. In this review, the synthesis of iron oxide nanoparticles, the mechanism of dopamine self-oxidation, the interaction between iron oxide and dopamine, and the functionality and the safety assessment of dopamine modified iron oxide nanoparticles as well as the biomedical application of such nanoparticles are discussed. To enlighten the future research, the opportunities and the limitations of functionalising iron oxide nanoparticles coated with PDA are also analyzed.

1. Introduction

Magnetic iron oxide nanoparticles are of great interest due to the unique properties stemmed from their extremely small size and large specific surface area [1]. They have been extensively investigated in recent years for the promising biomedical applications, such as drug delivery [2, 3], immunoassay analyzer [4, 5], magnetic resonance imaging [6, 7], and cancer hyperthermia [8]. For most of these applications, surface modification of iron oxide nanoparticles plays an important role in improving their hydrophilicity, colloidal stability, biocompatibility, and conjugation of bioactive functional groups. To this end, many materials have been employed to design stable surface coatings for iron oxide nanoparticles, such as polymers, surfactants, or inorganic shells [9, 10]. Surface modification of magnetic nanoparticles is mainly aiming at how to render their functionality and to control their solubility. For biomedical applications and bioanalysis, the ability to solubilize the nanoparticles in water and to modify their surfaces with molecules, proteins, oligonucleotides, or other targeting agents is a crucial step toward their widespread use [11]. However, the cumbersome and harsh conditions, such as toxic organic solvents

utilized as reaction media, are often seemed as the barriers to the modification processes. Therefore, surface modification with aforementioned materials is still a challenge so far to us, which appeals for a facile, feasible, and aqueous approach to achieve controllable surface coatings for iron oxide nanoparticles.

Nowadays, dopamine and its derivatives have enjoyed success as agents for the masking of magnetic nanoparticles, often so as to provide their biocompatibility with medium to long-term colloidal stability in the various biological milieu [12]. Recently, Lee et al. pioneered a one-step formation of robust adherent polydopamine (PDA) films based on mussel-inspired polymerization of dopamine at alkaline pHs on various substrates [13]. Because of the ease of the use as well as its fascinating properties, PDA has attracted great interest for wide applications. Notably, the application of PDA to iron oxide nanoparticles has emerged as a particularly important field. Controllable PDA films can be formed on the iron oxide nanoparticles by simply dispersing them in an alkaline dopamine solution and mildly stirring at room temperature [9]. Dopamine derivatives provide a novel and useful alternative for surface immobilization schemes. For example, dopamine derivatives have been used to anchor

small functional biomolecules onto ferromagnetic nanoparticles for protein separation [14, 15]. Obviously, dopamine and its derivatives open a new route to the modification of iron oxide nanoparticles [16].

In this review, certain aspects on PDA coated iron oxide nanoparticles, including the synthesis of iron oxide nanoparticles, the mechanism of self-oxidation of dopamine, the interaction between iron oxide nanoparticles and dopamine, and the functionality and safety assessment of dopamine modified iron oxide nanoparticles as well as their biomedical application, are discussed. The opportunities and the limitations of functionalising the surfaces of iron oxide nanoparticles coated with PDA are also analyzed.

2. Synthesis of Iron Oxide Nanoparticles

The quality of iron oxide nanoparticles, such as crystallization, size, and shape, highly depends on the synthesis approaches, which can produce well-crystallized and size-controlled iron oxide nanoparticles and offer more opportunities for their biomedical applications. Among all the chemical synthesis methods, hydrothermal may be one of the most widely reported [17, 26, 27]. In such method, a relative high temperature and a high pressure were often employed to induce or affect the formation of nanocrystals. The advantages of this method, such as high reactivity of the reactants, facile control of product morphology, and good crystallization of products, are apparent. Ge et al. reported a one-step hydrothermal approach to the synthesis of iron oxide nanoparticles with controllable diameters from 15 to 31 nm, narrow size distribution, and high saturation magnetization in the range of 53.3–97.4 emu/g, in the presence of $\text{FeCl}_2 \cdot 4\text{H}_2\text{O}$ in basic aqueous solution under an elevated temperature and pressure [17] (see Figure 1). With $\text{FeSO}_4 \cdot 7\text{H}_2\text{O}$ and FeCl_3 as precursors and NaOH as hydrolysis reactant, Kholam et al. achieved spherical iron oxide nanoparticles with a size range of 150–200 nm via a microwave hydrothermal reaction [26]. Obviously, the solubility of reactants and desired products via this method is critical.

Coprecipitation is another one of most widely reported methods to fabricate iron oxide nanoparticles [18, 28, 29]. In general, an alkaline solution, such as NaOH and $\text{NH}_3 \cdot \text{H}_2\text{O}$, was often employed to precipitate Fe^{2+} and Fe^{3+} ions in an aqueous solution. Due to the nanoparticles achieved by dehydration from the intermediate iron hydroxides, the surfaces of as-prepared nanoparticles were covered with large number of hydroxyl groups and the nanoparticles could be well suspended in an aqueous solution. Roth et al. prepared superparamagnetic iron oxide nanoparticles with size between 3 and 17 nm and saturation magnetizations from 26 to 89 emu/g via coprecipitation. They found that particle saturation magnetization could be enhanced by addition of more iron salt into the reaction system and employment of a molar ratio of $\text{Fe}^{3+}/\text{Fe}^{2+}$ below 2:1 [28]. Basuki et al. reported their work to prepare magnetic nanoparticles with in situ coprecipitation of Fe^{2+} and Fe^{3+} ions in aqueous solutions in the presence of functional block copolymers.

They varied the ratio of copolymer to Fe to wield control over nanoparticle diameters within the range of 7–20 nm. They found that the amount of polymer employed during the coprecipitation proved critical in governing crystallinity and colloidal stability [18] (see Figure 2). In addition, Xia et al. developed a complex-coprecipitation method to synthesize iron oxide nanoparticles with triethanolamine as ligands to govern the quality of iron oxide nanoparticles. In this case, triethanolamine was used mainly for limiting nanoparticles growing rate due to its chelation to Fe^{3+} and Fe^{2+} [29]. Because the most coprecipitation reactions carried out at low temperature and their reaction kinetics can be only controlled by changing reactants, it is difficult to optimize the size and size distribution of nanoparticles and to achieve high crystalline or control the particle shape in coprecipitation route.

Recently, high-temperature decomposition of organometallic precursors was found to be one of the most efficient approaches to fabricate iron oxide nanoparticles with well-controlled size and shape [30–33]. Sun and Zeng gave the first report on iron oxide nanoparticles preparation by thermal decomposition of $\text{Fe}(\text{acac})_3$ in the presence of surfactants, oleylamine, and oleic acid. With this method, uniform iron oxide nanoparticles with size between 4 and 16 nm were achieved [30]. Kucheryavy et al. synthesized magnetite nanoparticles in the size range of 3.2–7.5 nm with high yields using high-temperature hydrolysis of the precursor Fe^{2+} and Fe^{3+} ions alkoxides in diethylene glycol solution. The average sizes of the particles were adjusted by changing the reaction temperature and time and by using a sequential growth technique [31]. Alternatively, Fe-oleate complex was also employed as the precursor for large scale synthesis, up to 40 g of iron oxide nanoparticles obtained in a single reaction, by Park et al. [32]. Moreover, the work that iron oxide nanoparticles with 4.5 nm core size were synthesized by thermal decomposition of $\text{Fe}(\text{CO})_5$, followed by air oxidation with a ligand 4-methylcatechol, was also reported by Xie et al. [33].

3. Self-Oxidation of Dopamine on Iron Oxide Nanoparticles and Their Interaction

Dopamine, known as a small-molecule mimic of the adhesive proteins of mussels, is liable to be oxidized to generate a thin PDA layer on iron oxide nanoparticles surface (see Figure 3) [19]. At a weak alkaline solution, dopamine is susceptible to undergo self-oxidation to produce adherent PDA coatings on virtually any substrates and catechol groups are oxidized to the quinone form [13, 25, 34]. The catechol functionality of dopamine is primarily responsible for moisture-resistant adhesion and the oxidized o-quinone functionality is primarily responsible for cross-linking [35]. Virtually any substrate can be functionalized by first depositing PDA followed by secondary derivation reaction including self-assembled monolayers through the deposition of long-chain molecular building blocks, metal films by electroless metallization, bioactive functionalities, and even cross-linking reaction [19].

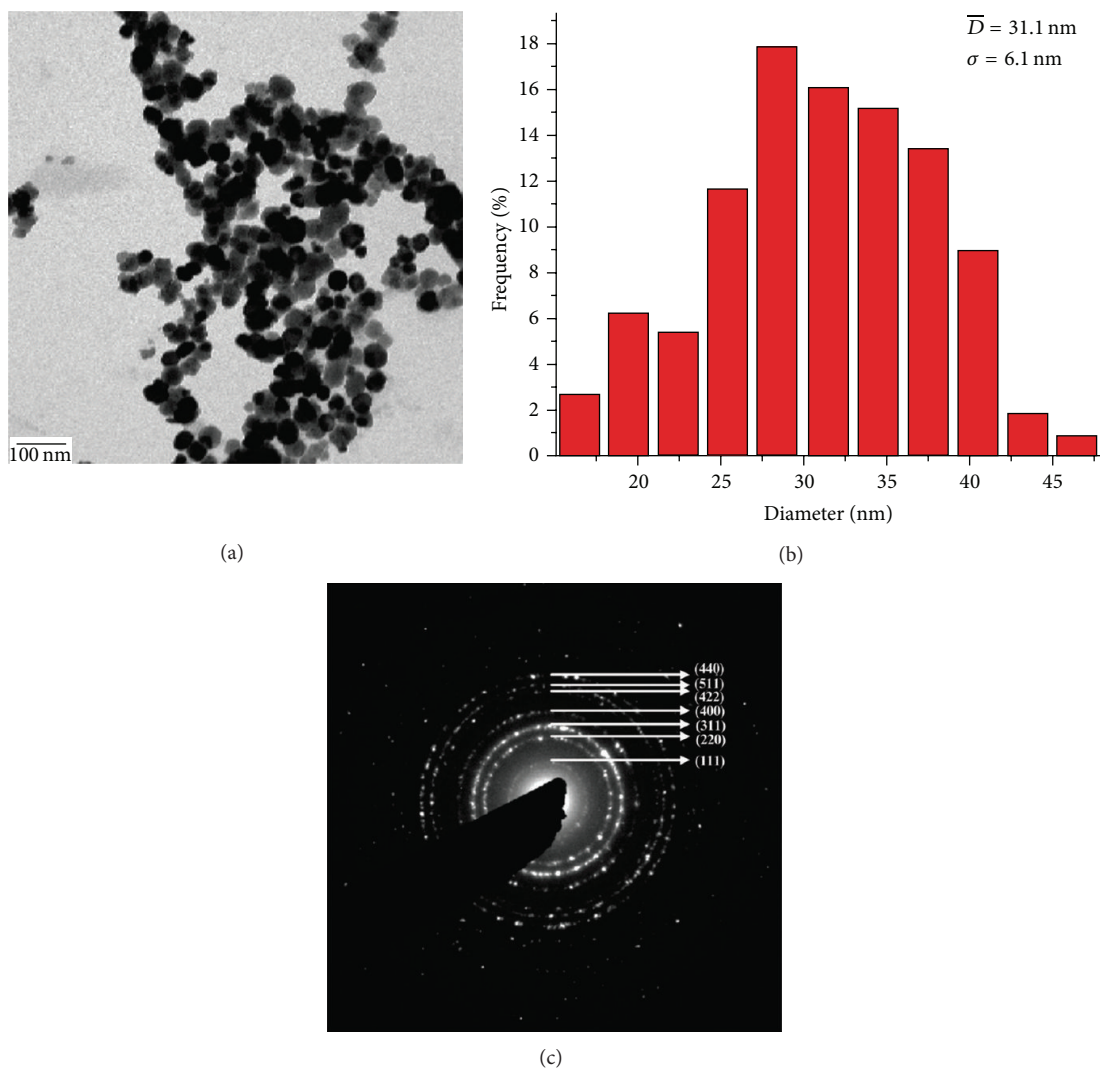


FIGURE 1: A typical TEM image (a), size distribution histogram (b), and SAED pattern (c) of iron oxide nanoparticles [17].

Shultz and his coworkers [20] found that an initial PDA structure formed with coordination to the surface of magnetic nanoparticle resulted from improved orbital overlap of the five-membered ring and a reduced steric environment of the iron complex (see Figure 4). A semiquinone is therefore formed via transfer of electrons to the iron cations on the surface and rearrangement of the oxidized dopamine. Oxygen on the surface was liable to be protonated because of free protons in the system and form Fe^{3+} in the aqueous solution. Consequently, the reactivity between Fe^{3+} and dopamine quickly facilitates the degradation of the nanoparticles.

The solvents also play an important role in the self-oxidation of dopamine. The presence of ethanol is found to significantly slow down the polymerization rate of dopamine and make the surface modification of nanomaterials with PDA more controllable in comparison to the water-phase polymerization [21, 36]. PDA can provide a simple and versatile method for surface modification of iron oxide nanoparticles and a promising building block towards functional materials (see Figure 5).

The interaction between PDA and iron oxide nanoparticles has been widely investigated by many groups. The method of Park and coworkers [32] was used for the preparation of iron oxide nanoparticles from iron(III) oleate. Mussel adhesive protein served as the inspiration for their surface coatings, which was composed of a polysaccharide containing pendant dopamine anchors. This composite ligand made use of multiple surface-dopamine interactions for surface attachment. Due to the large difference in the affinities of PDA-hyaluronic acid and oleic acid for the particle surface, the initial electrostatic interaction between the positively charged particle layer and the ligand-conjugate was replaced by a covalent interaction between the particle surface and the dopamine catecholates. Amstad et al. [22] synthesized dopamine derivative anchor groups possessed irreversible binding affinity to iron oxide which can optimally disperse magnetic nanoparticles under physiologic conditions. This not only leads to ultrastable iron oxide nanoparticles but also allows close control over the hydrodynamic diameter and interfacial chemistry (see Figure 6). Iron(III) in solution

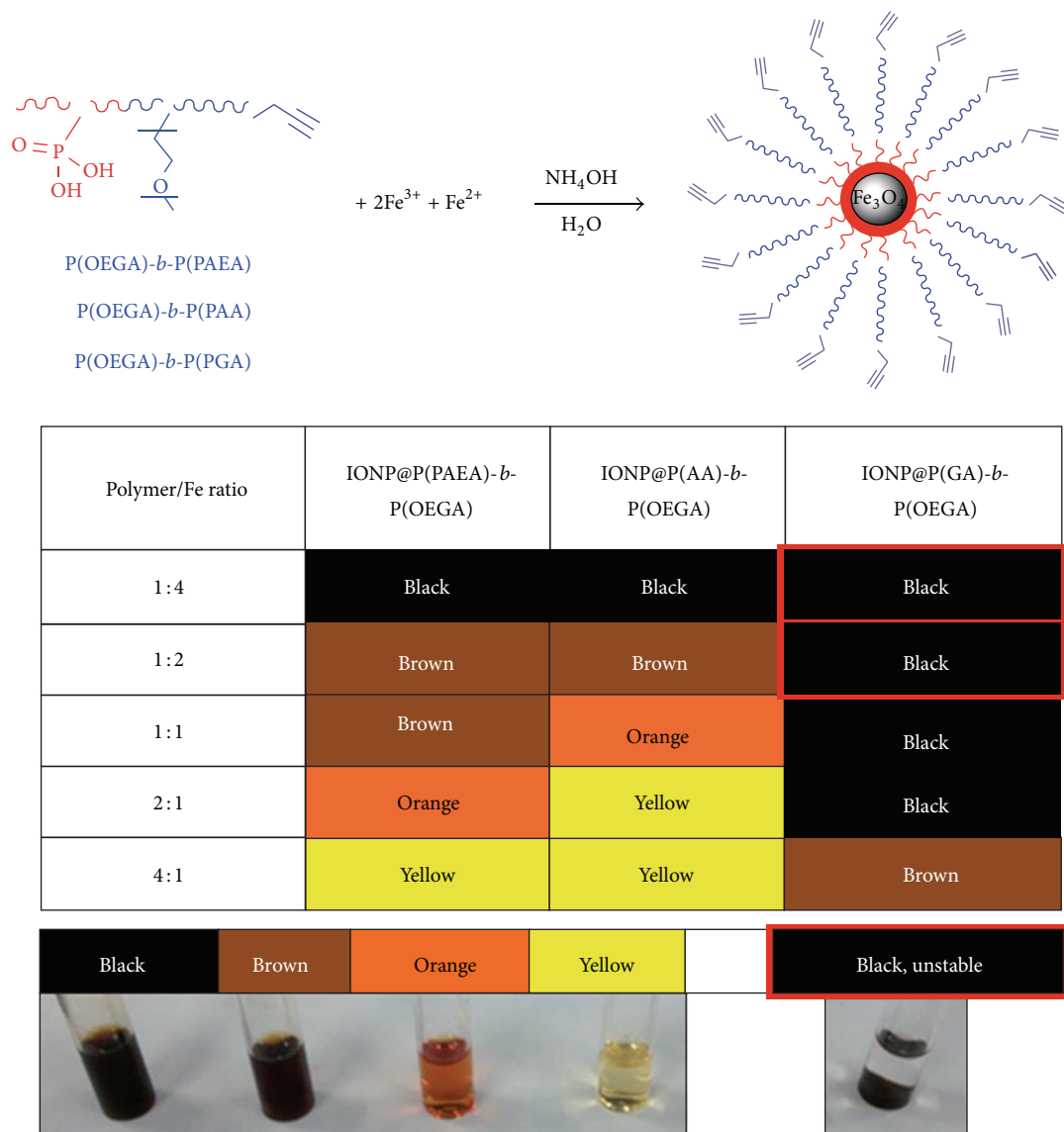


FIGURE 2: In situ coprecipitation of IONPs at different polymer-to-iron ratio [18].

forms extremely stable complexes with bidentate dopamine. For example, a stability constant of 1044.9 has been determined for the octahedral complex. Given the large stability constants for these complexes, it is no doubt that catecholate groups are found in siderophores, molecules which evolved to sequester iron from the external environment and in adhesive proteins. Hence the widespread use of dopamine-derived surface modification for iron oxide nanoparticles functionalisation is based on the well-studied bonding interactions in iron dopamine complexes [12].

4. Functionality of PDA Coated Iron Oxide Nanoparticles

As mentioned above, PDA provides a number of advantages, such as ease and convenience to modification on

iron oxide nanoparticles for further functionalization with biomolecules, chemical reactivity, near-infrared absorption, and high fluorescence quenching efficiency [37–39]. Besides, PDA film exhibits a special zwitterionicity: PDA layer is positively charged and allows good permeability of negatively charged small molecules at low pH, while it is negatively charged and allows good permeability of positively charged molecules at high pH. The fully reversible and pH-switchable permselectivity may be conferred with potential applications in drug delivery or other biomedical applications [40]. PDA shell can also be further surface functionalized to improve selective recognition with cells [41, 42]. PDA coatings with significant ability of enhancing the adhesion and proliferation of cells show good biocompatibility and promise for tissue engineering [43, 44]. PDA-coated iron oxide nanoparticles were also proved to have negligible cytotoxicity [45]. Furthermore, the functional properties of nanoparticles, including

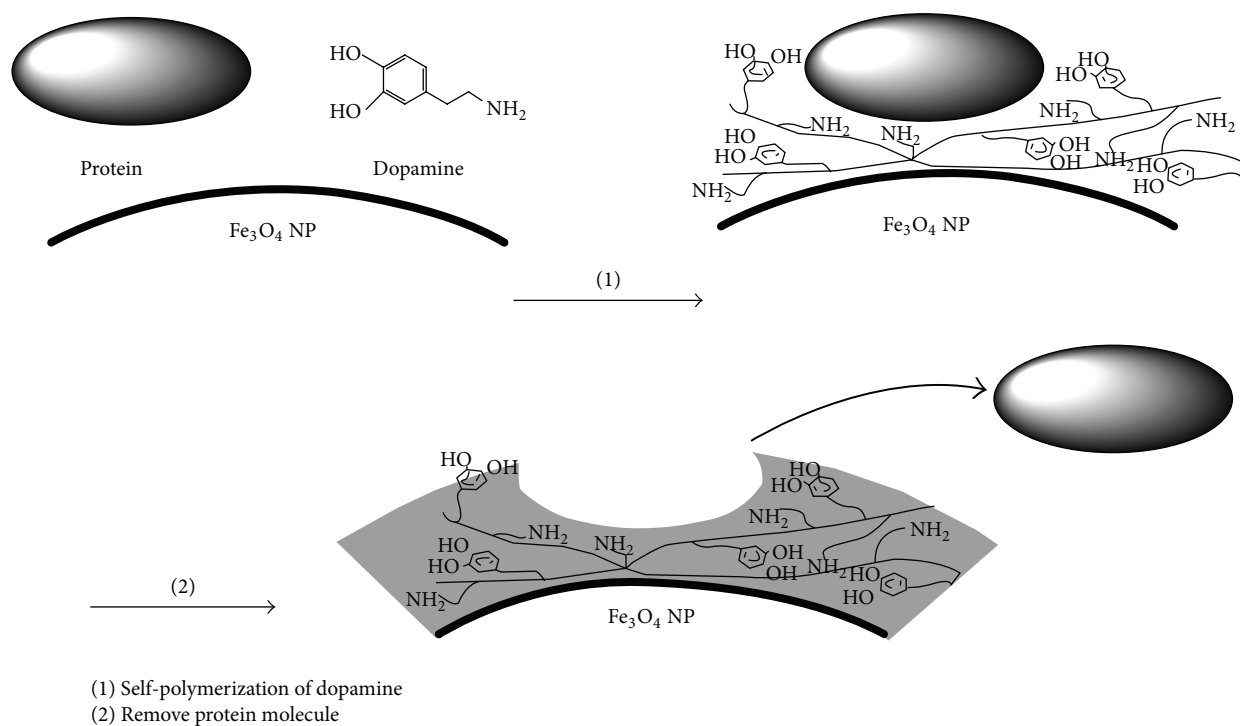


FIGURE 3: Formation of template imprinting PDA layer on Fe_3O_4 nanoparticles surface [19].

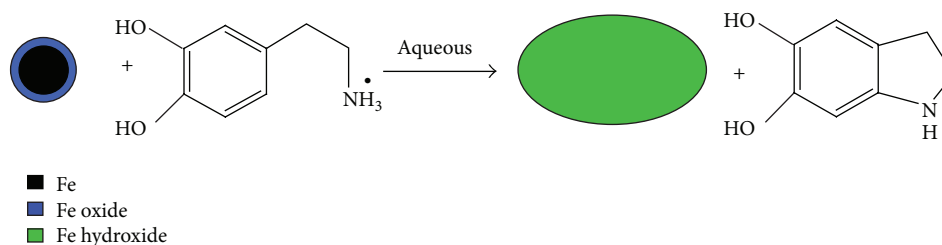


FIGURE 4: Illustration of reactive nature of dopamine as a surface functionalization agent in iron oxide nanoparticles [20].

enhanced magnetization and increased superparamagnetic blocking temperature, could be significantly improved via dopamine adsorption on iron oxide nanoparticles [46]. This was attributed to change from microstructure of the magnetic dead layer on the particle surface, which promoted magnetic ordering in the surface layer. A one-step reaction strategy was employed by Mazur et al. [23] to integrate several reactive sites onto iron oxide nanoparticles. Such particles, with size of 25 nm, were achieved by simultaneous modification with differently functionalized dopamine derivatives. Different termini, amine, azide, and maleimide functions enable further functionalization of iron oxide nanoparticles by the grafting-on approach (see Figure 7).

To enhance the functionality and thus to broaden the application of PDA coated iron oxide nanoparticles, many groups have done lots of effort. Kemikli et al. [47] obtained monosize sub-7 nm porphyrin coated magnetite nanoparticles via dopamine anchor with high crystallinity and well defined superparamagnetic behavior at room temperature. Zhou et al. [19] encapsued iron oxide nanoparticles with PDA

in the presence of human hemoglobin, yielding imprinted particles with preserved magnetic properties for their separation after exposure to targeting proteins. The versatility of the hemoglobin imprinted iron oxide nanoparticles was tested in a competitive binding assay using five different nontemplated proteins. In all assays, the relative binding of hemoglobin was over 80%, suggesting that those iron oxide nanoparticles have the potential to serve as affinity materials for protein separation and detection. With an ethanol-mediated oxidative polymerization of dopamine, Yue et al. [21] have achieved surface modified iron oxide nanoparticles. They found that the PDA coatings can dramatically reduce the cytotoxicity of nanomaterials and enhance their biocompatibility.

With the application environments (pH, temperature, ionic strength, illumination and time) in mind, the stability of PDA layer on iron oxide substrates is especially important for their application. A comparison of the stabilities of dopamine hydrochloride and 3,4-dihydroxybenzaldehyde for magnetic nanoparticles was carried out by Basti et al. [48] aiming at preparing novel MRI contrast agents.

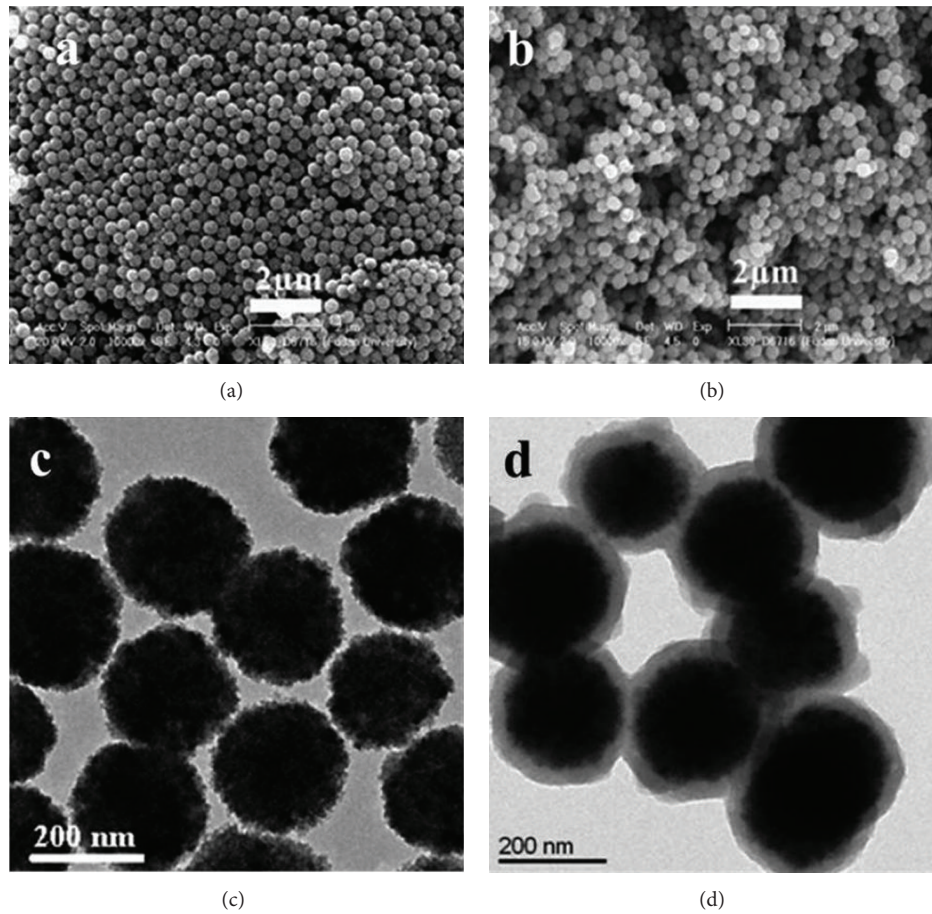


FIGURE 5: SEM (a and b) and TEM (c and d) images of (a and c) the Fe₃O₄ nanoparticles and (b and d) the Fe₃O₄@PDA core-shell particles [21].

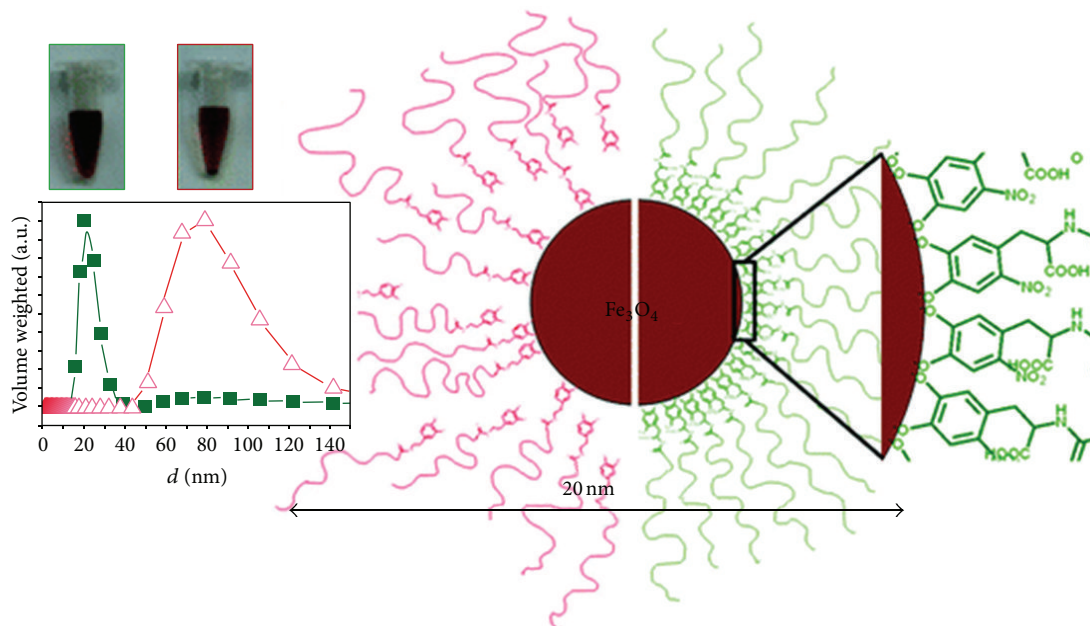


FIGURE 6: Dopamine-derivative anchor groups with irreversible binding affinity to iron oxide and optimal dispersity to superparamagnetic nanoparticles under physiologic conditions [22].

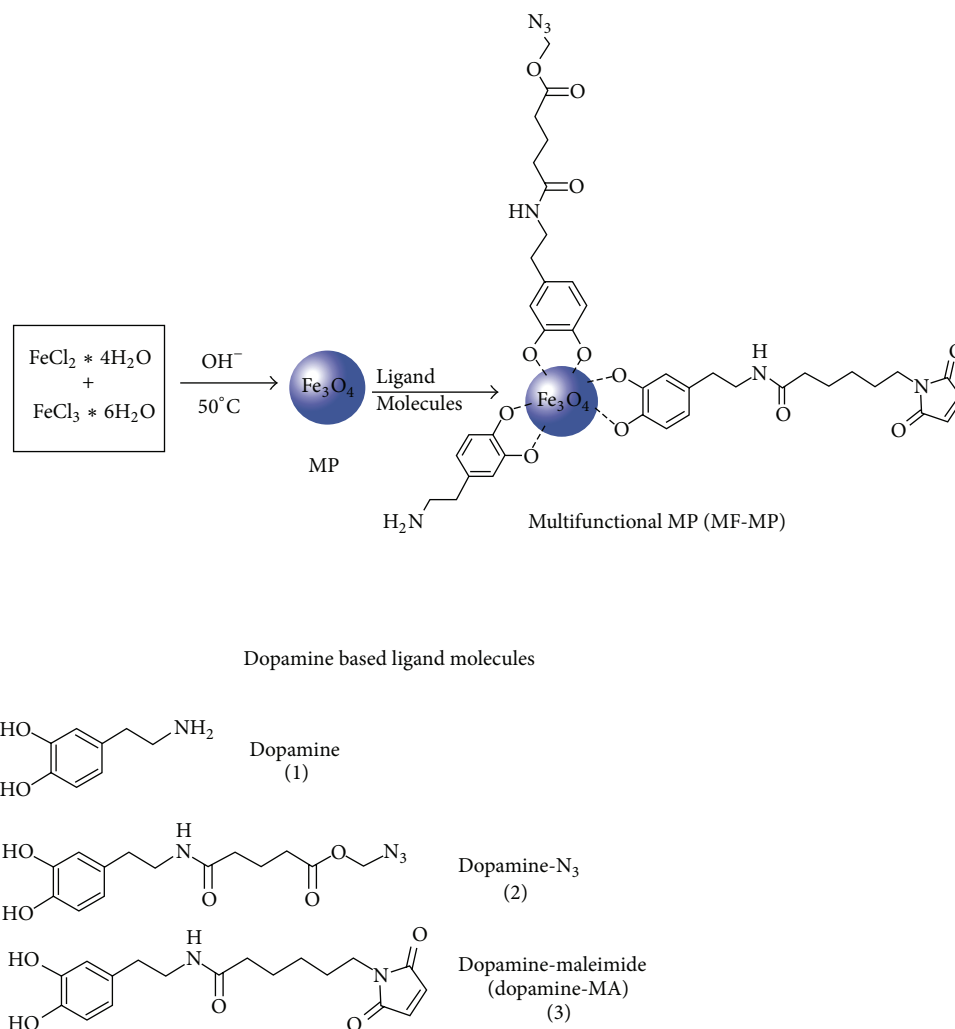


FIGURE 7: Schematic illustration of the formation of iron oxide nanoparticles with several reactive sites based on the use of differently functionalized dopamine derivatives [23].

Although both ligands coordinated the particle surface, thermogravimetric and calorimetric analyses indicated that 3,4-dihydroxybenzaldehyde did not have as high a grafting density as dopamine for magnetic nanoparticles. Hence, only dopamine was found to be suitable for stabilisation in aqueous environments, owing to its dense surface coverage. The formation of PDA layers on surfaces in aqueous solution probably indicates its good stability in aqueous environment. Dopamine is susceptible to oxidation itself, whereas PDA is more stable. The mPEG-dopamine-coated magnetite nanoparticles were stable at 70°C in the buffers when pH values are greater than 7 [49]. Moreover, dopamine-based anchor on iron oxide surfaces exhibited exceptional stability to heating and high salt concentration [50], with its thermal stability satisfying the requirement of hyperthermia therapy [14]. Amstad et al. reported dopamine derivative anchor groups having irreversible binding affinity to magnetite nanoparticles under physiological conditions [22]. Iron oxide nanoparticles modified with PEG-dopamine could be freeze-dried and stored as a powder for at least three months

or alternatively redispersed in pure water and stored for at least four months without noticeable change in particle stability. Particularly, the suspensions of PEG-nitrodopamine modified iron oxide nanoparticles can experience multiple cycles of diluting and heating free of nanoparticle agglomeration. Recently, highly crystalline and hydrophobic magnetite nanoparticles have been modified at the surface in the presence of dopamine with the advantages that the stability provided by a polypeptide shell covalently bonded to the magnetite surface through a dopamine anchor molecule instead of other noncovalent interactions [51].

For some potential applications, the PDA layer on magnetite nanoparticles must prove their robustness in variable environments, but relevant data are, so far, very rare. For example [16], the stability of PDA shell *in vivo* should be seriously taken into account. It is known that PDA will degrade oxidatively with the existence of strong alkaline or hydrogen peroxide [52]. For the *in vivo* case, Bettinger et al. [43] showed that the implant dopamine thin films seemed to degrade in tissue within eight weeks, where the gross

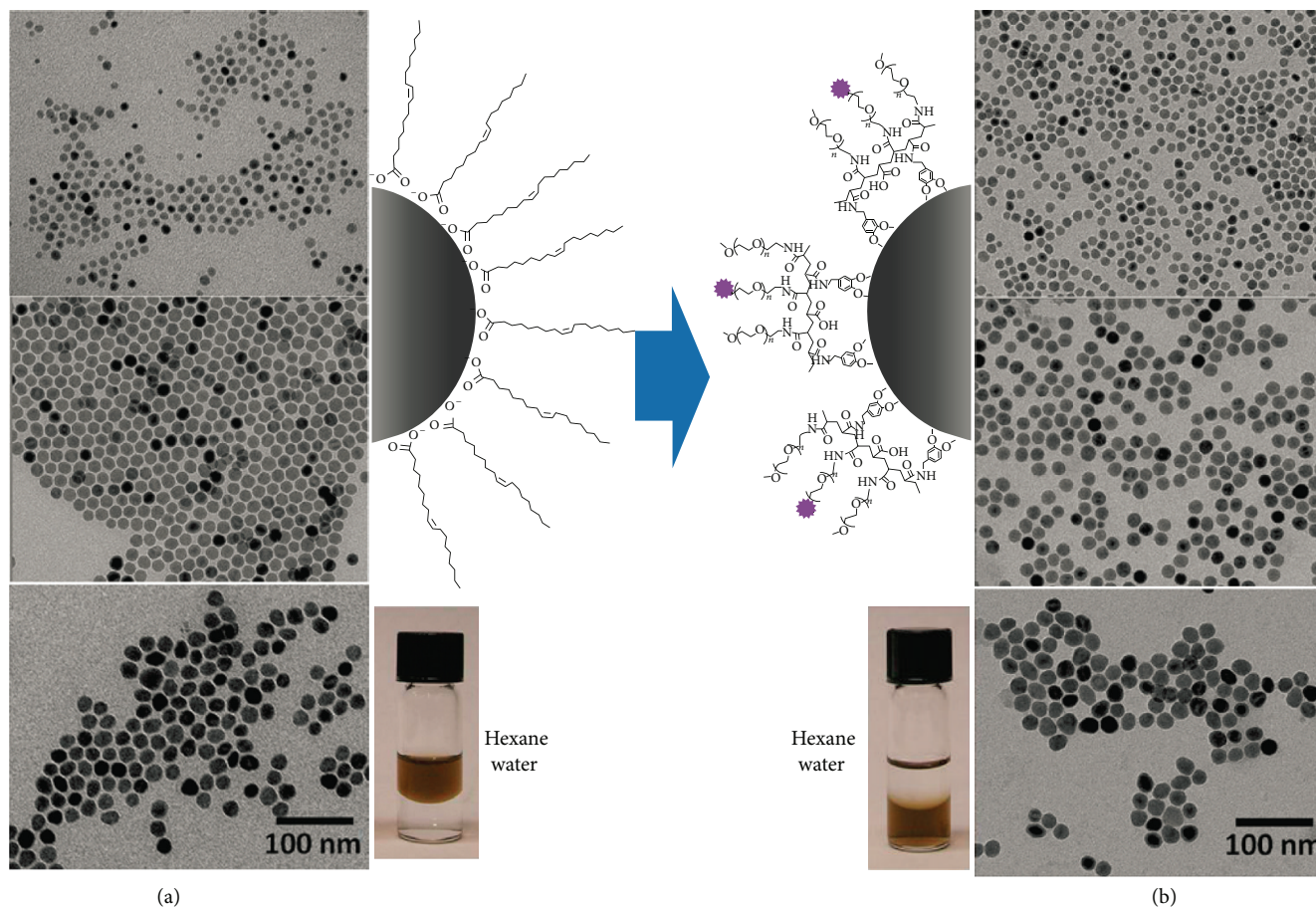


FIGURE 8: TEM images of Fe_3O_4 NPs with 11, 17, and 23 nm core size before (a) and after (b) ligand exchange with OligoPEG-Dopa. Schematic representation of the NP with the corresponding surface cap along with images of the organic and aqueous dispersions are shown [24].

erosion of the dopamine implant was fully completed. It could be attributed to the rigid properties of dopamine implants, which resulted in fracture of the implant after insertion into the host. The existence of dopamine nanoparticles could have allowed immediate uptake by macrophages and giant cells. However, it is still unanswered whether PDA, especially at the nanoscale, is degradable *in vivo* as well as within cells [53].

5. Safety Assessment on Polydopamine Coated Iron Oxide Nanoparticles

As mentioned above, PDA coating served as a useful method of surface functionalization on iron oxide nanoparticles due to the ability of this compound to form a nanometer-scale organic thin film on virtually any material surface to which many molecules are able to be attached. But a fact should not be neglected that dopamine is potentially individually highly neurotoxic molecule [54]. Thus evaluation of toxicity of PDA coated iron oxide nanoparticles should be carried out before their application, but to date less reference was found closely related to these aspects except the reports from Na et al. [24], Postma et al. [55], Xie et al. [15, 56], and Wei et al. [57].

Na et al. prepared a set of PDA and polyethylene glycol- (PEG-) derivatized oligomers, OligoPEG-Dopa on iron oxide nanocrystals (see Figure 8), which served as MRI T2 contrast, and applied MTT (3-(4,5-dimethylthiazol-2-yl)-2,5-diphenyltetrazolium bromide) assay to test the potential cytotoxicity of these NPs to live cells. Finally, they found no measurable toxicity to live cells [24]. Postma et al. carried out the cell experiment with PDA/ Fe_3O_4 capsules via a cell viability assay, showing that the $1\ \mu\text{m}$ capsules at the tested concentrations are not inherently cytotoxic for LIM1215 cells [55]. The work of Xie et al. demonstrated that the uniform PEG- Fe_3O_4 nanoparticles with catechol bonding brought about negligible aggregation in cell culture condition and much reduced nonspecific uptake by macrophage cells, meaning that these particles can escape from the innate immune system [15]. In addition, Xie et al. utilized dopamine modified iron oxide nanoparticles to yield nanoconjugates that could be easily encapsulated into human serum albumin (HSA) matrices. In order to assess their biophysical characteristics, the HSA coated iron oxide nanoparticles were labeled with both ^{64}Cu -DOTA and Cy5.5 and tested in a mouse model via subcutaneous U87MG xenograft. The particles were manifested a prolonged circulation half-life

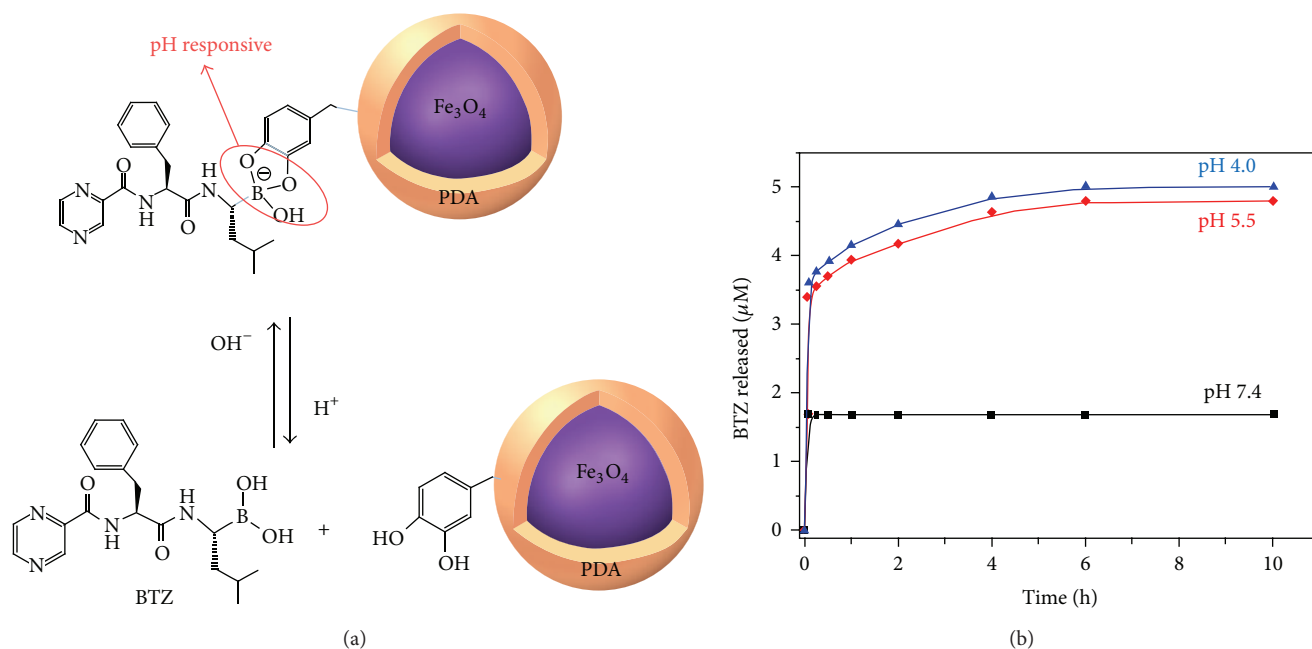


FIGURE 9: (a) Schematic of pH-dependent boronic acid–catechol conjugates on hybrid core–shell nanoparticle. (b) Time-dependent release of BTZ from $\text{Fe}_3\text{O}_4@$ PDA core–shell nanoparticles as a function of solution pH ranging from 4 to 7.4 [25].

and showed massive accumulation in lesions, high extravasation rate, and low uptake by macrophages at the tumor area [56]. Compact and water-soluble zwitterionic dopamine sulfonate (ZDS) ligand coated superparamagnetic iron oxide nanoparticles were prepared by Wei et al. [57] and their in vitro performance and in vivo performance relative to nonspecific interactions with HeLa cells and in mice were both evaluated. They found that those particles showed only small nonspecific uptake into HeLa cancer cells in vitro and low nonspecific binding to serum proteins in vivo in mice.

6. Biological Applications

The synthesis of dopamine functional magnetic nanoparticles is one of the most active areas in advanced materials as their surfaces allow conjugation of biological and chemical molecules, thus making it possible to achieve target-specific diagnostic in parallel to therapeutics [23]. Surface modification of diatom frustules with dopamine terminated iron oxide nanoparticles was confirmed active and available for the attachment of targeting ligands by Losic et al. [58]. Sustained release over 2 weeks of poorly water-soluble drug indomethacin from magnetic diatom structures has been demonstrated and is expected to serve as magnetically guided microcarriers with the potential to open new prospects for noninvasive and targeted drug delivery.

Polymer capsules are considered to be another desirable mean as drug delivery vehicles. Emulsion droplets, loaded with magnetic nanoparticles prior to the PDA deposition, yield about $1\mu\text{m}$ sized cargo-loaded PDA capsules [59]. A pH-sensitive manner was also used on $\text{Fe}_3\text{O}_4@$ PDA NPs for the controlled drug release via reversible bonding between

catechol and boronic acid groups of PDA and the anticancer drug bortezomib (BTZ) [25] (See Figure 9). The released amount of BTZ was pH dependent, with a greater concentration observed at lower pH values.

As universal nonfouling materials, PEGs were linked to surfaces using dopamine [13] and showed excellent resistance to serum protein adsorption [60]. A dopamine-PEG based ligand was used to stabilize uniform 9 nm magnetic nanoparticles in physiological conditions and against nonspecific uptake by macrophage cells. Such advantages provide an opportunity for enhancing the efficiency in target-specific drug delivery and increasing the signal-to-noise ratio in MRI [15].

Peng et al. [61] have linked dopamine as spacer molecules to iron oxide nanoparticles. They found that the existence of the spacer molecule on magnetic nanoparticles could greatly improve the activity and the storage stability of bound trypsin through increasing the flexibility of enzyme and changing the microenvironment on nanoparticles surface compared to the naked magnetic nanoparticles. Yuen et al. [12] prepared core-shell magnetic molecularly imprinted polymers for protein recognition. The lysozyme-imprinted $\text{Fe}_3\text{O}_4@$ PDA nanoparticles show high binding capacity and acceptable specific recognition behavior towards template proteins.

In addition, magnetic nanoparticles have been largely used for efficient magnetic resonance imaging. Xie et al. [62] reported an approach to prepare dopamine-plus-HSA (human serum albumin) to functionalize iron oxide nanoparticles, resulting in nanoconjugates with high efficiency in labeling various types of cell lines, and the application in vivo MRI on xenograft and focal cerebral ischemia models was further demonstrated. Lin et al. [39] prepared $\text{Fe}_3\text{O}_4@$ PDA

NCs with the ability to act as theranostic agents for intracellular mRNA detection and multimodal imaging-guided photothermal therapy. Generally speaking, the staining of the target cells by nonfouling nanoparticles is the prerequisite for this technique. The application usually requires designated molecules to be anchored onto the surfaces of magnetic nanoparticles. However, there are not very effective methods to modify Fe_3O_4 , to which solution dopamine provides great opportunity by displaying very good affinity to Fe_3O_4 . For example, Xie et al. reported peptide coated iron oxide nanoparticles via dopamine that act as a contrast agent used in MRI in vivo tumor detection. Moreover, the cellular uptake was dramatically increased due to multivalent binding of the functionalized iron oxide nanoparticles [33].

Immobilization of lipase on appropriate solid supports has been considered as an effective way to improve their stability and activity and could be reused for large scale applications. Ren et al. developed a lipase immobilization method by use of PDA coated iron oxide nanoparticles. 73.9% of the available lipase was immobilized on PDA coated iron oxide nanoparticles under optimal conditions, yielding a lipase loading capacity as high as 429 mg/g with enhanced pH and thermal stability compared to free lipase and the ease of isolation from the reaction medium by magnetic separation. This work made the immobilization of enzyme onto magnetic iron oxide nanoparticles via polydopamine film more economical, facile, and efficient [63].

Taking the advantages of PDA coatings into account, the applications will expand in the near future. Although biomedical application by such reports show promise, their potential needs to be further determined [64].

7. Conclusions and Perspectives

Dopamine and its derivatives can efficiently and facily modify iron oxide nanoparticles and yield functional surfaces. The surface modification relies largely on the interactions between nanoparticles substrate and PDA or their derivatives. Modified iron oxide surfaces exhibited the best stability due to the stronger adhesion [65, 66]. Although the details of the thermodynamics, kinetics, and mechanisms of dopamine self-oxidation keep unclear to date, the strong binding of dopamine represents a robust and feasible approach for the surface modification of iron oxide nanoparticles [16]. A large number of functionalities of such nanoparticles have been developed via the optimization of polymerization, the selection of dopamine ligands, or even more deeply insight with the quick appearance of advanced instruments.

This strategy may be utilized in increasing areas, including but not limited to biomedical application because of potential long term stability in wet conditions and resistance to oxidation. Future research may be directed towards an even more universal dopamine in physiological environments or at other complex conditions. For better application in biomedical areas, in vivo and in vitro safety assessment of PDA coated iron oxide nanoparticles should be carried out completely. Thus more questions about the modification, the functionality, and the application of PDA coated iron

oxide nanoparticles, according to those environments or conditions, should be better answered with broad and deep interdisciplinary content.

Conflict of Interests

The authors declare that there is no conflict of interests regarding the publication of this paper.

Acknowledgments

The authors are grateful to the National Natural Science Foundation of China (no. 51273033), Shandong Provincial Development Project of Science and Technology (no. 2014GGX102037), Shandong Province Higher Educational Science and Technology Program (no. J14LC56), and the Natural Science Foundation of Shandong Province, China (nos. ZR2010EL014, ZR2012HQ027, BS2011CL001, and ZR2014HL039).

References

- [1] Y. Yuan, D. Rende, C. L. Altan, S. Bucak, R. Ozisik, and D. A. B. Tasciuc, "Effect of surface modification on magnetization of iron oxide nanoparticle colloids," *Langmuir*, vol. 28, no. 36, pp. 13051–13059, 2012.
- [2] M. Talelli, C. J. F. Rijcken, T. Lammers et al., "Superparamagnetic iron oxide nanoparticles encapsulated in biodegradable thermosensitive polymeric micelles: toward a targeted nanomedicine suitable for image-guided drug delivery," *Langmuir*, vol. 25, no. 4, pp. 2060–2067, 2009.
- [3] M. Mahmoudi, A. Simchi, M. Imani, and U. O. Hafeli, "Superparamagnetic iron oxide nanoparticles with rigid cross-linked polyethylene glycol fumarate coating for application in imaging and drug delivery," *The Journal of Physical Chemistry C*, vol. 113, no. 19, pp. 8124–8131, 2009.
- [4] J. S. Beveridge, J. R. Stephens, and M. E. Williams, "The use of magnetic nanoparticles in analytical chemistry," *Annual Review of Analytical Chemistry*, vol. 4, pp. 251–273, 2011.
- [5] J. E. Smith, K. E. Sapsford, W. Tan, and F. S. Ligler, "Optimization of antibody-conjugated magnetic nanoparticles for target preconcentration and immunoassays," *Analytical Biochemistry*, vol. 410, no. 1, pp. 124–132, 2011.
- [6] H. E. Daldrup-Link, D. Golovko, B. Ruffell et al., "MRI of tumor-associated macrophages with clinically applicable iron oxide nanoparticles," *Clinical Cancer Research*, vol. 17, no. 17, pp. 5695–5704, 2011.
- [7] K. Andreas, R. Georgieva, M. Ladwig et al., "Highly efficient magnetic stem cell labeling with citrate-coated superparamagnetic iron oxide nanoparticles for MRI tracking," *Biomaterials*, vol. 33, no. 18, pp. 4515–4525, 2012.
- [8] F. M. Kievit and M. Zhang, "Surface engineering of iron oxide nanoparticles for targeted cancer therapy," *Accounts of Chemical Research*, vol. 44, no. 10, pp. 853–862, 2011.
- [9] X. Liu, J. Cao, H. Li et al., "Mussel-inspired polydopamine: a biocompatible and ultrastable coating for nanoparticles in vivo," *ACS Nano*, vol. 7, no. 10, pp. 9384–9395, 2013.
- [10] M. Zhang, X. Zhang, X. He, L. Chen, and Y. Zhang, "A self-assembled polydopamine film on the surface of magnetic nanoparticles for specific capture of protein," *Nanoscale*, vol. 4, no. 10, pp. 3141–3147, 2012.

- [11] A. H. Latham and M. E. Williams, "Controlling transport and chemical functionality of magnetic nanoparticles," *Accounts of Chemical Research*, vol. 41, no. 3, pp. 411–420, 2008.
- [12] A. K. L. Yuen, G. A. Hutton, A. F. Masters, and T. Maschmeyer, "The interplay of catechol ligands with nanoparticulate iron oxides," *Dalton Transactions*, vol. 41, no. 9, pp. 2545–2559, 2012.
- [13] H. Lee, S. M. Dellatore, W. M. Miller, and P. B. Messersmith, "Mussel-inspired surface chemistry for multifunctional coatings," *Science*, vol. 318, no. 5849, pp. 426–430, 2007.
- [14] H. Gu, K. Xu, Z. Yang, C. K. Chang, and B. Xu, "Synthesis and cellular uptake of porphyrin decorated iron oxide nanoparticles—a potential candidate for bimodal anticancer therapy," *Chemical Communications*, no. 34, pp. 4270–4272, 2005.
- [15] J. Xie, C. Xu, N. Kohler, Y. Hou, and S. Sun, "Controlled PEGylation of monodisperse Fe₃O₄ nanoparticles for reduced non-specific uptake by macrophage cells," *Advanced Materials*, vol. 19, no. 20, pp. 3163–3166, 2007.
- [16] Q. Ye, F. Zhou, and W. Liu, "Bioinspired catecholic chemistry for surface modification," *Chemical Society Reviews*, vol. 40, no. 7, pp. 4244–4258, 2011.
- [17] S. Ge, X. Shi, K. Sun et al., "Facile hydrothermal synthesis of iron oxide nanoparticles with tunable magnetic properties," *Journal of Physical Chemistry C*, vol. 113, no. 31, pp. 13593–13599, 2009.
- [18] J. S. Basuki, A. Jacquemin, L. Esser, Y. Li, C. Boyer, and T. P. Davis, "A block copolymer-stabilized co-precipitation approach to magnetic iron oxide nanoparticles for potential use as MRI contrast agents," *Polymer Chemistry*, vol. 5, no. 7, pp. 2611–2620, 2014.
- [19] W.-H. Zhou, C.-H. Lu, X.-C. Guo, F.-R. Chen, H.-H. Yang, and X.-R. Wang, "Mussel-inspired molecularly imprinted polymer coating superparamagnetic nanoparticles for protein recognition," *Journal of Materials Chemistry*, vol. 20, no. 5, pp. 880–883, 2010.
- [20] M. D. Shultz, J. U. Reveles, S. N. Khanna, and E. E. Carpenter, "Reactive nature of dopamine as a surface functionalization agent in iron oxide nanoparticles," *Journal of the American Chemical Society*, vol. 129, no. 9, pp. 2482–2487, 2007.
- [21] Q. Yue, M. Wang, Z. Sun et al., "A versatile ethanol-mediated polymerization of dopamine for efficient surface modification and the construction of functional core-shell nanostructures," *Journal of Materials Chemistry B*, vol. 1, no. 44, pp. 6085–6093, 2013.
- [22] E. Amstad, T. Gillich, I. Bilecka, M. Textor, and E. Reimhult, "Ultrastable iron oxide nanoparticle colloidal suspensions using dispersants with catechol-derived anchor groups," *Nano Letters*, vol. 9, no. 12, pp. 4042–4048, 2009.
- [23] M. Mazur, A. Barras, V. Kuncser et al., "Iron oxide magnetic nanoparticles with versatile surface functions based on dopamine anchors," *Nanoscale*, vol. 5, no. 7, pp. 2692–2702, 2013.
- [24] H. B. Na, G. Palui, J. T. Rosenberg, X. Ji, S. C. Grant, and H. Mattoussi, "Multidentate catechol-based polyethylene glycol oligomers provide enhanced stability and biocompatibility to iron oxide nanoparticles," *ACS Nano*, vol. 6, no. 1, pp. 389–399, 2012.
- [25] R. Liu, Y. Guo, G. Odusote, F. Qu, and R. D. Priestley, "Core-shell Fe₃O₄ polydopamine nanoparticles serve multipurpose as drug carrier, catalyst support and carbon adsorbent," *ACS Applied Materials and Interfaces*, vol. 5, no. 18, pp. 9167–9171, 2013.
- [26] Y. B. Kholam, S. R. Dhage, H. S. Potdar et al., "Microwave hydrothermal preparation of submicron-sized spherical magnetite (Fe₃O₄) powders," *Materials Letters*, vol. 56, no. 4, pp. 571–577, 2002.
- [27] S.-W. Cao and Y.-J. Zhu, "Iron oxide hollow spheres: microwave-hydrothermal ionic liquid preparation, formation mechanism, crystal phase and morphology control and properties," *Acta Materialia*, vol. 57, no. 7, pp. 2154–2165, 2009.
- [28] H. C. Roth, S. P. Schwaminger, M. Schindler, F. E. Wagner, and S. Berensmeier, "Influencing factors in the CO-precipitation process of superparamagnetic iron oxide nano particles: a model based study," *Journal of Magnetism and Magnetic Materials*, vol. 377, pp. 81–89, 2015.
- [29] T. Xia, J. Wang, C. Wu et al., "Novel complex-coprecipitation route to form high quality triethanolamine-coated Fe₃O₄ nanocrystals: their high saturation magnetizations and excellent water treatment properties," *CrystEngComm*, vol. 14, no. 18, pp. 5741–5744, 2012.
- [30] S. Sun and H. Zeng, "Size-controlled synthesis of magnetite nanoparticles," *Journal of the American Chemical Society*, vol. 124, no. 28, pp. 8204–8205, 2002.
- [31] P. Kucheryavy, J. He, V. T. John et al., "Superparamagnetic iron oxide nanoparticles with variable size and an iron oxidation state as prospective imaging agents," *Langmuir*, vol. 29, no. 2, pp. 710–716, 2013.
- [32] J. Park, K. An, Y. Hwang et al., "Ultra-large-scale syntheses of monodisperse nanocrystals," *Nature Materials*, vol. 3, no. 12, pp. 891–895, 2004.
- [33] J. Xie, K. Chen, H.-Y. Lee et al., "Ultrasmall c(RGDyK)-coated Fe₃O₄ nanoparticles and their specific targeting to integrin $\alpha_v\beta_3$ -rich tumor cells," *Journal of the American Chemical Society*, vol. 130, no. 24, pp. 7542–7543, 2008.
- [34] H. Lee, B. P. Lee, and P. B. Messersmith, "A reversible wet/dry adhesive inspired by mussels and geckos," *Nature*, vol. 448, no. 7151, pp. 338–341, 2007.
- [35] B. P. Lee, C. Y. Chao, F. Nelson Nunalee, E. Motan, K. R. Shull, and P. B. Messersmith, "Rapid gel formation and adhesion in photocurable and biodegradable block copolymers with high DOPA content," *Macromolecules*, vol. 39, no. 5, pp. 1740–1748, 2006.
- [36] J. Yan, L. Yang, M. F. Lin, J. Ma, X. Lu, and P. S. Lee, "Polydopamine spheres as active templates for convenient synthesis of various nanostructures," *Small*, vol. 9, no. 4, pp. 596–603, 2013.
- [37] S. H. Ku, J. S. Lee, and C. B. Park, "Spatial control of cell adhesion and patterning through mussel-inspired surface modification by polydopamine," *Langmuir*, vol. 26, no. 19, pp. 15104–15108, 2010.
- [38] H. Hu, B. Yu, Q. Ye, Y. Gu, and F. Zhou, "Modification of carbon nanotubes with a nanothin polydopamine layer and polydimethylamino-ethyl methacrylate brushes," *Carbon*, vol. 48, no. 8, pp. 2347–2353, 2010.
- [39] L.-S. Lin, Z.-X. Cong, J.-B. Cao et al., "Multifunctional Fe₃O₄@polydopamine core-shell nanocomposites for intracellular mRNA detection and imaging-guided photothermal therapy," *ACS Nano*, vol. 8, no. 4, pp. 3876–3883, 2014.
- [40] B. Yu, J. Liu, S. Liu, and F. Zhou, "Pdop layer exhibiting zwitterionicity: a simple electrochemical interface for governing ion permeability," *Chemical Communications*, vol. 46, no. 32, pp. 5900–5902, 2010.

- [41] K.-Y. Ju, Y. Lee, S. Lee, S. B. Park, and J.-K. Lee, "Bioinspired polymerization of dopamine to generate melanin-like nanoparticles having an excellent free-radical-scavenging property," *Biomacromolecules*, vol. 12, no. 3, pp. 625–632, 2011.
- [42] K. C. L. Black, J. Yi, J. G. Rivera, D. C. Zelasko-Leon, and P. B. Messersmith, "Polydopamine-enabled surface functionalization of gold nanorods for cancer cell-targeted imaging and photothermal therapy," *Nanomedicine*, vol. 8, no. 1, pp. 17–28, 2013.
- [43] C. J. Bettinger, J. P. Bruggeman, A. Misra, J. T. Borenstein, and R. Langer, "Biocompatibility of biodegradable semiconducting melanin films for nerve tissue engineering," *Biomaterials*, vol. 30, no. 17, pp. 3050–3057, 2009.
- [44] P. Yan, J. Wang, L. Wang, B. Liu, Z. Lei, and S. Yang, "The in vitro biomineralization and cytocompatibility of polydopamine coated carbon nanotubes," *Applied Surface Science*, vol. 257, no. 11, pp. 4849–4855, 2011.
- [45] J. Si and H. Yang, "Preparation and characterization of bio-compatible Fe_3O_4 @Polydopamine spheres with core/shell nanostructure," *Materials Chemistry and Physics*, vol. 128, no. 3, pp. 519–524, 2011.
- [46] M. S. Ata, Y. Liu, and I. Zhitomirsky, "A review of new methods of surface chemical modification, dispersion and electrophoretic deposition of metal oxide particles," *RSC Advances*, vol. 4, no. 43, pp. 22716–22732, 2014.
- [47] N. Kemikli, H. Kavaz, S. Kazan, A. Baykal, and R. Ozturk, "Synthesis of protoporphyrin coated superparamagnetic iron oxide nanoparticles via dopamine anchor," *Journal of Alloys and Compounds*, vol. 502, no. 2, pp. 439–444, 2010.
- [48] H. Basti, L. B. Tahar, L. S. Smiri et al., "Catechol derivatives-coated Fe_3O_4 and $\gamma\text{-Fe}_2\text{O}_3$ nanoparticles as potential MRI contrast agents," *Journal of Colloid and Interface Science*, vol. 341, no. 2, pp. 248–254, 2010.
- [49] J. Xie, C. Xu, Z. Xu et al., "Linking hydrophilic macromolecules to monodisperse magnetite (Fe_3O_4) nanoparticles via trichloro-s-triazine," *Chemistry of Materials*, vol. 18, no. 23, pp. 5401–5403, 2006.
- [50] C. Xu, K. Xu, H. Gu et al., "Dopamine as a robust anchor to immobilize functional molecules on the iron oxide shell of magnetic nanoparticles," *Journal of the American Chemical Society*, vol. 126, no. 32, pp. 9938–9939, 2004.
- [51] G. Marcelo, A. Muñoz-Bonilla, J. Rodríguez-Hernández, and M. Fernández-García, "Hybrid materials achieved by polypeptide grafted magnetite nanoparticles through a dopamine biomimetic surface anchored initiator," *Polymer Chemistry*, vol. 4, no. 3, pp. 558–567, 2013.
- [52] N. F. Della Vecchia, R. Avolio, M. Alfè, M. E. Errico, A. Napolitano, and M. D'Ischia, "Building-block diversity in polydopamine underpins a multifunctional eumelanin-type platform tunable through a quinone control point," *Advanced Functional Materials*, vol. 23, no. 10, pp. 1331–1340, 2013.
- [53] W.-B. Tsai, W.-T. Chen, H.-W. Chien, W.-H. Kuo, and M.-J. Wang, "Poly(dopamine) coating of scaffolds for articular cartilage tissue engineering," *Acta Biomaterialia*, vol. 7, no. 12, pp. 4187–4194, 2011.
- [54] M. Asanuma, I. Miyazaki, and N. Ogawa, "Dopamine- or L-DOPA-induced neurotoxicity: the role of dopamine quinone formation and tyrosinase in a model of Parkinson's disease," *Neurotoxicity Research*, vol. 5, no. 3, pp. 165–176, 2003.
- [55] A. Postma, Y. Yan, Y. Wang, A. N. Zelikin, E. Tjijto, and F. Caruso, "Self-polymerization of dopamine as a versatile and robust technique to prepare polymer capsules," *Chemistry of Materials*, vol. 21, no. 14, pp. 3042–3044, 2009.
- [56] J. Xie, K. Chen, J. Huang et al., "PET/NIRF/MRI triple functional iron oxide nanoparticles," *Biomaterials*, vol. 31, no. 11, pp. 3016–3022, 2010.
- [57] H. Wei, O. T. Bruns, O. Chen, and M. G. Bawendi, "Compact zwitterion-coated iron oxide nanoparticles for in vitro and in vivo imaging," *Integrative Biology*, vol. 5, no. 1, pp. 108–114, 2013.
- [58] D. Losic, Y. Yu, M. S. Aw, S. Simovic, B. Thierry, and J. Addai-Mensah, "Surface functionalisation of diatoms with dopamine modified iron-oxide nanoparticles: toward magnetically guided drug microcarriers with biologically derived morphologies," *Chemical Communications*, vol. 46, no. 34, pp. 6323–6325, 2010.
- [59] J. W. Cui, Y. J. Wang, A. Postma, J. Hao, L. Hosta-Rigau, and F. Caruso, "Monodisperse polymer capsules: tailoring size, shell thickness, and hydrophobic cargo loading via emulsion templating," *Advanced Functional Materials*, vol. 20, no. 10, pp. 1625–1631, 2010.
- [60] J. L. Dalsin, L. Lin, S. Tosatti, J. Vörös, M. Textor, and P. B. Messersmith, "Protein resistance of titanium oxide surfaces modified by biologically inspired mMpeg-dopa," *Langmuir*, vol. 21, no. 2, pp. 640–646, 2005.
- [61] H. Peng, X. Zhang, K. Huang, and H. Xu, "Modification of Fe_3O_4 magnetic nanoparticles by L-dopa or dopamine as an enzyme support," *Journal Wuhan University of Technology, Materials Science Edition*, vol. 23, no. 4, pp. 480–485, 2008.
- [62] J. Xie, J. Wang, G. Niu et al., "Human serum albumin coated iron oxide nanoparticles for efficient cell labeling," *Chemical Communications*, vol. 46, no. 3, pp. 433–435, 2010.
- [63] Y. Ren, J. G. Rivera, L. He, H. Kulkarni, D. K. Lee, and P. B. Messersmith, "Facile, high efficiency immobilization of lipase enzyme on magnetic iron oxide nanoparticles via a biomimetic coating," *BMC Biotechnology*, vol. 11, article 63, 2011.
- [64] M. E. Lyngø, R. van der Westen, A. Postma, and B. Städler, "Polydopamine—a nature-inspired polymer coating for biomedical science," *Nanoscale*, vol. 3, no. 12, pp. 4916–4928, 2011.
- [65] H. Chung, P. Glass, J. M. Pothén, M. Sitti, and N. R. Washburn, "Enhanced adhesion of dopamine methacrylamide elastomers via viscoelasticity tuning," *Biomacromolecules*, vol. 12, no. 2, pp. 342–347, 2011.
- [66] J. L. Murphy, L. Vollenweider, F. Xu, and B. P. Lee, "Adhesive performance of biomimetic adhesive-coated biologic scaffolds," *Biomacromolecules*, vol. 11, no. 11, pp. 2976–2984, 2010.

Research Article

A Green and Facile Synthesis of Carbon-Incorporated Co_3O_4 Nanoparticles and Their Photocatalytic Activity for Hydrogen Evolution

Libo Gao,^{1,2} Jiangtao Diwu,³ Qiang Zhang,^{1,2} Hongyan Xu,³
Xiujian Chou,^{1,2} Jun Tang,^{1,2} and Chenyang Xue^{1,2}

¹Key Laboratory of Instrumentation Science and Dynamic Measurement of Ministry of Education, North University of China, Taiyuan, Shanxi 030051, China

²Science and Technology on Electronic Test & Measurement Laboratory, North University of China, Taiyuan, Shanxi 030051, China

³School of Materials Science and Engineering, North University of China, Taiyuan, Shanxi 030051, China

Correspondence should be addressed to Chenyang Xue; xuechenyang@foxmail.com

Received 15 June 2014; Revised 9 August 2014; Accepted 10 August 2014

Academic Editor: Shimou Chen

Copyright © 2015 Libo Gao et al. This is an open access article distributed under the Creative Commons Attribution License, which permits unrestricted use, distribution, and reproduction in any medium, provided the original work is properly cited.

Carbon-incorporated Co_3O_4 nanoparticles with an average diameter of 50 nm were prepared via a facile and environmentally friendly one-pot carbon-assisted method using degreasing cotton as a template as well as a reactant. The elemental analysis indicates the incorporation of carbon species into the Co_3O_4 nanoparticles and the XPS measurements demonstrate the presence of carbon species which comes from the incomplete combustion of the degreasing cotton. Interestingly, the resultant sample was able to split pure water into hydrogen under visible light irradiation without any cocatalyst, which is mainly due to the enhanced light absorption behavior confirmed by the UV-Vis absorption spectra. This facile method provided a potential strategy for applying narrow bandgap semiconductors in pure water splitting.

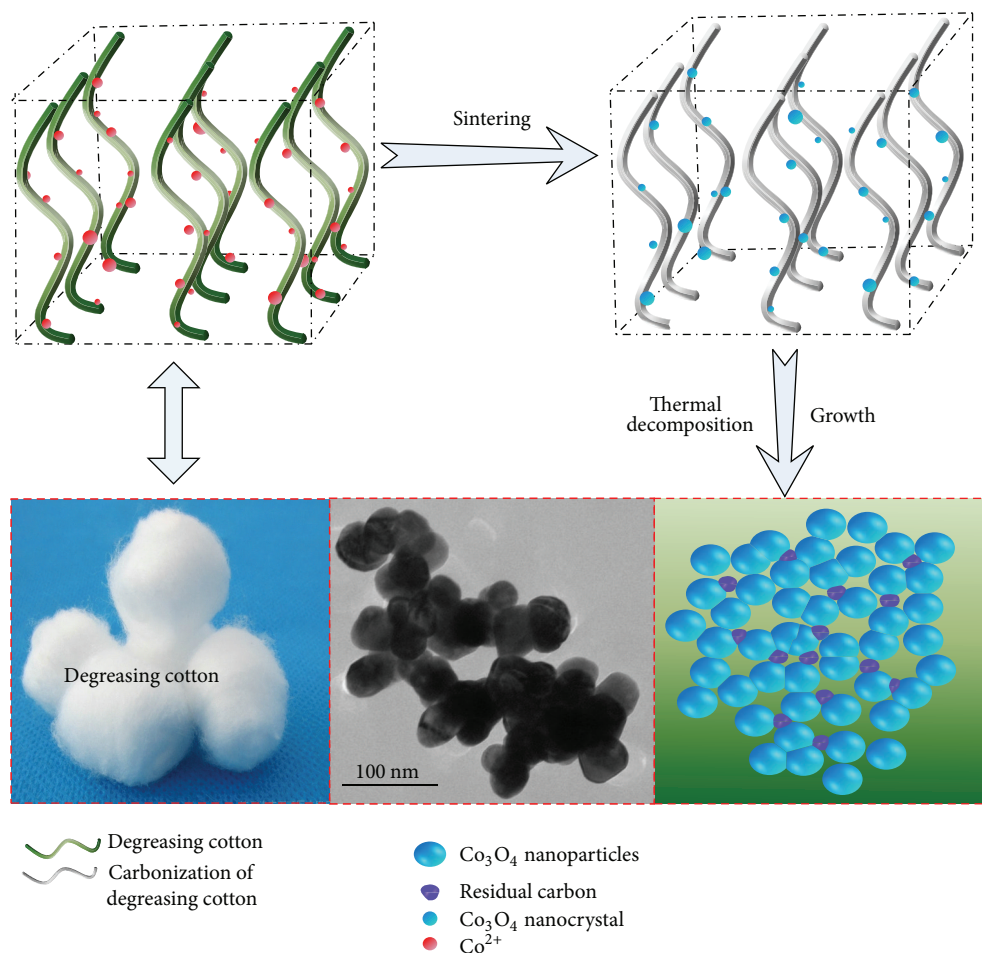
1. Introduction

In recent years, photocatalytic production of hydrogen from water splitting has been regarded as an ideal solution to deal with the energy problem, due to its clean, nonprecious, and environmentally friendly production process via utilizing solar energy [1, 2]. In this field, a large amount of semiconducting materials have been explored to choose the ideal material which is capable of splitting water into hydrogen efficiently.

Co_3O_4 with a bandgap of 2.1 eV has been widely explored for photocatalytic production of O_2 from water splitting, owing to its excellent oxidation ability and low energy gap [3]. However, due to the lower conduction band minimum (CBM) compared to the H^+ reduction potential, much less reports on photocatalytic production of hydrogen have been reported. Although Zhang et al. reported that the Co_3O_4 quantum dots prepared by a reverse micelle method using

a microwave-assisted solvothermal reaction had an excellent photocatalytic performance on splitting water into hydrogen because of the CBM upshift [4], this method required difficult procedures. Boumaza et al. reported that Co_3O_4 , a multifunctional spinel-type p-type, was capable of promoting hydrogen photoproduction in the presence of methanol as sacrificial agent. This material, however, suffered rapid deactivation [5]. Therefore much research should go deep into the Co_3O_4 as a photocatalyst for hydrogen production.

It has been reported recently that carbon species can serve as sensitizers [6, 7]. Zhang et al. reported that the carbon species incorporated TiO_2 had a high hydrogen production rate, which is 1.8 times larger than that of P25, owing to the sensitization effect of carbon [8]. Kado et al. also synthesized TiO_2 with an enhanced photoresponse, which was modified by a thin carbon [9]. Nevertheless, Co_3O_4 modified with the carbon species as a photocatalyst for water splitting into hydrogen has not been reported.



In this work, a facile and environmentally friendly one-pot carbon-assisted method using degreasing cotton as a template as well as a reactant was used to synthesize the carbon-incorporated Co_3O_4 and its hydrogen production from photocatalytic splitting of water has been studied. To the best of our knowledge, this is the first time that the carbon-incorporated Co_3O_4 prepared as a photocatalyst was used to split water into hydrogen and the sample prepared interestingly even has photocatalytic activity under visible light irradiation.

2. Materials and Methods

Synthesis. Typically, 17.46 g $\text{Co}(\text{NO}_3)_2 \cdot 6\text{H}_2\text{O}$ was added to 20 mL deionized water followed by vigorous stirring for 10 min, producing a stable pink solution. Subsequently, 1.5 g degreasing cotton was immersed into the obtained pink solution and kept in an ultrasonic bath for 10 min in order to have a good dispersion of Co^{2+} on the surface of degreasing cotton. Then the treated degreasing cotton was collected and transferred into a quartz petri dish in the tube furnace (OTF-1200X-III, Hefei, China) and kept at 600°C for 2 h in air.

The resultant sample designated as Co_3O_4 -DC was obtained without any postprocedures. For comparison, the product labeled as Co_3O_4 -WA was fabricated directly calcining $\text{Co}(\text{NO}_3)_2$ solution at 600°C for 2 h without any additive.

The formation procedure is shown as Scheme 1.

Characterization. The crystal structure of the sample was performed through X-ray diffraction (XRD, a Bruker D8, $\lambda = 1.5406 \text{ \AA}$) in the 2θ of $10\text{--}80^\circ$ with scan rate of $10^\circ/\text{min}$ and $\text{Cu K}\alpha$ radiation, 40 KV. Scanning electron microscopy (SEM) images were obtained on a Hitachi S-4800 scanning electron microscope. The particle shapes and sizes were characterized by TEM measurement (JEOL JEM-1200EX) with a working voltage being 120 kv. Chemical composition analysis was carried out using energy dispersive X-ray (EDX) spectroscopy and X-ray photoelectron spectroscopy (XPS) which was collected using an ESCALAB 250Xi spectrometer with a standard $\text{Al K}\alpha$ radiation with the binding energies calibrated based on the contaminant carbon ($\text{C1s} = 284.6 \text{ eV}$). The Raman spectrum was measured using a Renishaw inVia-Reflex Raman spectrometer. Specific surface areas and pore size distributions were computed from the results of N_2

physisorption at 77 K (Micromeritics ASAP 2020) by using the BET (Brunauer-Emmett-Teller) and BJH (Barrett-Joyner-Halenda). A Cary 300 Scan UV-Vis spectrophotometer was employed to record the UV-Vis diffuse reflectance spectra (DRS) in a region of 200 to 800 nm.

Photocatalysis. The photocatalytic activity for hydrogen production generated from water was estimated under simulated solar light condition. Typically, 0.02 g photocatalyst was added into the solution (~200 mL) containing 100 mL water and 100 mL ethanol as the sacrificial reagent, as it is more sustainable and renewable than methanol. The mixture was put in an ultrasonic stirring for 20 min, purged by Ar gas for 20 min, and then irradiated under simulated solar light with magnetic stirring. A 300 W Xe arc lamp (LSH-A500, Kaifeng Hxsei Science Instrument Co., Ltd., China) with UV cut-off filters (420 nm) was used as the light source. The hydrogen produced was analyzed by a gas chromatography (GC-9890B, Shanghai Linghua Instrument Co., Ltd., China) equipped with a thermal conductivity detector and a stainless steel column packed with molecular sieve (5A). Ar gas (99.999%) was used as the carrier gas.

3. Results and Discussions

3.1. Characterization. The XRD patterns of the Co_3O_4 -DC are shown in Figure 1. No impurity peaks are found in the XRD patterns and all peaks have a good agreement with the standard spinel cubic Co_3O_4 spectrum (JCPDS number 42-1467; space group $\text{Fd}\bar{3}\text{m}$; lattice constant $a = 8.084 \text{ \AA}$), suggesting that the sample produced is well-crystallized Co_3O_4 with high purity. The crystalline sizes of Co_3O_4 -DC and Co_3O_4 -WA (see the supporting information Figure S1 in the Supplementary Material available online at <http://dx.doi.org/10.1155/2015/618492>) calculated from the strongest peak located at (311) plan, respectively, are estimated to be 51.64 nm and ~100 nm according to Scherrer's formula, $D = 0.89\lambda / (B \cos \theta)$ (D , average dimension of crystallites; λ , the X-ray wavelength; θ , the Bragg angle; B , the pure diffraction broadening of a peak at half-height), thus confirming that the crystal size of Co_3O_4 -DC is much smaller than that of Co_3O_4 -WA.

To further observe the morphologies of Co_3O_4 -DC and Co_3O_4 -WA, SEM and TEM were performed. It is clear from the panoramic view (insets (a), (b), and (c) of Figure 1) that the Co_3O_4 -DC interestingly contains uniform and weak agglomerated Co_3O_4 nanospheres with 50 nm in diameter, which is in accordance with the value calculated from XRD. In addition, disordered hole-like arrangement of pores also can be seen in inset (a), making a promising favor to facilitate the water splitting due to the large specific surface area. The BET surface area and BJH pore size distributions of the as-prepared Co_3O_4 -DC are shown in Figure S2 and the BET surface area is calculated to be $17.46 \text{ m}^2 \text{ g}^{-1}$ and the average pore size is 23.67 nm while the Co_3O_4 -WA is only $5.8 \text{ m}^2 \text{ g}^{-1}$. Thus the Co_3O_4 -DC should have more active sites in principle, which is beneficial to the photocatalytic splitting water into hydrogen [10]. Nevertheless, the Co_3O_4 -WA

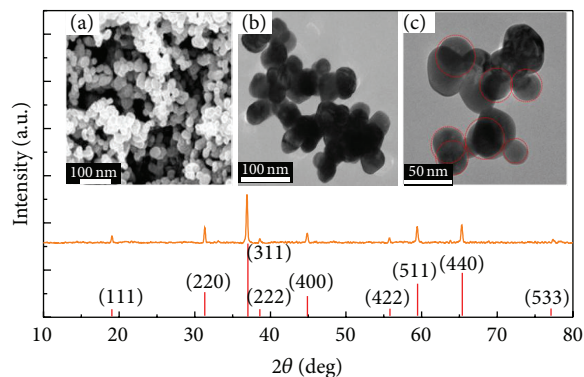


FIGURE 1: XRD patterns of Co_3O_4 -DC and the inset is (a) SEM image; ((b), (c)) TEM images of Co_3O_4 -DC. The inset bottom red bars indicate the standard reflections from Co_3O_4 (JCPDS number 42-1467).

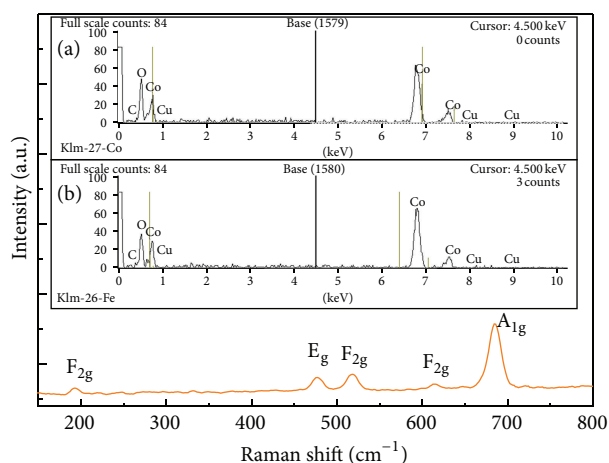


FIGURE 2: Raman spectrum of the Co_3O_4 -DC. The insets are element analysis on the surface (a) and the cross section (b) of the Co_3O_4 -DC.

nanoparticles despondingly have geometric irregular shapes which are spherical or rod-like structure with a particle size of ~100 nm, as shown in Figure S3.

Based on the analysis above, it is proved that the degreasing cotton used in the carbon-assisted method plays an important role in the fabrication of the Co_3O_4 -DC with both regular morphology and high crystallization.

In an attempt to clarify the structure of the Co_3O_4 -DC, Raman spectrum was performed due to its sensitivity on the microstructure of nanocrystalline materials. As shown in Figure 2, five obvious peaks are found at 192.4, 476.1, 518.3, 614.5, and 685.2 cm^{-1} , respectively, corresponding to the five Raman-active modes ($\text{A}_{1\text{g}}$, E_{g} , and $3\text{F}_{2\text{g}}$) of Co_3O_4 . The Raman shifts are consistent with those of pure crystalline Co_3O_4 [11], revealing that the sample has a similar crystal structure to bulk Co_3O_4 .

The insets of Figure 2 show the elemental analysis for the Co_3O_4 -DC. The carbon content in the nanoparticles is 31.5 at% (atomic percent) on the surface (the inset (a) of Figure 2) and 24.35 at% in the cross section (inset (b) of Figure 2),

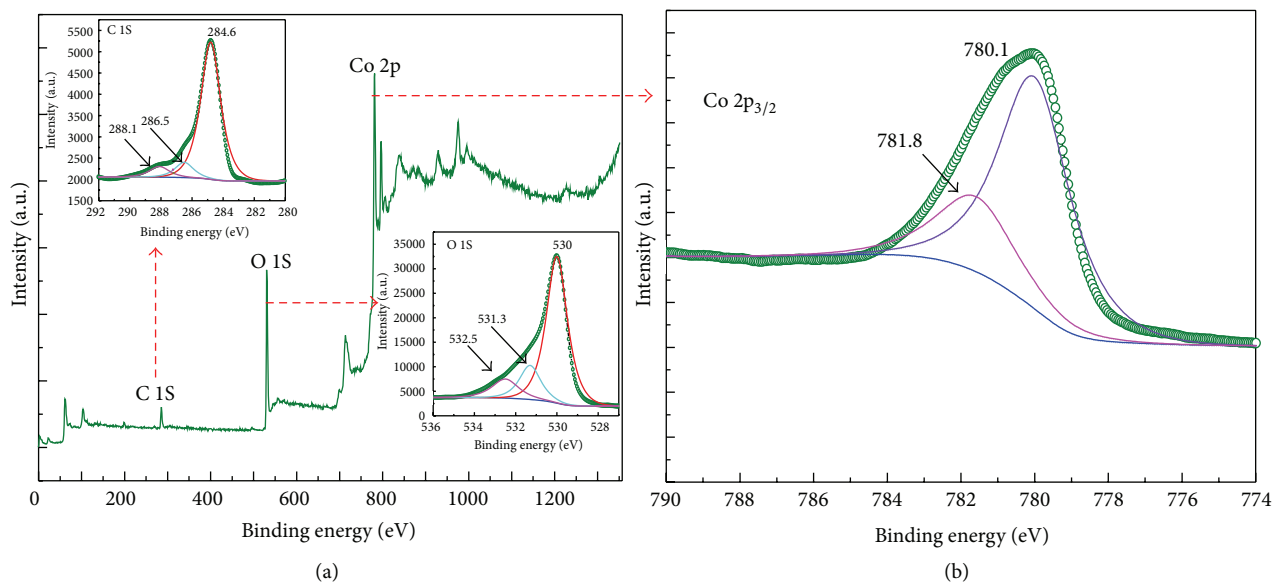


FIGURE 3: (a) XPS survey spectrum of the Co_3O_4 -DC. The inset of (a) is the high resolution XPS C 1s and O 1s. (b) The high resolution XPS Co $2p_{3/2}$.

respectively. These results indicate the incorporation of carbon species into the Co_3O_4 nanoparticles, as a result of incomplete decomposition of degreasing cotton.

Figure 3 presents the X-ray photoemission spectroscopy (XPS) of Co_3O_4 -DC to estimate the chemical composition of the sample. Peaks corresponding to cobalt, carbon, and oxygen are detected in the spectrum, indicating that only Co, O, and C elements can be found in the Co_3O_4 -DC. The strong peak of C 1s centers at 284.6 eV can be assigned to elemental carbon which has given rise to the incomplete burning of degreasing cotton [12]. The other two weak peaks showed at 286.5 and 288.1 eV, respectively, which, as expected, are ascribed to the C–O bonds from insufficient combustion residual degreasing cotton [13, 14]. Additionally, no Co–C bond at 282.5 eV has been clearly found [15], revealing that nearly no carbon is doped into the lattice of Co_3O_4 . As a consequence, it is proved that the carbon species incorporated in Co_3O_4 matrix are almost present as elemental state, which is in line with the results obtained in Teng's work [12].

The inset of Figure 3(a) shows the O 1s spectrum of the evaluated sample. The asymmetric O 1s spectra are fitted using two component peaks centered at 530 and 531.3 eV, which are ascribed to the surface lattice oxygen species and the surface adsorbed oxygen species (O^{2-} or O^-), respectively [16]. The peak at 532.5 eV can be assigned to C–O [8], which is caused by the incomplete decomposition of degreasing cotton. Figure 3(b) gives the Co $2p_{3/2}$ high resolution XPS spectrum of the as-synthesized Co_3O_4 -DC. The peaks at 780.1 and 781.8 eV correspond to Co^{3+} and Co^{2+} , respectively [17, 18]. The ratio of $\text{Co}^{3+}/\text{Co}^{2+}$ on the surface of Co_3O_4 -DC estimated by quantitative analysis is 2.84 instead of 2 in the chemical form of $\text{Co}^{2+}(\text{Co}^{3+})_2\text{O}_4$ while it is 1.89 in that of the Co_3O_4 -WA (Figure S4), and the probable reason is the presence of abundant surface oxygen vacancies on

the Co_3O_4 -WA with much less defects on Co_3O_4 -DC [16]. Importantly, it has been confirmed that less defects give rise to higher photocatalytic activity, as the recombination between photogenerated electrons and holes is decreased at the defect [19], thus indicating that our prepared sample may have a better performance on splitting water into hydrogen.

The optical absorption properties of the Co_3O_4 -DC were investigated at room temperature by UV-Vis spectroscopy (Figure 4(a)). It is obvious that more intense and broad background absorption in the visible light region is observed for Co_3O_4 -DC, and the absorption edges shift to longer wavelength compared with that of Co_3O_4 -WA. The carbon residuals on the Co_3O_4 -DC may be responsible for this phenomenon. In addition, the bandgap E_g value calculated according to the UV-Vis spectroscopy of Co_3O_4 -DC is 2.0 eV (Figure 4(b)) which was greater than that of Co_3O_4 -WA ($E_g = 1.9$ eV, inset of Figure 4(c)). The increase in the bandgap of the Co_3O_4 -DC may be ascribed to the quantum confinement effects of nanomaterials [20]. Importantly, inset of Figure 4(a) shows the valence band maximum of Co_3O_4 -DC and Co_3O_4 -WA, clearly indicating that they have almost the same position of valence-band XPS spectra, thus demonstrating that bandgap widening of Co_3O_4 -DC was mainly attributed to the conduction band minimum upshift, which would provide higher potential for H^+ reduction beneficial for photocatalytic hydrogen production.

Control experiments demonstrated that no hydrogen was evolved when the reaction proceeded without a photocatalyst or in the dark under stirring conditions while other conditions remained unchanged.

Figure 5(a) shows the photocatalytic hydrogen production on Co_3O_4 -DC and Co_3O_4 -WA at water/sacrificial agent (1:1) under simulated solar light. Higher photocatalytic splitting of water is observed for the Co_3O_4 -DC (0.85 μmol

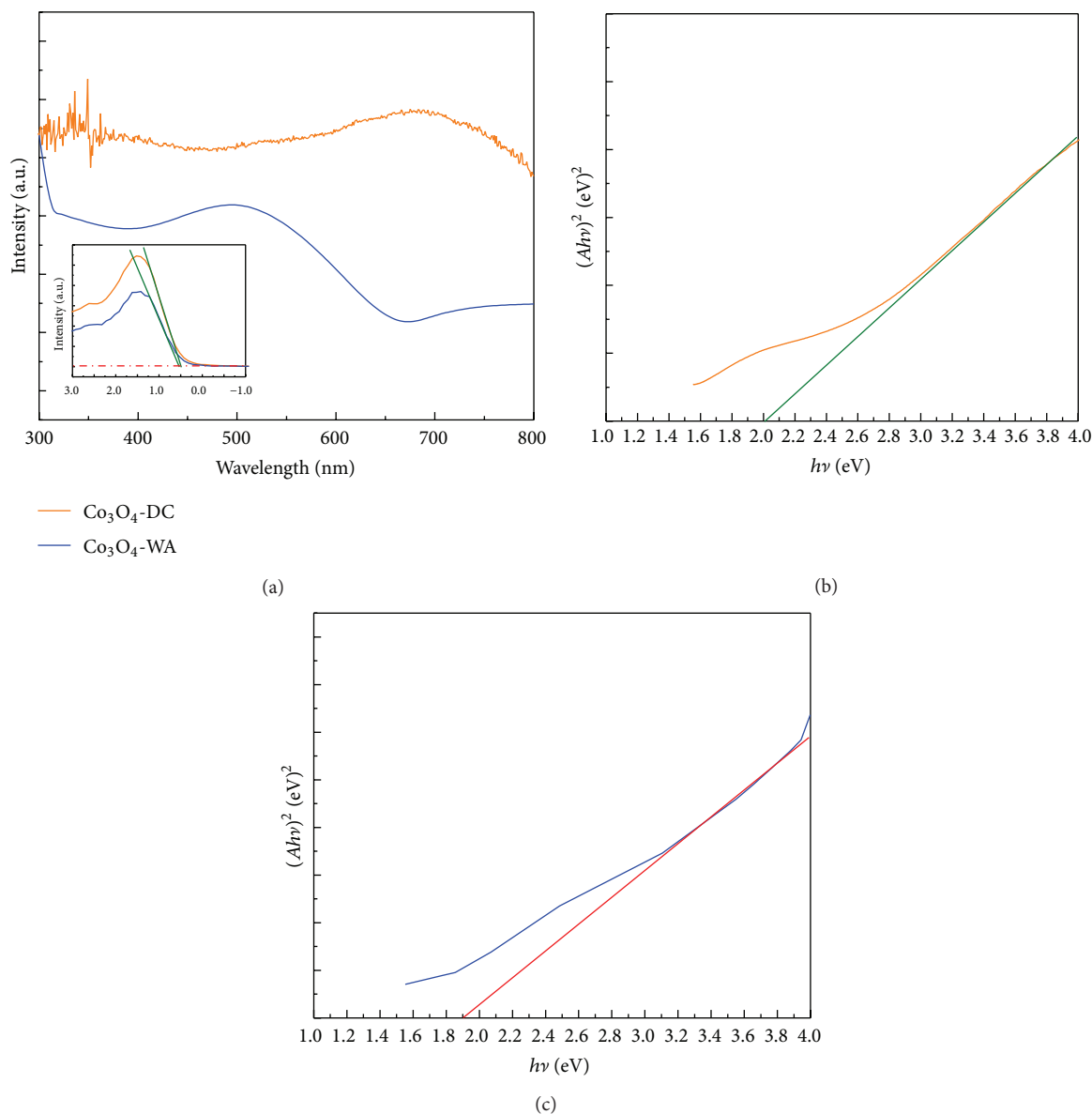


FIGURE 4: (a) UV-Vis spectrum of Co₃O₄-DC and Co₃O₄-WA, (b) $(Ah\nu)^2$ - $h\nu$ curve of Co₃O₄-DC, and (c) $(Ah\nu)^2$ - $h\nu$ curve of Co₃O₄-WA. Inset of (a): valence-band XPS spectra of Co₃O₄-DC and Co₃O₄-WA.

h^{-1}) as compared to that of Co₃O₄-WA (0.57 $\mu\text{mol h}^{-1}$). The improvement of activity of Co₃O₄-DC could be ascribed to the small particle size and a high surface area resulted from the disordered hole-like arrangement of pores produced by the decomposition of degreasing cotton as a hard template, an abundance of oxygen vacancies, and a much more intense and broad background absorption in the visible light region which were caused by the sensitization of carbon residuals. Figure 5(b) displays the photocatalytic hydrogen production on Co₃O₄-DC and Co₃O₄-WA at pure water under simulated solar light; the hydrogen product decreases to 0.13 $\mu\text{mol h}^{-1}$ for Co₃O₄-DC, indicating that the sacrificial agent has a significant effect on the photocatalytic hydrogen production. It is evidently seen that Co₃O₄-DC showed photocatalytic activity for hydrogen evolution while Co₃O₄-WA did not have

a photocatalytic performance in pure water under visible light (Figure 5(c)). Zhang et al. [8] and Lettmann et al. [21] have proved that the carbon residuals in semiconducting metal oxide are prone to carrying out a charge transfer process and are responsible for the photosensitization of semiconducting metal oxide. Thus, the enhanced photocatalytic activity of the sample can be ascribed to the sensitization effect of carbon and the conduction band minimum upshift. Proposed mechanism for photocatalytic hydrogen production for Co₃O₄-DC is shown in Figure 5(d). After an electron is excited from the carbon residual by light irradiation, the electron is injected to the conduction band of Co₃O₄; meanwhile, the electron excited in Co₃O₄ also takes part in the hydrogen production and then hydrogen evolves on the surface of Co₃O₄ [22]. These results confirm that the carbon-incorporated Co₃O₄

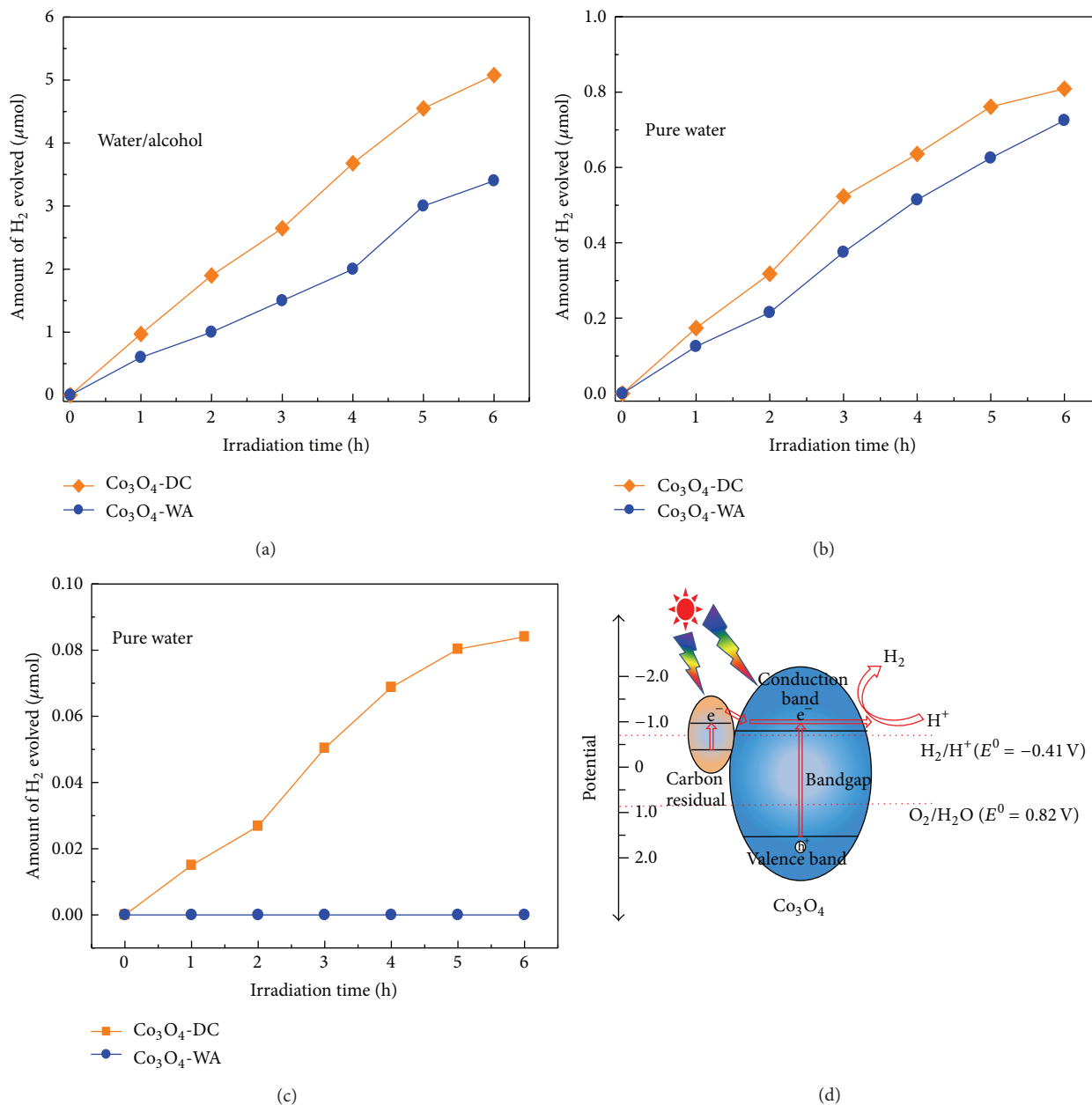


FIGURE 5: Photocatalytic hydrogen production on Co₃O₄-DC and Co₃O₄-WA under simulated solar light at (a) water/sacrificial agent (1:1); (b) pure water; (c) photocatalytic hydrogen production on Co₃O₄-DC and Co₃O₄-WA under visible light at pure water; (d) proposed mechanism for photocatalytic hydrogen production for Co₃O₄-DC at pure water.

synthesized via carbon-assisted method using degreasing cotton has a good performance in hydrogen production and even has photocatalytic ability under visible light for hydrogen evolution.

4. Conclusions

In summary, carbon-incorporated Co₃O₄ was successfully prepared by a facile and environmentally friendly carbon-assisted method using degreasing cotton and further applied as a photocatalyst in photocatalytic water splitting for hydrogen

evolution. The carbon-incorporated Co₃O₄ was able to split pure water into hydrogen under visible light condition without any cocatalyst, which is mainly due to the sensitization effect of carbon. In addition, it provided a potential strategy for applying narrow bandgap semiconductors in pure water splitting.

Conflict of Interests

The authors declare that there is no conflict of interests regarding the publication of this paper.

Acknowledgments

The authors gratefully acknowledge the support of this research by the National Natural Science Foundation of China (no. 91123616 and no. 51105345). They also deeply appreciate the referee's valuable comments, which have greatly enhanced the quality of the paper.

References

- [1] X. B. Chen, S. H. Shen, L. J. Guo, and S. S. Mao, "Semiconductor-based photocatalytic hydrogen generation," *Chemical Reviews*, vol. 110, no. 11, pp. 6503–6570, 2010.
- [2] R. Abe, "Recent progress on photocatalytic and photoelectrochemical water splitting under visible light irradiation," *Journal of Photochemistry and Photobiology C: Photochemistry Reviews*, vol. 11, no. 4, pp. 179–209, 2010.
- [3] S. Yusuf and F. Jiao, "Effect of the support on the photocatalytic water oxidation activity of cobalt oxide nanoclusters," *ACS Catalysis*, vol. 2, no. 12, pp. 2753–2760, 2012.
- [4] N. Zhang, J. Shi, S. S. Mao, and L. Guo, "Co₃O₄ quantum dots: reverse micelle synthesis and visible-light-driven photocatalytic overall water splitting," *Chemical Communications*, vol. 50, no. 16, pp. 2002–2004, 2014.
- [5] S. Boumaza, R. Bouarab, M. Trari, and A. Bouguelia, "Hydrogen photo-evolution over the spinel CuCr₂O₄," *Energy Conversion and Management*, vol. 50, no. 1, pp. 62–68, 2009.
- [6] C. Chen, M. Long, H. Zeng et al., "Preparation, characterization and visible-light activity of carbon modified TiO₂ with two kinds of carbonaceous species," *Journal of Molecular Catalysis A: Chemical*, vol. 314, no. 1-2, pp. 35–41, 2009.
- [7] J. Zhong, F. Chen, and J. Zhang, "Carbon-deposited TiO₂: synthesis, characterization, and visible photocatalytic performance," *Journal of Physical Chemistry C*, vol. 114, no. 2, pp. 933–939, 2010.
- [8] X. Zhang, Y. Sun, X. Cui, and Z. Jiang, "Carbon-incorporated TiO₂ microspheres: facile flame assisted hydrolysis of tetrabutyl orthotitanate and photocatalytic hydrogen production," *International Journal of Hydrogen Energy*, vol. 37, no. 2, pp. 1356–1365, 2012.
- [9] Y. Kado, R. Hahn, and P. Schmuki, "Surface modification of TiO₂ nanotubes by low temperature thermal treatment in C₂H₂ atmosphere," *Journal of Electroanalytical Chemistry*, vol. 662, no. 1, pp. 25–29, 2011.
- [10] P. Yang, D. Zhao, D. I. Margolese, B. F. Chmelka, and G. D. Stucky, "Block copolymer templating syntheses of mesoporous metal oxides with large ordering lengths and semicrystalline framework," *Chemistry of Materials*, vol. 11, no. 10, pp. 2813–2826, 1999.
- [11] V. G. Hadjiev, M. N. Iliev, and I. V. Vergilov, "The Raman spectra of Co₃O₄," *Journal of Physics C: Solid State Physics*, vol. 21, no. 7, pp. L199–L201, 1988.
- [12] Y. Teng, L. X. Song, L. B. Wang, and J. Xia, "Face-raised octahedral Co₃O₄ nanocrystals and their catalytic activity in the selective oxidation of alcohols," *Journal of Physical Chemistry C*, vol. 118, no. 9, pp. 4767–4773, 2014.
- [13] C.-S. Kuo, Y.-H. Tseng, C.-H. Huang, and Y.-Y. Li, "Carbon-containing nano-titania prepared by chemical vapor deposition and its visible-light-responsive photocatalytic activity," *Journal of Molecular Catalysis A: Chemical*, vol. 270, no. 1-2, pp. 93–100, 2007.
- [14] W. Ren, Z. Ai, F. Jia, L. Zhang, X. Fan, and Z. Zou, "Low temperature preparation and visible light photocatalytic activity of mesoporous carbon-doped crystalline TiO₂," *Applied Catalysis B: Environmental*, vol. 69, no. 3-4, pp. 138–144, 2007.
- [15] D. X. Ye, S. Pimanpang, C. Jezewski et al., "Low temperature chemical vapor deposition of Co thin films from Co₂(CO)₈," *Thin Solid Films*, vol. 485, no. 1-2, pp. 95–100, 2005.
- [16] G. Kwak, J. Hwang, J.-Y. Cheon et al., "Preparation method of Co₃O₄ nanoparticles using ordered mesoporous carbons as a template and their application for Fischer-Tropsch synthesis," *The Journal of Physical Chemistry C*, vol. 117, no. 4, pp. 1773–1779, 2013.
- [17] T. J. Chuang, C. R. Brundle, and D. W. Rice, "Interpretation of the x-ray photoemission spectra of cobalt oxides and cobalt oxide surfaces," *Surface Science*, vol. 59, no. 2, pp. 413–429, 1976.
- [18] J. L. Gautier, E. Rios, M. Gracia, J. F. Marco, and J. R. Gancedo, "Characterisation by X-ray photoelectron spectroscopy of thin Mn_xCo_{3-x}O₄ (1 ≥ x ≥ 0) spinel films prepared by low-temperature spray pyrolysis," *Thin Solid Films*, vol. 311, no. 1-2, pp. 51–57, 1997.
- [19] H. Kato and A. Kudo, "Highly efficient decomposition of pure water into H₂ and O₂ over NaTaO₃ photocatalysts," *Catalysis Letters*, vol. 58, no. 2-3, pp. 153–155, 1999.
- [20] S. Farhadi, K. Pourzare, and S. Sadeghinejad, "Simple preparation of ferromagnetic Co₃O₄ nanoparticles by thermal dissociation of the [CoII(NH₃)₆](NO₃)₂ complex at low temperature," *Journal of Nanostructure in Chemistry*, vol. 3, no. 1, pp. 1–7, 2013.
- [21] C. Lettmann, K. Hildenbrand, H. Kisch, W. Macyk, and W. F. Maier, "Visible light photodegradation of 4-chlorophenol with a coke-containing titanium dioxide photocatalyst," *Applied Catalysis B: Environmental*, vol. 32, no. 4, pp. 215–227, 2001.
- [22] A. Kudo and Y. Miseki, "Heterogeneous photocatalyst materials for water splitting," *Chemical Society Reviews*, vol. 38, no. 1, pp. 253–278, 2009.

Research Article

Study of Phase Change Materials Applied to CPV Receivers

Zun-Hao Shih, Ke-Jen Chain, and Hwen-Fen Hong

Institute of Nuclear Energy Research, Atomic Energy Council, Taoyuan County 32546, Taiwan

Correspondence should be addressed to Zun-Hao Shih; shihzunhao@iner.gov.tw

Received 26 September 2014; Accepted 5 April 2015

Academic Editor: Fathallah Karimzadeh

Copyright © 2015 Zun-Hao Shih et al. This is an open access article distributed under the Creative Commons Attribution License, which permits unrestricted use, distribution, and reproduction in any medium, provided the original work is properly cited.

There are lots of factors which can directly affect output efficiency of photovoltaic device. One of them is high temperature which would cause adverse effect to solar cell. When solar cell is operated in high temperature, the cell's output efficiency will become low. Therefore, improving thermal spreading of solar cell is an important issue. In this study, we focused on finding new materials to enhance the thermal disspreading and keep the temperature of solar cell as low as possible. The new materials are different from conventional metal ones; they are called "phase change materials (PCMs)" which are mainly applied to green buildings. We chose two kinds of PSMs to study their thermal disspreading ability and to compare them with traditional aluminum material. These two kinds of PCMs are wax and lauric acid. We made three aluminum-based cuboids as heat sinking units and two of them were designed with hollow space to fill in the PCMs. We applied electric forward bias on solar cells to simulate the heat contributed from the concentrated sunlight. Then we observed the thermal distribution of these three kinds of thermal spreading materials. Two levels of forward biases were chosen to test the samples and analyze the experiment results.

1. Introduction

In the development of concentrating photovoltaic (CPV) technology, heat dissipation is always an important issue that affects the output efficiency of CPV module or receiver. The output power of solar cell is inversely proportional to its operating temperature. The lower temperature solar cell is the higher power it can produce [1]. Currently, the most popular thermal-dissipation structure is aluminum-extruded heat sink with varied shapes, which maximizes the thermal-dissipating surface area to the air. It will increase the efficiency of passive thermal convection and keep the temperature of CPV receivers as low as possible. In this paper, we used different approaches and materials to achieve the new thermal-dissipation path. These materials are called phase change materials (PCMs) which have been applied to thermal storage and green building technology for a long time [2]. Some PCMs with low melting point ($40^{\circ}\text{C}\sim 60^{\circ}\text{C}$) and high latent heat (over 150 J/g) have good ability to reduce room temperature fluctuation as used in the sandwich wall of the buildings.

In this study, some PCMs were used to keep solar cell at a proper temperature for a period of time, making solar module

have better power conversion efficiency. This temperature depends on the melting point of applied PCMs. As a result, the temperature of solar cell could be controlled at an expected value. Therefore, it is important to choose suitable PCMs to perform this experiment.

2. The Thermal Function of Phase Change Materials

There are three kinds of thermal spreading modes in heat transfer mechanism: conduction, convection, and radiation. These are also the core concepts of designing heat sinks. The most common material of heat sink is aluminum due to its high thermal conductive coefficient (167 W/mK) and easy-shaping characteristic. Here we embedded the PCMs into the aluminum heat sink. These materials were expected to add extra heat capacity of the original heat spreading system. The extra heat capacity comes from its high latent heat value that could keep temperature at a specific melting point for a long time and restart to heat up again until PCMs melting into liquid state entirely.

In this paper, two PCMs were used, which were paraffin wax and lauric acid. The properties of these PCMs are listed in

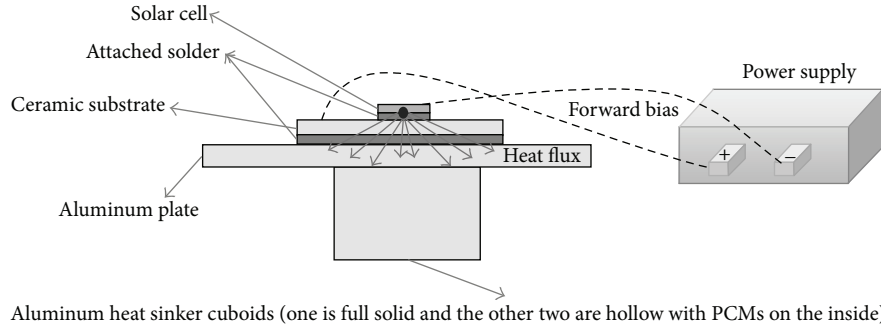


FIGURE 1: Sketch of experiments with solar cell applied forward bias as a heat source center.

TABLE 1: The individual characteristics of the three experimental materials [3, 4].

| Material | Aluminum | Paraffin wax | Lauric acid |
|--|----------|--------------|-------------|
| Density (g/cm^3) | 2.7 | 0.9 | 0.88 |
| Specific heat (solid) ($\text{J}/\text{g}\cdot\text{K}$) | 0.91 | 2.9 | 2.4 |
| Specific heat (liquid) ($\text{J}/\text{g}\cdot\text{K}$) | | 2.13 | 2.0 |
| Latent heat of melting (J/g) | 321 | 189 | 182 |
| Melting point ($^{\circ}\text{C}$) | 660 | 49 | 42 |
| Thermal conductivity (solid state) ($\text{W}/\text{m}\cdot\text{k}$) | 167 | 0.21 | 0.15 |
| Thermal conductivity (liquid state) ($\text{W}/\text{m}\cdot\text{k}$) | | 0.167 | 0.148 |

Table 1 in comparison with aluminum. The melting points of paraffin wax and lauric acid are 49°C and 42°C , respectively. These melting points are at the lower margin of the CPV operating temperature. But there are also some thermal spreading issues of PCMs. First of all, these PCMs often have low thermal conductivity and high thermal resistance comparing with aluminum. Another issue is that the PCMs cannot contact directly with solar cell since there are some interface materials and circuit board between them. It will affect heat absorption efficiency of PCMs. In this study, some samples were fabricated to verify these issues.

3. Experimental Parameters and Conditions

For our thermal spreading and dissipating experiment, we designed a modified structure from our original CPV receiver, as shown in Figure 1. The test receiver had several components and was packaged by SMT. First of all, the backsides of the solar cells were connected with the gold contact electrode pads of the ceramic substrates by solder. We joined the topsides of the dies and the circuit of the ceramic substrates with wire bonding. The backsides of the ceramic substrates were integrated in the topside of the aluminum plate to form the primary part of CPV receiver. Finally three aluminum cuboids were fixed on the backside of the CPV receiver and located at bottom center of each solar cell. We fabricated two different types of the cuboids, shown in Figure 2, to execute our PCMs thermal-dissipation

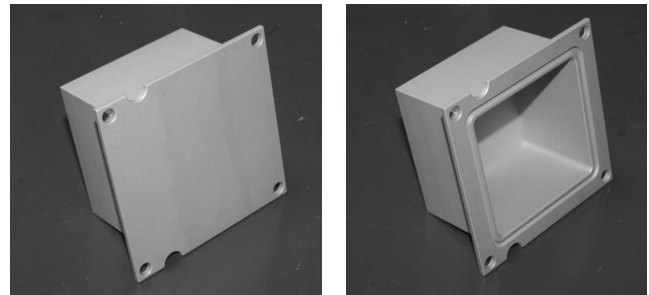


FIGURE 2: The two types of the aluminum heat sinker cuboids for the thermal dissipating experiment.

experimental analysis. One type of the cuboids was a solid aluminum bulk as reference sample. Another type was a hollow cuboid which would fill with PCM as test sample. Furthermore, two kinds of PCMs were filled into the hollow cuboids, which were paraffin wax and lauric acid. All of them were attached directly onto the backside of the aluminum plate of CPV receiver. Therefore, there were three different samples in the CPV receiver and the solar cells of each sample were connected in series.

For establishing a stable and equal heat source, we used a power supply to bias the solar cells with a 4A or 6A forward current continuously in the laboratory for 100 minutes instead of irradiating by unstable outdoor sunlight. When the solar cells were in forward bias, they would become LED-like devices and consume the input electric power into heat and light. During this process, we observed the temperature change and distribution of these three samples on the topside of the CPV receiver by thermal image instrument. The room temperature and humidity were controlled by the air conditioner.

4. Result and Discussion

The first experimental condition was that the CPV receiver was biased continuously by fixed-value 6A forward current in 100 minutes to observe the thermal spreading pattern. After the experiment, the thermal-equilibrium temperatures of the solar cells of these three samples were 71.9°C for lauric acid, 71.6°C for aluminum bulk, and 73.5°C for paraffin wax, respectively, as shown in Figure 3. These temperature values

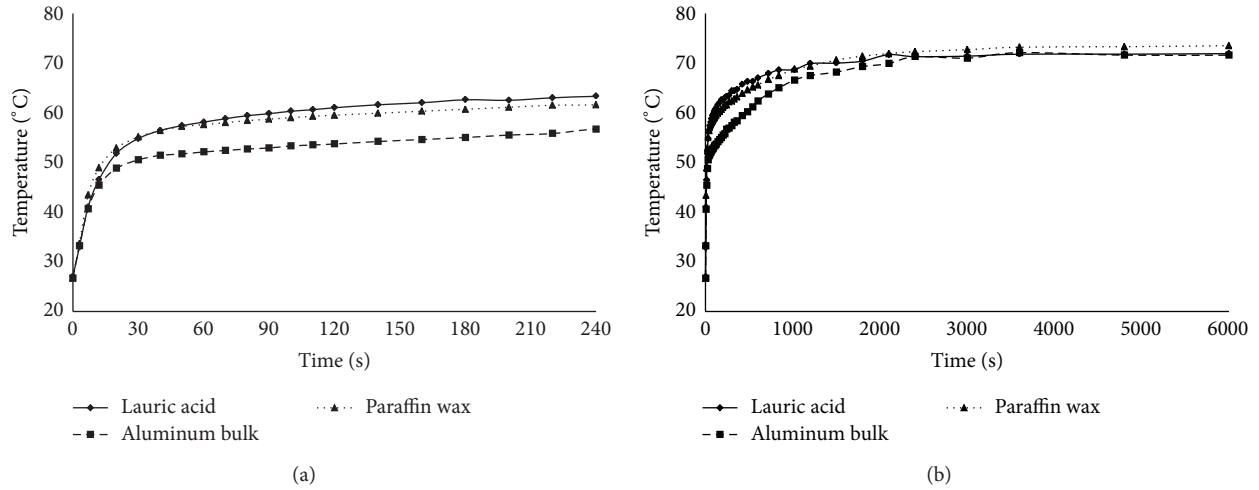


FIGURE 3: (a) The first two-minute and (b) the 100-minute temperature variations of the solar cells of the three experimental samples under 6A forward current injection.

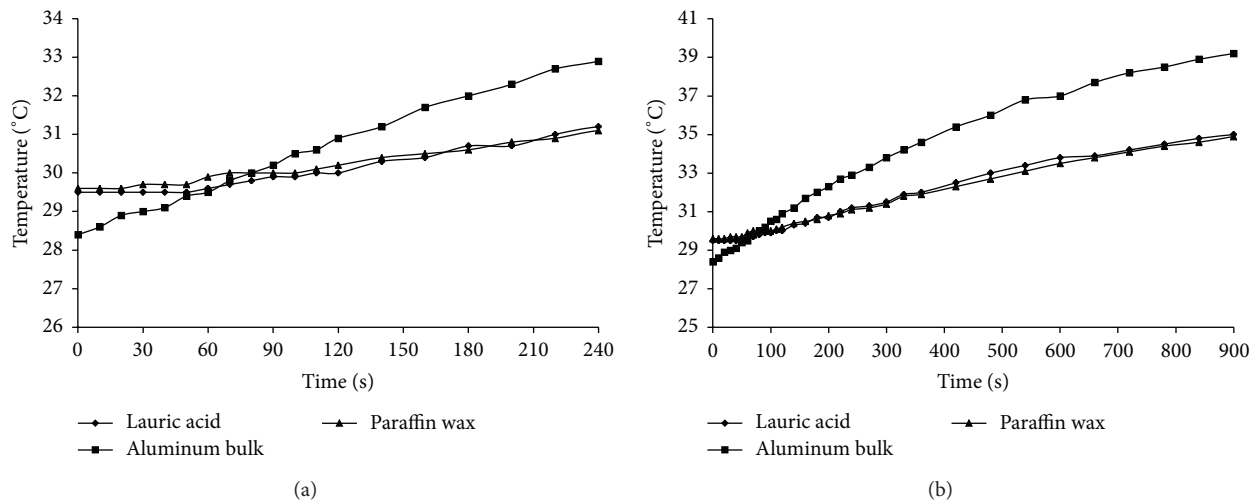


FIGURE 4: (a) The first two-minute and (b) the fifteen-minute bottom temperature values of the three cuboids measured by IR image instrument.

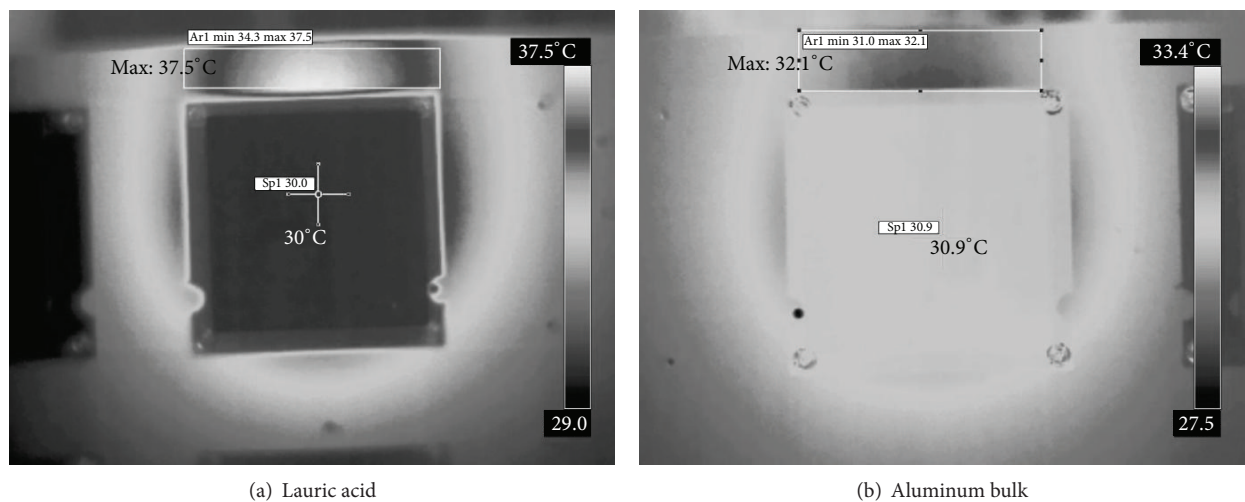


FIGURE 5: The thermal images of the test samples which were heated two minutes ((a) is lauric acid and (b) is aluminum bulk).

were quite close to the outdoor operating temperature of solar cell in the sunny summer. The result showed that the entire thermal spreading and dissipating efficiency of these three samples were quite close, too.

Another focus of observation was the different temperature-rising curves of the three samples during the first two minutes of heating. For the sample with the aluminum bulk, temperature rising rate of its solar cell was the lowest. This was because aluminum bulk had most outstanding thermal conductive efficiency of all samples. The quantity of heat which was transferred quickly from the solar cell to the bottom of the aluminum bulk was more than the PCMs samples. Then there was the highest temperature value on the backside of the sample with aluminum bulk in first two and entire fifteen minutes, as shown in Figures 4(a) and 4(b), respectively. In another view, the comparison of two thermal images which is backsides of the samples with aluminum bulk and lauric acid was shown in Figure 5. When the CPV receiver was heat by forward current in two minutes, the temperature in the plate region of the lauric acid sample was 37.5°C (maximum value) and 30°C in the bottom of the cuboid. The different between the two measured points was 7.5°C. For the sample with aluminum bulk, the different value was only 1.2°C. Further the 3D temperature distribution in the zone of the each PCMs sample was more wide range and higher than the aluminum bulk sample after being biased two minutes, as shown in Figure 6. The heat was transferred less efficiently downward to the cuboids due to the lower thermal conductivity of the PCMs and the thermal crowding in the nearby region of the solar cells caused temperature increase more quickly.

In addition the thermal spreading and dissipating experimental result showed another phenomenon that the solar cell did not keep in a specific temperature point which was equal to melting point of lauric acid or paraffin wax. It was also due to large thermal conductive different among aluminum and PCMs. In the CPV receiver structure here, the PCMs were surrounded by aluminum and did not touch the solar cells directly. There were too many interface materials to have good heat absorption efficiency for the PCMs. When the heat absorption of the PCMs was less efficient than the heat generation from power supply, it caused that the temperature value of the solar cell would be higher than the melting point of the PCM. Although the temperature value of the solar cell was not entirely controlled in our default method, effect of the PCM still happened in the cuboid of the CPV receiver backside. The temperature values of the samples in the CPV backside were close to the melting points of the two PCMs and the thermal equilibrium was also shown in Figure 7. The Sp3 point was 43°C and Sp4 was 43.3°C; furthermore, these temperature values were very close to the melting points of the lauric acid and paraffin wax, respectively. The PCMs were in touch directly with the whole inner surface of the cuboids, so the thermal transference and absorption would have more efficiency and immediacy than the heat flow from the solar cells to the PCMs. The outcome was that the temperature difference from cuboid to PCMs was smaller than from solar cell to PCMs. If the CPV system operates in the field, the lower backside temperature of the CPV module

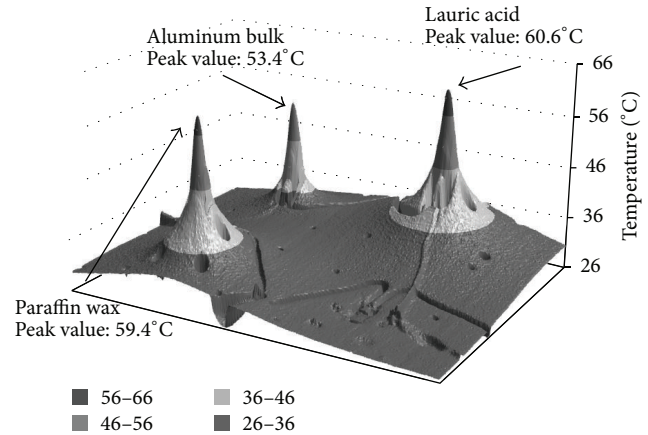


FIGURE 6: Highest temperature value and 3D thermal distribution of each test sample on CPV receiver topside in first two minutes of forward biasing.

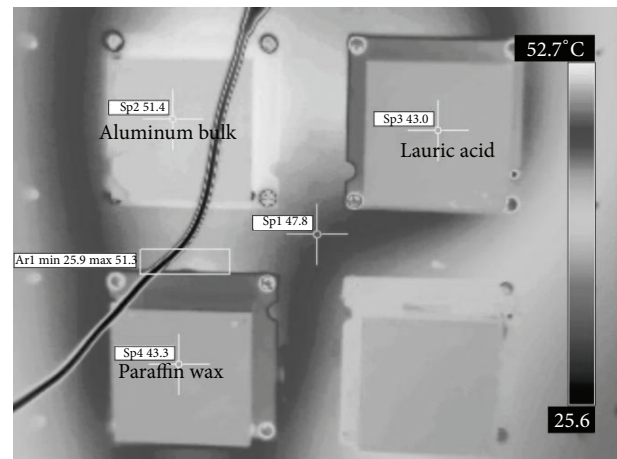


FIGURE 7: The highest temperature values of the three bottoms of the cuboids measured after heating in 100 minutes.

will have more superior protection for system operators and maintenance staffs. It still had benefit for the development of the CPV technology to strengthen workplace safety.

We tested another experimental parameter for observation of lower thermal spreading situation. The 4A forward current which was given by power supply was injected into the three test samples continuously for 100 minutes and the result was shown in Figures 8(a) and 8(b). In the lower input power case, the three thermal-equilibrium temperature values of the samples were, respectively, 56°C for lauric acid, 55.9°C for aluminum bulk, and 56.8°C for paraffin wax. The difference of the temperature-rising curves was closer than the previous experiment. Because the input power was lower, the thermal accumulation was less. Therefore, the main thermal spreading and dissipating mechanism was the same with 6A current injection case. From the results of these two experimental parameters, we could find that the quantity of the input power did not influence distinctly

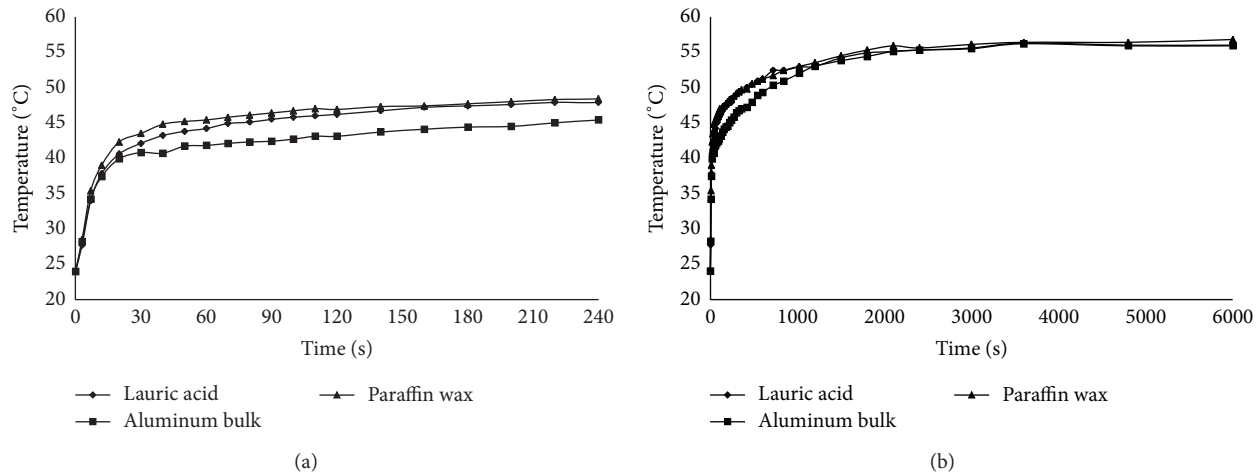


FIGURE 8: (a) The first two-minute and (b) the 100-minute temperature variations of the solar cells of the three experimental samples under 4A forward current injection.

the heating-rising trend and the difference of the thermal-equilibrium temperature values in the CPV receiver. The behavior patterns and mechanisms of the 4A and 6A current injections were quite the same.

5. Conclusion

We tried to develop innovative thermal sinking method to decrease the operating temperature of the solar cells in the CPV receiver. However the PCMs were not an effective improvement for the heat sinking of these solar cells. The shape of this experimental sample was cuboid, and then we would try to fabricate other shapes to test more conditions in the future. Although there were the similar temperature values of the solar cells of the test samples for all materials in the thermal equilibrium by heating, it had improved the backside temperature of the CPV receiver indeed. This experiment is the beginning application of the PCMs in the CPV field and it has still many unexplored questions to be found and solved.

Conflict of Interests

The authors declare that there is no conflict of interests regarding the publication of this paper.

References

- [1] G. Peharz, J. P. Ferrer Rodríguez, G. Siefert, and A. W. Bett, "Investigations on the temperature dependence of CPV modules equipped with triple-junction solar cells," *Progress in Photovoltaics: Research and Applications*, vol. 19, no. 1, pp. 54–60, 2011.
- [2] A. Sharma, V. V. Tyagi, C. R. Chen, and D. Buddhi, "Review on thermal energy storage with phase change materials and applications," *Renewable and Sustainable Energy Reviews*, vol. 13, no. 2, pp. 318–345, 2009.
- [3] B. Zalba, J. M. Marín, L. F. Cabeza, and H. Mehling, "Review on thermal energy storage with phase change: materials, heat transfer analysis and applications," *Applied Thermal Engineering*, vol. 23, no. 3, pp. 251–283, 2003.
- [4] R. Murray, "Design of a latent heat energy storage system coupled with a domestic hot water solar thermal system," in *Proceedings of the World Renewable Energy Congress*, Stockholm, Sweden, May 2011.

Research Article

Ab Initio Theoretical Investigation on the Geometrical and Electronic Structures of Gallium Aurides: $\text{GaAu}_n^{0/-}$ and $\text{Ga}_2\text{Au}_n^{0/-}$ ($n = 1-4$)

Wen-Zhi Yao,¹ Jian-Bin Yao,² and Si-Dian Li³

¹Department of Environmental and Municipal Engineering, North China University of Water Conservancy and Electric Power, Zhengzhou 450011, China

²Department of Information Engineering, North China University of Water Conservancy and Electric Power, Zhengzhou 450011, China

³Institute of Molecular Science, Shanxi University, Taiyuan 030001, China

Correspondence should be addressed to Wen-Zhi Yao; yaowenzhi-1982@163.com

Received 20 June 2014; Accepted 30 July 2014

Academic Editor: Jian Sun

Copyright © 2015 Wen-Zhi Yao et al. This is an open access article distributed under the Creative Commons Attribution License, which permits unrestricted use, distribution, and reproduction in any medium, provided the original work is properly cited.

This study presents a systematic investigation of the geometric and electronic properties of $\text{GaAu}_n^{0/-}$ and $\text{Ga}_2\text{Au}_n^{0/-}$ ($n = 1-4$) clusters based on density functional theory and wave function theory. Detailed orbital analyses, adaptive natural density partitioning, and electron localization function analyses are performed and relevant results are discussed. $\text{GaAu}_n^{0/-}$ ($n = 1-4$) clusters with n -Au terminals and $\text{Ga}_2\text{Au}_n^{0/-}$ ($n = 1-4$) clusters with bridged Au atoms possess geometric structures and bonding patterns similar to those of the corresponding gallium hydrides $\text{GaH}_n^{0/-}$ and $\text{Ga}_2\text{H}_n^{0/-}$. Ga–Au interaction is predicted to occur through highly polar covalent bonds in monogallium aurides. In contrast to the highly symmetric ground states of C_{2v} , Ga_2Au , C_{2v} , Ga_2Au_2 , and D_{3h} , Ga_2Au_3 , C_{3v} , Ga_2Au_4 is composed of strong interactions between a Ga^+ cation and the face of a tetrahedral GaAu_4^- anion. The adiabatic and vertical detachment energies of the anions under study are calculated to facilitate their experimental characterization. Geometric and electronic structural comparisons with the corresponding gallium hydrides are conducted to establish an isolobal analogy between gold and hydrogen atoms.

1. Introduction

Considering its strong relativistic effects, Au is highly different from other coinage metals (Cu and Ag); Au has the highest electron affinity (2.3086 eV) of any element other than the halogens as well as the highest electron negativity (2.4 in the Pauling scale) among all of the metals [1–4]. The H/Au isolobal is an extension of the most remarkable experimental discovery of the H/AuPR₃ analogy thus far and has helped elucidate the structures and bonding types in various ligated Au compounds [5, 6]. The H/Au isolobal relationship in gas-phase Si–Au alloy clusters and B–Au alloy clusters, such as $\text{SiAu}_4^{0/-}$ [7], $\text{Si}_2\text{Au}_x^{0/-}$ ($x = 2, 4$) [8, 9], Si_3Au_3 , $\text{B}_7\text{Au}_2^{0/-}$ [10], $\text{B}_6\text{Au}_n^{0/-}$ ($n = 1-3$) [11], $\text{B}_{10}\text{Au}^{0/-}$ [12], and closo-aurobranes $\text{B}_n\text{Au}_n^{2-}$ ($n = 5-12$) [13], has been confirmed by joint photoelectron spectroscopy (PES) and density functional

theory (DFT) investigations. Various compounds with 2c–2e N–Au and B–Au bonds [14–17], relativistic pseudopotential calculations on XAu_n^{m+} containing Au ligands ($X = \text{B-N, Al-S, } n = 4-6$) [18], and Au-bridged $\text{X} \cdots \text{Au-Y}$ Lewis acid-base pairs have also been reported [19].

The H/Au analogy has recently motivated our group to analyze the geometric and electronic structures of electron-deficient B–Au and Al–Au alloy small clusters, such as those of $\text{BAu}_n^{0/-}$ ($n = 1-4$) [20], $\text{B}_2\text{Au}_n^{0/-}$ ($n = 1, 3, 5$) [21], $\text{B}_2\text{Au}_2^{0/-/2-}$ [22], $\text{AlAu}_n^{0/-}$ ($n = 2-4$) [23], $\text{Al}_2\text{Au}_n^{0/-}$ ($n = 1-3$) [24], $\text{B}_2\text{Au}_4^{0/-}$, and $\text{Al}_2\text{Au}_4^{0/-}$, based on *ab initio* theories. These studies reveal a clear structural link between electron-deficient Au-containing clusters and the corresponding hydride molecules. Comparative studies on the properties of group IIIA element–Au alloy clusters have also attracted our interest. Boron, aluminum, and gallium

hydrides, as well as their corresponding Au compounds, show several similarities and differences. To the best of our knowledge, no investigations on gallium aurides are yet available.

The present study describes a detailed *ab initio* investigation on the geometric and electronic structures of $\text{GaAu}_n^{0/-}$ and $\text{Ga}_2\text{Au}_n^{0/-}$ ($n = 1-4$) based on DFT and wave function theory. Natural resonance theory (NRT) and electron localization function (ELF) [25, 26] are performed to characterize Ga–Au bonds in monogallium aurides. Natural localized molecular orbitals (NLMO) and adaptive natural density partitioning (AdNDP) [27] are performed to discuss the chemical bonding in digallium aurides. The adiabatic electron detachment energies (ADEs) and vertical electron detachment energies (VDEs) of GaAu_n^- and Ga_2Au_n^- ($n = 1-4$) anions are calculated to aid their PES characterization. The results obtained in this work extend the concept of bridging Au interactions and enrich the chemistry of Au.

2. Theoretical Methods

Structural optimizations and frequency analyses were conducted on low-lying isomers using the hybrid B3LYP method [28, 29] and the second-order Møller-Plesset approach by frozen core approximation [MP2(FC)] [30, 31]. MP2 produces ground state structures and relative energy orders similar to B3LYP with slightly different bond parameters. Relative energies for the lowest-lying isomers were further refined using the coupled cluster method with triple excitations [CCSD(T)] [32] at B3LYP structures. Stuttgart quasi-relativistic pseudopotentials and basis sets augmented with two f-type polarization functions and one g-type polarization function (Stuttgart_rsc_1997_eCP+2f1g ($\alpha(f) = 0.498$, $\alpha(g) = 1.464$, and $\alpha(g) = 1.218$)) [33] were employed for Au with 19 valence electrons. The augmented Dunning's correlation consistent basis set of aug-cc-pvTZ [34] was used for Ga throughout this work. Bonding analyses were accomplished using NRT, NLMO, AdNDP [27], and ELF [25, 26]. The ADEs and VDEs of the anions were calculated as the energy differences between the anions and the corresponding neutrals at their ground state and anionic structures, respectively. All calculations in this work were performed using Gaussian 09 [35]. AdNDP and ELF analyses were performed with Multiwfn [36]. The NBO5.0 [37] program was used to calculate bond orders and atomic charges.

3. Results and Discussion

3.1. Geometric and Electronic Structures of GaAu_n and GaAu_n^- ($n = 1-4$). $\text{GaAu}_n^{0/-}$ ($n = 1-4$) clusters with n–Au terminals possess geometric structures and bonding patterns similar to those of the corresponding gallium hydrides $\text{GaH}_n^{0/-}$ [38]. As shown in Figure 1, low-spin electronic states are consistently favored in $\text{GaAu}_n^{0/-}$ ($n = 1-4$). At all levels of theory, the ground structure GaAu^- anion (**1**, $^2\Sigma^+$) has a bond length of $r_{\text{Ga-Au}} = 2.52 \text{ \AA}$ and is 1.76 eV more stable than its quartet isomer (**2**, $^4\Sigma^+$) at the CCSD(T) level. The most stable

GaAu neutral structure (**3**, $^1\Sigma^+$) possesses a bond length of $r_{\text{Ga-Au}} = 2.45 \text{ \AA}$. For GaAu_2 , the V-shaped C_{2v} GaAu_2^- (**5**, 1A_1) with a bond length of $r_{\text{Ga-Au}} = 2.55 \text{ \AA}$ is the ground state and is 0.80 eV more stable than the linear $C_{\infty v}$ GaAu_2^- (**6**, $^1\Sigma^+$) at the CCSD(T) level. V-shaped C_{2v} GaAu_2 (**7**, 2B_2) is the most stable geometry on the potential surface of neutral GaAu_2 . A large geometric change may be observed upon electron detachment from the anion C_{2v} GaAu_2^- **4** to the neutral C_{2v} GaAu_2 **7**, although these molecules have the same symmetry: the Ga–Au bond length increases by 0.08 Å, the Au–Au distance decreases by 1.19 Å, and the Au–Ga–Au bond angle considerably decreases by 38° in the anion relative to the neutral molecule.

The perfect planar triangular GaAu_3^- structure has D_{3h} symmetry (**9**, $^2A_1'$) with a bond length of $r_{\text{Ga-Au}} = 2.49 \text{ \AA}$ and an Au–Ga–Au bond angle of $\text{AuGaAu} = 120^\circ$. This structure is the ground state form and is 0.18 eV more stable than the off-plane C_s GaAu_3^- (**10**, $^2A_1'$) at the CCSD(T) level. Neutral GaAu_3 (**11**, $^1A_1'$) with an sp^2 hybridized Ga at the center of the molecule is a closed-shell singlet with D_{3h} symmetry. Compared with the anion, the neutral molecule only exhibits slight shortening of the Ga–Au bond length (0.1 Å).

On GaAu_4^- , we calculated several isomers and found that the perfect tetrahedral T_d GaAu_4^- (**13**, 1A_1) has an sp^3 hybridized Ga. This structure is the ground geometry; here, the four –Au terminals are singly σ -bound to the central Ga with a bond length of $r_{\text{Ga-Au}} = 2.45 \text{ \AA}$ and a Wiberg bond index of $\text{WBI}_{\text{Ga-Au}} = 0.93$. T_d GaAu_4^- (**13**) is separated by at least 0.14 eV from other 2D and 3D isomers at the CCSD(T) level, which suggests that an Ga^- tetrahedral center is strongly favored in the GAu_4^- anion. Interestingly, T_d GaAu_4^- (**13**) has the shortest Ga–Au bond length and the largest HOMO-LUMO energy gap of $\Delta E_{\text{gap}} = 2.89 \text{ eV}$ in the GaAu^- series. Detaching one electron from the perfect tetrahedral T_d GaAu_4^- (**13**) involves a John-Teller process to produce the severely distorted global minimum of C_s GaAu_4 (**16**, $^2A_1'$), which lies at least 0.22 eV higher than those of other low-lying isomers at the CCSD(T) level.

3.2. Bonding Consideration of GaAu_n and GaAu_n^- ($n = 1-4$). NRT was used to calculate the bond orders and bond polarities of the molecules under study. As shown in Table 1, covalent contributions to the Ga–Au interactions continuously increase in the GaAu_n^- series from $n = 1$ to $n = 4$. The Ga–Au bonds in T_d GaAu_4^- (**13**) have the highest percentage of covalence (78%). The Ga–Au bonds in D_{3h} GaAu_3^- (**9**), C_{2v} GaAu_2^- (**5**), and $C_{\infty v}$ GaAu^- (**1**) show covalent contributions of 54%, 44%, and 40%, respectively. This result indicates that Ga–Au interactions in the GaAu_n^- series render the characteristics of ionic structures, especially in GaAu_2^- and GaAu^- . The characteristic of the Ga–Au bond in the GaAu_n^- series is also illustrated clearly by ELF analysis [27], which reflects the probability of finding an electron or a pair of pairs in specific basins (Figure 2). Contour line maps of $C_{\infty v}$ GaAu^- (**1**), C_{2v} GaAu_2^- (**5**), D_{3h} GaAu_3^- (**9**), and T_d GaAu_4^- (**13**) reveal the presence of a weak electronic interaction between Ga and Au. This interaction is a highly polar covalent bond. NBO quantitatively reveals

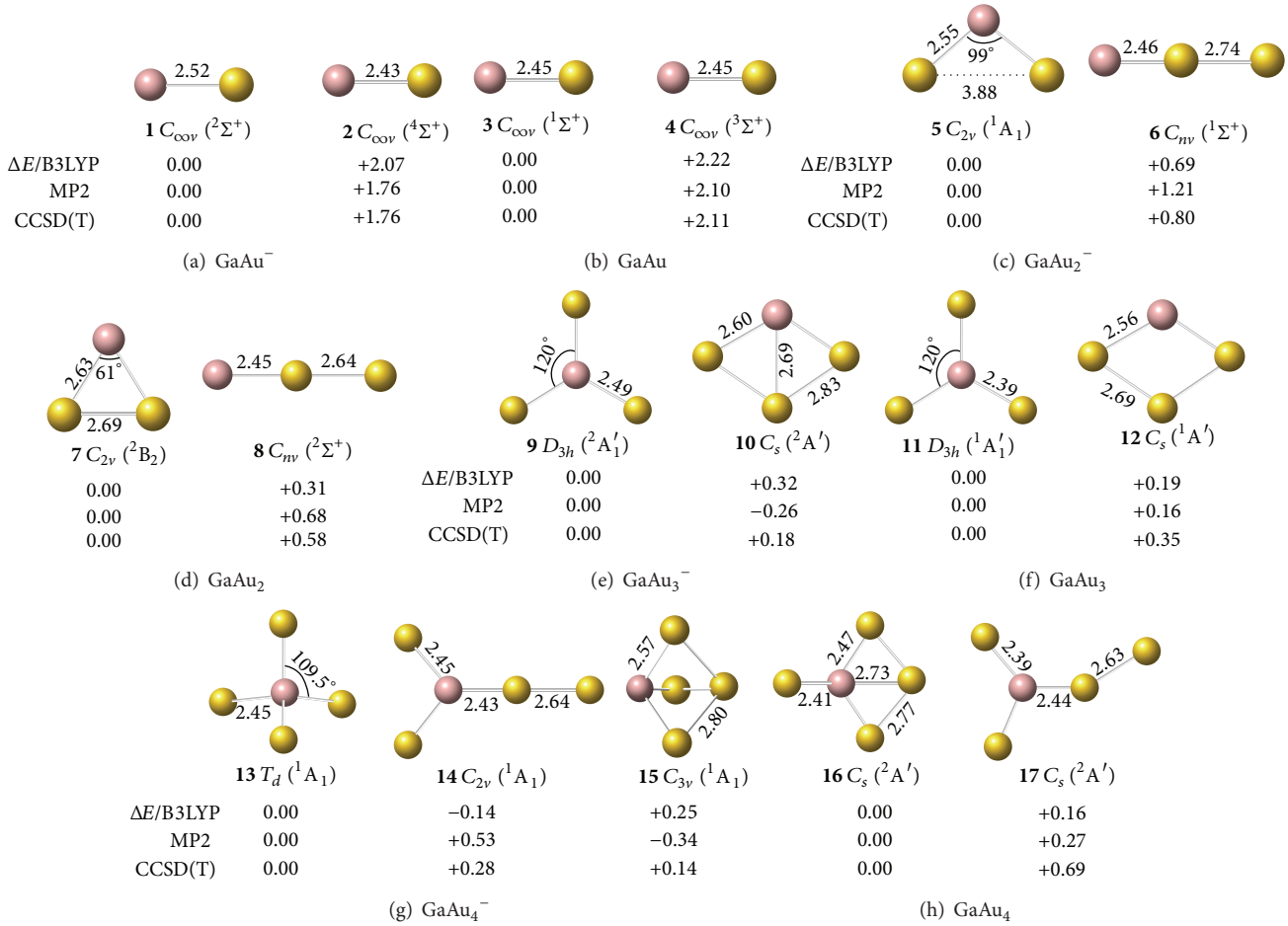


FIGURE 1: Low-lying isomers of (a) GaAu⁻, (b) GaAu, (c) GaAu₂⁻, (d) GaAu₂, (e) GaAu₃⁻, (f) GaAu₃, (g) GaAu₄⁻, and (h) GaAu₄ at the B3LYP level. Relative energies ΔE (eV) at B3LYP//B3LYP, MP2//MP2, and CCSD(T)//B3LYP are also indicated (bond lengths in angstrom and bond angles in degree).

TABLE 1: Full valency, covalency, and electrovalency indices, covalent percentages, and natural atomic charges ($q/|e|$) calculated for GaAu_n⁻ anions.

| Isomers | Atom | Valency | Covalency | Electrovalency | Covalent percentage | q |
|--|------|---------|-----------|----------------|---------------------|-------|
| 1 C _{ooV} GaAu ⁻ | Ga | 1.02 | 0.41 | 0.61 | 0.40 | -0.44 |
| | Au | 1.02 | 0.41 | 0.61 | 0.40 | -0.56 |
| 5 C _{2v} GaAu ₂ ⁻ | Ga | 2.03 | 0.87 | 1.15 | 0.43 | 0.05 |
| | Au | 1.01 | 0.44 | 0.58 | 0.44 | -0.53 |
| 9 D _{3h} GaAu ₃ ⁻ | Ga | 2.85 | 1.53 | 1.32 | 0.54 | 0.08 |
| | Au | 0.96 | 0.51 | 0.45 | 0.53 | -0.36 |
| 11 T _d GaAu ₄ ⁻ | Ga | 3.77 | 2.95 | 0.82 | 0.78 | -0.34 |
| | Au | 0.94 | 0.74 | 0.20 | 0.79 | -0.17 |

the Ga–Au bonding properties: the Ga–Au bond length of $r_{\text{Ga–Au}} = 2.45\text{--}2.55$ Å and the corresponding bond order of $\text{WBI}_{\text{Ga–Au}} = 0.73\text{--}0.90$ in the GaAu_n⁻ series. These properties further indicate that the interaction is covalent but with ionic characteristics.

In the GaAu_n⁻ series, the perfect tetrahedral T_d GaAu₄⁻ (13) is unique. Figure 3 shows the four valence molecular orbitals of the molecule, including a triply degenerate HOMO

(t₂) and a singlet HOMO-1 (a₁). T_d GaAu₄⁻ has a bonding pattern similar to that of T_d GaH₄⁻, with an sp³ hybridized Ga center surrounded by four Au atoms to form four equivalent σ single bonds. The B–Au and B–H σ bonds in T_d GaAu₄⁻ and T_d GaH₄⁻ show subtle differences in orbital composition because of obvious relative effects in Au. T_d GaAu₄⁻ possesses the orbital combination of $\text{MO}_{\text{Ga–Au}} = 0.63(\text{sp}^3)_{\text{Ga}} + 0.77(\text{sd}^{0.05})_{\text{Au}}$ and the corresponding atomic

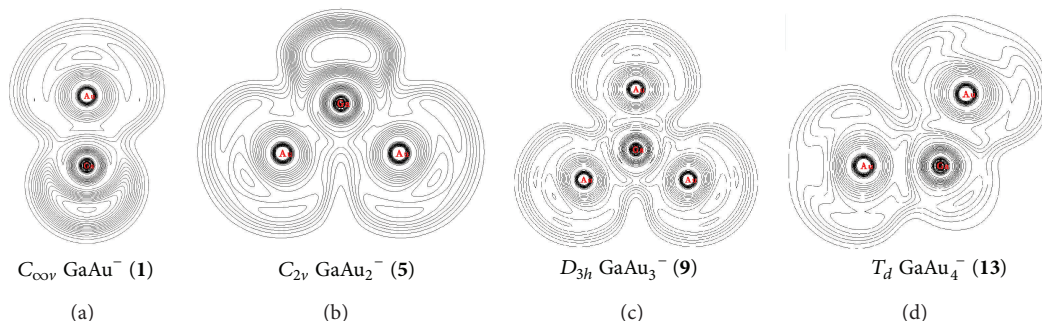


FIGURE 2: Contour line maps of electron localization functions (ELFs) in GaAu⁻ (1), GaAu₂⁻ (5), GaAu₃⁻ (9), and GaAu₄⁻ (13).

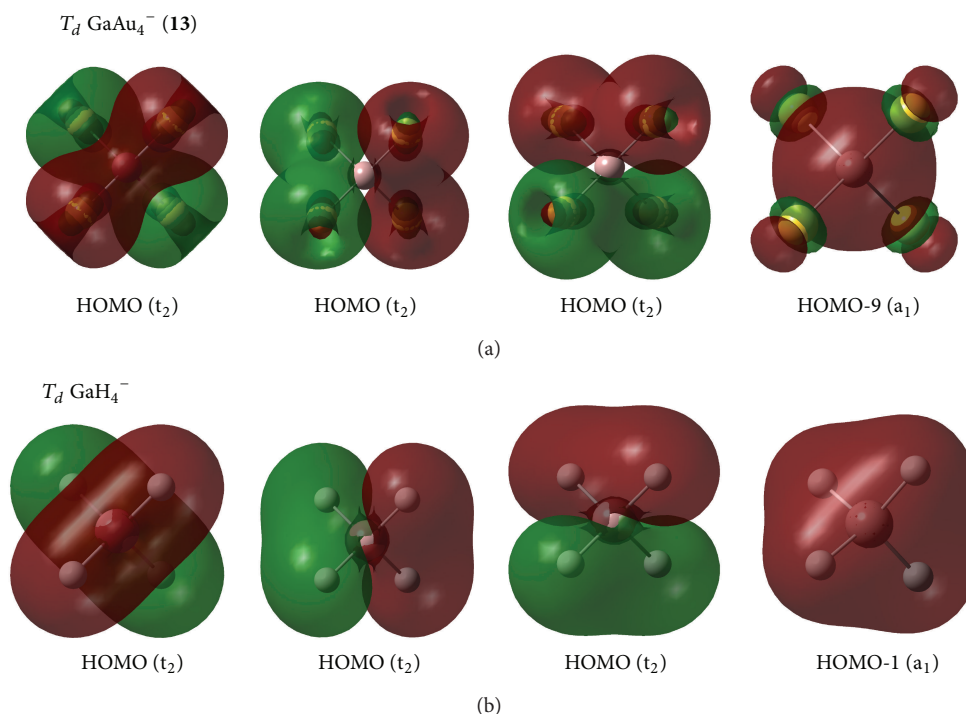


FIGURE 3: Comparison of the four valence MOs responsible for the four equivalent σ -bonds in T_d [GaAu₄]⁻ and T_d [GaH₄]⁻ at the B3LYP level.

contribution of 40%Ga + 60%Au, with Au 6s contributing 95.2% and Au 5d contributing 4.7% to the Au-based orbital. In GaAu_{*n*}^{0/-} (*n* = 1–4), Au 5d contributes 8.5%–4.7% to the Au-based orbital, which is less than that in monoboron aurides.

3.3. Geometric and Electronic Structures of Ga₂Au_{*n*} and Ga₂Au_{*n*}^{0/-} (*n* = 1–4). All low-lying neutral and anion clusters of Ga₂Au_{*n*}^{0/-} (*n* = 1–4) are summarized in Figure 4. Ga₂Au_{*n*}^{0/-} (*n* = 1–4) clusters with bridged Au atoms possess geometric structures similar to those of the corresponding gallium hydrides Ga₂H_{*n*}^{0/-} [38]. As shown in Figures 4(a) and 4(b), the smallest digallium auride Ga₂Au^{0/-} contains a bridging Au atom. Anionic Ga₂Au⁻ exhibits three possible structures: triplet Au-bridged V-shaped (C_{2v} , **18**, 3B_1), singlet

Au-bridged V-shaped (C_{2v} , **19**, 1A_1), and triplet linear ($C_{\infty v}$, **20**, $^3\Sigma_g^-$). At the CCSD(T) level, the triplet Au-bridged structure **18** with bond lengths of $r_{\text{Ga-Au}} = 2.62 \text{ \AA}$ and $r_{\text{Ga-Ga}} = 2.67 \text{ \AA}$, respectively, lies 0.22 and 0.47 eV lower than the singlet Au-bridged **19** and triplet linear **20** structures. This result suggests that the triplet Au-bridged C_{2v} Ga₂Au⁻ (3B_1 , **18**) is the ground state of Ga₂Au⁻. Similar to the V-shaped Ga₂H (Ga(μ -H)Ga), the doublet Au-bridged C_{2v} Ga₂Au (**21**, 2B_1) is a global minimum lying 0.72 eV lower than the linear $C_{\infty v}$ Ga₂Au (**22**) at the CCSD(T) level. Adding one Au atom to bridge two Ga atoms in C_{2v} Ga₂Au⁻ (**18**) and C_{2v} Ga₂Au (**21**), respectively, produces the ground states of the off-plane di-Au-bridged C_{2v} Ga₂Au⁻ ([Ga(μ -Au)₂Ga]⁻) (**23**, 2A_1) and C_{2v} Ga₂Au₂ ([Ga(μ -Au)₂Ga]) (**26**, 1A_1), which are at least 0.43 and 0.67 eV, respectively, more stable than other isomers. Di-Au-bridged C_{2v} Ga₂Au₂ (**26**)

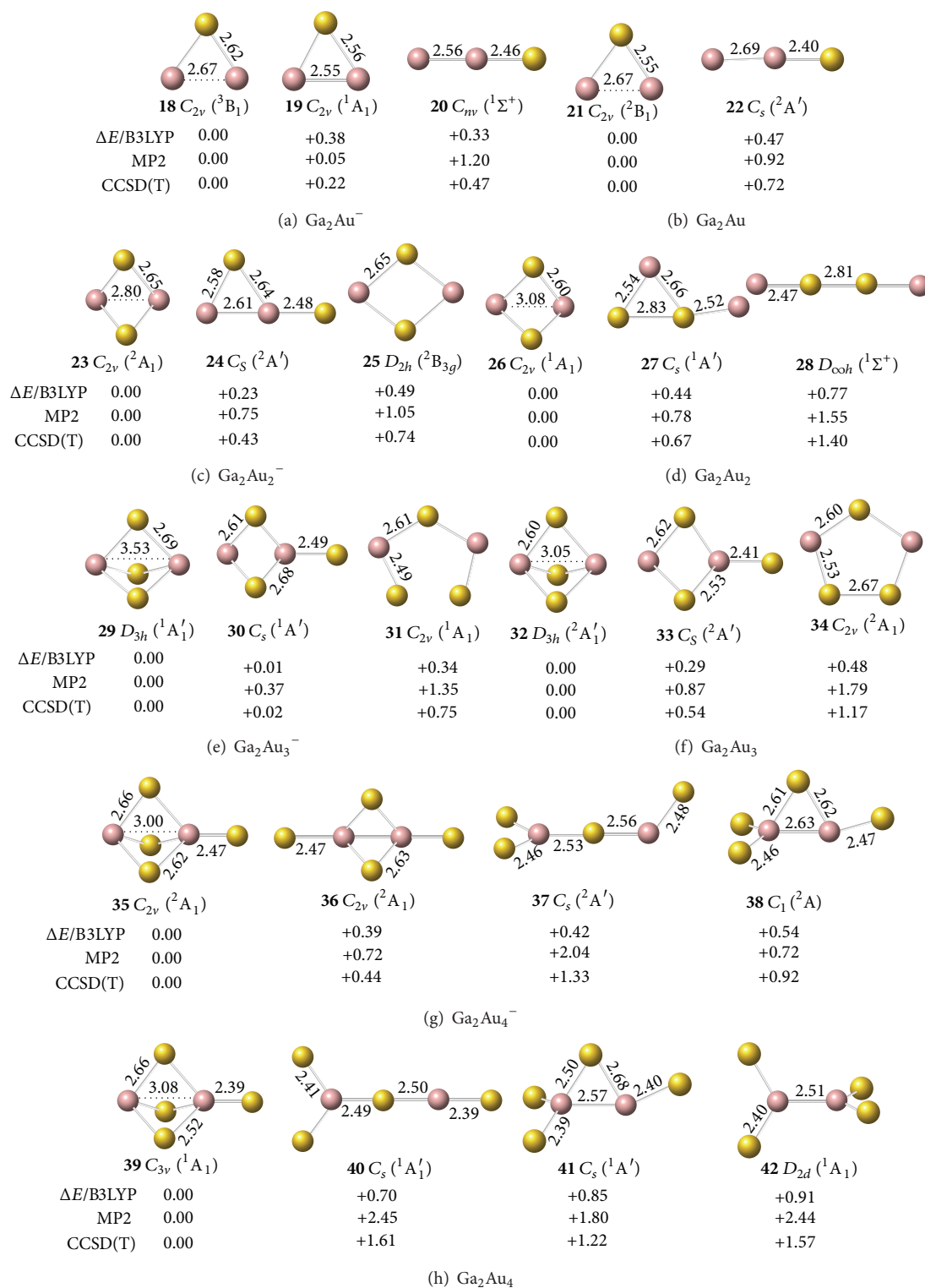


FIGURE 4: Low-lying isomers of (a) Ga_2Au^- , (b) Ga_2Au , (c) Ga_2Au_2^- , (d) Ga_2Au_2 , (e) Ga_2Au_3^- , (f) Ga_2Au_3 , (g) Ga_2Au_4^- , and (h) Ga_2Au_4 at the B3LYP level. Relative energies ΔE (eV) at B3LYP//B3LYP, MP2//MP2, and CCSD(T)//B3LYP are also indicated (bond lengths in angstrom).

possesses the same geometry as di-H-bridged C_{2v} Ga_2H_2 . For $X_2Au_2^{0/-}$ ($X=B, Al, Ga$) systems, the global minima of $Ga_2Au_2^{0/-}$ and $Al_2Au_2^{0/-}$ show similar V-shaped geometries. Both molecules differ from $B_2Au_2^{0/-}$, which favors a linear structure containing a multiple-bonded BB core terminated by two Au atoms. This finding further demonstrates the presence of a strong chemical interaction between two B atoms in diboron aurides.

The interaction between two Ga atoms is so weak that two Au atoms prefer to bond with digallium auride isomers, such as $D_{\infty h}$ Ga_2Au_2 (**28**). The anion $Ga_2Au_3^-$ prefers a tri-Au-bridged $[Ga(\mu-Au)_3Ga]^-$ form with a singlet electronic structure. The most stable geometry of the tri-Au-bridged D_{3h} $Ga_2Au_3^-$ (**29**, $^1A'_1$) with a bond length of $r_{Ga-Au} = 2.69 \text{ \AA}$ is at least 0.37 and 0.02 eV more stable than di-Au-bridged C_s $Ga_2Au_3^-$ (**30**, $^1A'$) at the MP2 and CCSD(T) levels, respectively. Similar to Ga_2H_3 favoring a tri-H-bridged $[Ga(\mu-H)_3Ga]$ structure, the global minimum of Ga_2Au_3 is the tri-Au-bridged D_{3h} Ga_2Au_3 ($^2A'_1$, **32**), which lies 0.54 and 1.17 eV lower than di-Au-bridged C_s $Ga_2Au_3^-$ (**33**, $^2A'$) and planar C_{2v} $Ga_2Au_3^-$ (**34**, 2A_1), respectively. The Ga–Ga distance decreases by 0.48 \AA and the Ga–Au bond length decreases by 0.09 \AA in anion **29** relative to the neutral molecule **32**. This result indicates a large geometry change upon electron detachment from the anion to the neutral molecule, although they have the same symmetry.

Adding one Au atom terminally to a Ga in D_{3h} $Ga_2Au_3^-$ $[Ga(\mu-Au)_3Ga]^-$ (**29**, $^1A'_1$) produces the ground state of tri-Au-bridged C_{3v} $Ga_2Au_4^-$ $[Ga(\mu-Au)_3Ga]Ga^-$ (**35**, 2A_1), which is 0.44, 1.33, and 0.92 eV more stable than di-Au-bridged C_{2v} $Ga_2Au_4^-$ (**36**, 2A_1), distorted Y-shaped C_s $Ga_2Au_4^-$ (**37**, $^2A'$), and mono-Au-bridged C_1 $Ga_2Au_4^-$ (**38**, 2A) at the CCSD(T) level, respectively. Ga_2Au_4 has the same high-symmetry ground state of tri-Au-bridged C_{3v} Ga_2Au_4 $Au^+[Ga(\mu-Au)_3Ga]^-$ (**39**, 1A_1), which lies 1.61, 1.22, and 1.57 eV lower than Y-shaped C_s Ga_2Au_4 (**40**, $^1A'$), mono-Au-bridged Ga_2Au_4 (**41**, $^1A'$), and nonbridged perpendicular D_{2d} Ga_2Au_4 (**42**, 1A_1), respectively. Similar to the tri-H-bridged C_{3v} Ga_2H_4 [39], tri-Au-bridged C_{3v} Ga_2Au_4 (**39**) is composed of strong interactions between a Ga^+ cation and the face of a tetrahedral $GaAu_4^-$ anion. The global minima of Ga_2Au_4 and Al_2Au_4 have the same ionic conformer; both molecules differ from B_2Au_4 , which has a di-Au-bridged covalent structure.

3.4. Bonding Consideration of Ga_2Au_n and $Ga_2Au_n^-$ ($n = 1-4$). AdNDP analysis [27] is an effective tool for analyzing the bonding patterns of various organic and inorganic molecules. As shown in Figure 5, other bonds besides the lone pairs of the Au atom may be analyzed as follows. C_{2v} Ga_2Au (**21**) contains one localized Ga–Ga 2c–2e σ -bond with an occupation number of ON = 1.96 |e|, one localized Ga–Ga 2c–2e σ -anti-bond with an occupation number of ON = 1.96 |e|, and one delocalized Ga–Au–Ga 3c–2e bond with an occupation number of ON = 2.00 |e|. C_{2v} Ga_2Au_2 (**26**) contains one localized Ga–Ga 2c–2e σ -bond with an occupation number of ON = 1.90 |e|, one localized Ga–Ga 2c–2e σ -anti-bond with

an occupation number of ON = 1.90 |e|, and two delocalized Ga–Au–Ga 3c–2e bonds with an occupation number of ON = 1.97 |e|. D_{3h} Ga_2Au_3 (**32**) contains three delocalized Ga–Au–Ga 3c–2e bonds with an occupation number of ON = 1.94 |e|. C_{3v} Ga_2Au_4 (**39**) contains one localized $Ga_{(2)}-Au_{(t)}$ 2c–2e σ -bond with an occupation number of ON = 1.95 |e| and three delocalized Ga–Au–Ga 3c–2e bonds with an occupation number of ON = 1.93 |e|. The same number of electrons occupies the bonding and antibonding orbitals in C_{2v} Ga_2Au (**21**) and C_{2v} Ga_2Au_2 (**26**). Thus, no electronic effect is produced between two Ga atoms and the delocalized Ga–Au–Ga 3c–2e bond is the main interaction in high symmetric Ga_2Au_n ($n = 1-4$).

Detailed NLMO analyses quantitatively reveal the existence of bridging Ga–Au–Ga 3c–2e bonds in C_{2v} Ga_2Au (**21**), C_{2v} Ga_2Au_2 (**26**), D_{3h} Ga_2Au_3 (**32**), and C_{3v} Ga_2Au_4 (**39**), as clearly shown in an image of their 3c–2e orbital and orbital combination (Figure 6). In C_{2v} Ga_2Au (**21**), the 3c–2e bond possesses the orbital combination of $\tau_{Ga-Au-Ga} = 0.38(sp^{99.9})_{Ga} + 0.83(sd^{0.02})_{Au} + 0.38(sp^{99.9})_{Ga}$ and the corresponding atomic contribution of 15%Ga + 70%Au + 15%Ga. In the Ga–Au–Ga 3c–2e bond, Au 6s contributes 97.8% and Au 5d contributes 1.64% to the Au-based orbital, whereas Ga 4p contributes 98.2% and Ga 4s contributes 0.76% to the Ga-based orbital. Obviously, Au 6s and Ga 4p provide the largest contributions to the Ga–Au–Ga 3c–2e bond, and it can be practically approximated as $\tau_{Ga-Au-Ga} = 0.38(p)_{Ga} + 0.83(sd^{0.02})_{Au} + 0.38(p)_{Ga}$. The orbital combinations of Ga–Au–Ga 3c–2e bond in C_{2v} Ga_2Au_2 (**26**) [$\tau_{Ga-Au-Ga} = 0.39(p)_{Ga} + 0.83(sd^{0.01})_{Au} + 0.39(p)_{Ga}$] and D_{3h} Ga_2Au_3 (**32**) [$\tau_{Ga-Au-Ga} = 0.42(p)_{Ga} + 0.80(sd^{0.02})_{Au} + 0.42(p)_{Ga}$] are surprisingly similar to that of C_{2v} Ga_2Au (**21**). However, the composition of the 3c–2e orbital in C_{3v} Ga_2Au_4 (**39**) is obviously different from that in Ga_2Au_n ($n = 1-3$). Each 3c–2e bond has an orbital combination of $\tau_{Ga(1)-Au-Ga(2)} = 0.40(sp^{99.9})_{Ga(1)} + 0.70(sd^{0.02})_{Au} + 0.59(sp^{4.73})_{Ga(2)}$ and the corresponding atomic contribution of 16%Ga₍₁₎ + 50%Au + 35%Ga₍₂₎.

In the bridging $Ga_{(1)}-Au-Ga_{(2)}$ 3c–2e bond, bridged Au 6s and 5d, respectively, contribute 80.7% and 1.4% to the Au-based orbital, Ga₍₁₎ 4s and 4p, respectively, contribute 0.7% and 98.6% to the Ga₍₁₎-based orbital, and Ga₍₂₎ 4s and 4p, respectively, contribute 17.3% and 81.8% to the Ga₍₂₎-based orbital. Obviously, the 17.3% contribution from Ga₍₂₎ is not negligible because of the Ga₍₂₎ atom of the $GaAu_4^-$ unit. Au 6s and Ga₍₁₎ 4p provide the largest contributions to the $Ga_{(1)}-Au-Ga_{(2)}$ bridging bond in C_{3v} Ga_2Au_4 (**39**). This finding agrees with the ionic characteristic of $Au_{(t)}^+ [Ga_{(1)}(\mu-Au)_3Ga_{(2)}]^-$ presented earlier. Thus, in contrast to the orbital combination in Ga_2Au_n ($n = 1-3$), the bridging bond of C_{3v} Ga_2Au_4 (**39**) can be approximated as $\tau_{Ga(1)-Au-Ga(2)} = 0.40(p)_{Ga(1)} + 0.70(sd^{0.02})_{Au} + 0.59(sp^{4.73})_{Ga(2)}$. Similar 3c–2e orbital combinations exist in the corresponding anions. Compared with the bridging Au 3c–2e bond observed in electron-deficient systems (B_2Au_n , Al_2Au_n , and Ga_2Au_n), we found that bridging Au provides greater contributions to dialuminum and digallium aurides (70%–68%) than to

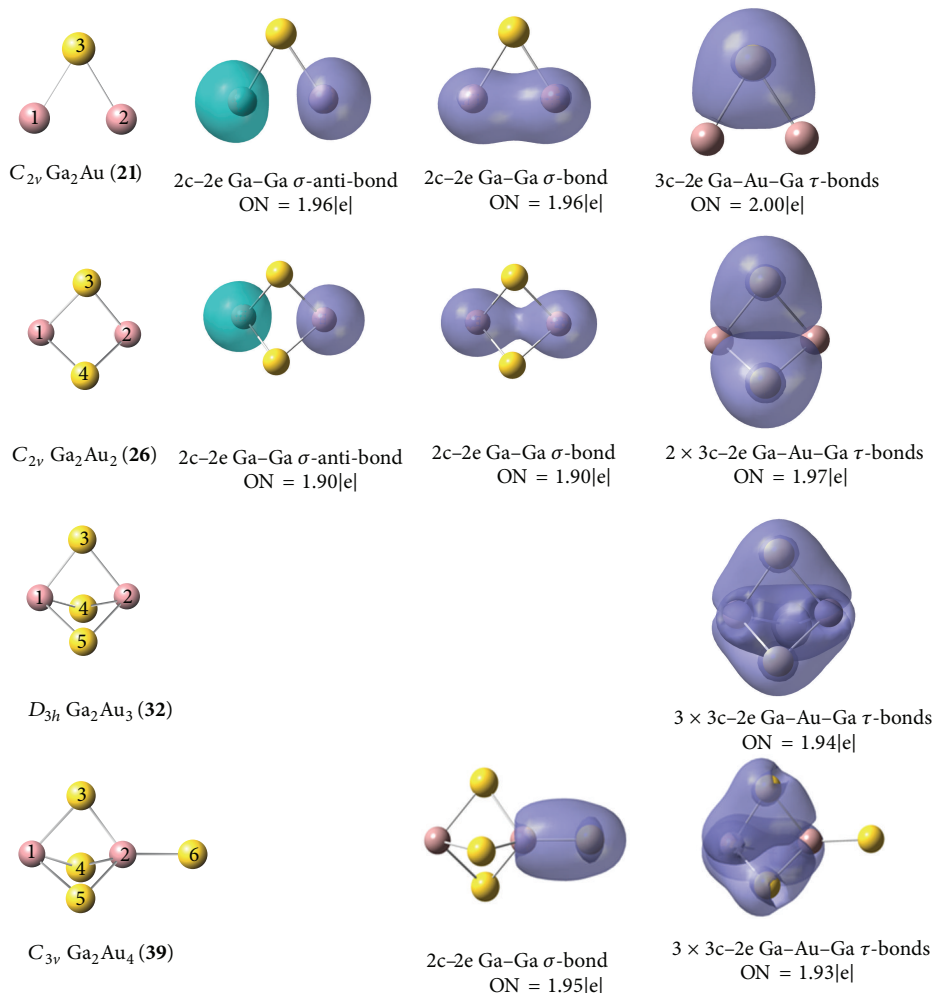


FIGURE 5: AdNDP bonding patterns of Ga_2Au (21), Ga_2Au_2 (26), Ga_2Au_3 (32), and Ga_2Au_4 (39). Occupation numbers (ON) are also indicated.

TABLE 2: Calculated ADEs (eVs) and VDEs (eV) of digallium auride anions at the B3LYP and CCSD(T)//B3LYP levels. The ADEs of the anions are equivalent to the electron affinities of the corresponding neutrals.

| | ADE | | VDE | |
|---|-----------------------|-----------------------|-----------------------|-----------------------|
| | B3LYP | CCSD(T) | B3LYP | CCSD(T) |
| 1 $C_{\infty v}$ $GaAu^-$ ($^2\Sigma^+$) | 0.64 ($^1\Sigma^+$) | 0.30 ($^1\Sigma^+$) | 0.66 ($^1\Sigma^+$) | 0.60 ($^1\Sigma^+$) |
| 5 C_{2v} $GaAu_2^-$ (1A_1) | 2.51 (2B_2) | 2.33 (2B_2) | 2.75 (2B_2) | 2.72 (2B_2) |
| 9 D_{3h} $GaAu_3^-$ ($^2A_1'$) | 1.99 ($^1A_1'$) | 1.56 ($^1A_1'$) | 2.10 ($^1A_1'$) | 1.86 ($^1A_1'$) |
| 13 T_d $GaAu_4^-$ (1A_1) | 3.23 ($^2A'$) | 3.07 (2T_2) | 3.95 ($^2A'$) | 4.17 (2T_2) |
| 18 C_{2v} Ga_2Au^- (3B_1) | 1.47 (2B_1) | 1.47 (2B_1) | 1.49 (2B_1) | 1.50 (2B_1) |
| 23 C_{2v} $Ga_2Au_2^-$ (2A_1) | 1.45 (1A_1) | 1.46 (1A_1) | 1.50 (1A_1) | 1.52 (1A_1) |
| 29 D_{3h} $Ga_2Au_3^-$ ($^1A_1'$) | 2.39 ($^2A_1'$) | 2.13 ($^2A_1'$) | 2.67 ($^2A_1'$) | 2.60 ($^2A_1'$) |
| 35 C_{3v} $Ga_2Au_4^-$ (2A_1) | 1.96 (1A_1) | 1.55 (1A_1) | 2.06 (1A_1) | 1.87 (1A_1) |

diboron aurides (50%–45%). Specifically, Au 5d contributes less than 2% to the Au-based orbital in dialuminum and digallium aurides.

3.5. Electron Detachment Energies. The ADE and VDE values of the anions were calculated in PES experiments. As shown in Table 2, the B3LYP and CCSD(T)//B3LYP levels produced

consistent one-electron detachment energies for $GaAu_n^-$ and $Ga_2Au_n^-$ ($n = 1-4$) anions. Except for C_{2v} $GaAu_2^-$ (5) and T_d $GaAu_4^-$ (13), D_{3h} $Ga_2Au_3^-$ (29), the calculated ADEs and VDEs at the CCSD(T) level lay at 0.30–1.87 eV. The small differences between ADE and VDE (0.03–0.32 eV) agree with the minor structural relaxation observed between the anion and the corresponding neutral molecule. At the same level,

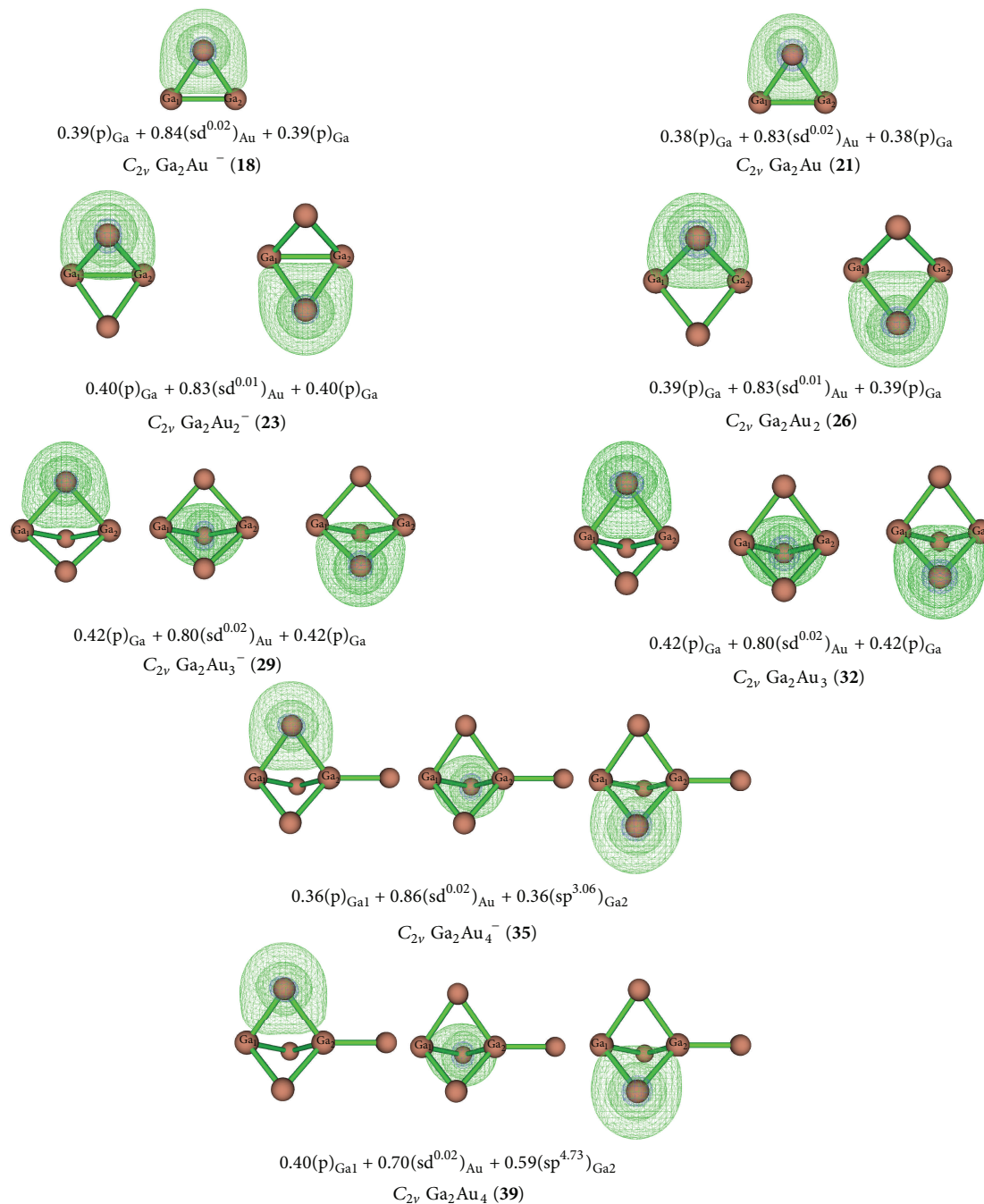


FIGURE 6: Isosurface maps and orbital combinations of 3c-2e bonds in Ga_2Au^- (18), Ga_2Au (21), Ga_2Au_2^- (23), Ga_2Au_2 (26), Ga_2Au_3^- (29), Ga_2Au_3 (32), Ga_2Au_4^- (35), and Ga_2Au_4 (39).

$C_{2v} \text{GaAu}_2^-$ (5) shows ADE = 2.33 eV and VDE = 2.72 eV. The difference between the ADE and VDE (0.39 eV) shows considerable structure relaxation between the C_{2v} anion (5) and the C_{2v} neutral molecule (7). A similar result was observed in $D_{3h} \text{Ga}_2\text{Au}_3^-$ (29). $T_d \text{GaAu}_4^-$ (13) anion has the calculated one-electron detachment energies of ADE = 3.07 eV and VDE = 4.17 eV at the CCSD(T)//B3LYP level. B3LYP approaches produced close ADE and VDE values with

CCSD(T). The extremely high electron detachment energies of $T_d \text{GaAu}_4^-$ indicate that GaAu_4 neutrals lie considerably higher than GaAu_4^- anions in energy, while the big ADE-VDE differences (0.72–1.10 eV) agree with the considerable structural relaxation from $T_d \text{GaAu}_4^-$ (13) and its closely related $C_s \text{GaAu}_4$ (16). The electron binding energies of these anions fall within the energy range of the conventional excitation laser (266 nm, 4.661 eV) in PES measurements.

4. Summary

This study presents geometric and electronic structural analyses of $\text{GaAu}_n^{0/-}$ and $\text{Ga}_2\text{Au}_n^{0/-}$ ($n = 1-4$) clusters based on DFT and wave function theory. The structure and bonding of a series of $\text{GaAu}_n^{0/-}$ ($n = 1-4$) with one Ga atom at the center are characterized. NRT, ELF, and NBO analyses show that Ga–Au interactions in the aurogalliums are highly polar covalent bonds with ionic characteristics. $\text{Ga}_2\text{Au}_n^{0/-}$ ($n = 1-4$) is predicted to possess highly symmetric ground states of C_{2v} $\text{Ga}_2\text{Au}_n^{0/-}$, C_{2v} $\text{Ga}_2\text{Au}_2^{0/-}$, D_{3h} $\text{Ga}_2\text{Au}_3^{0/-}$, and C_{3v} $\text{Ga}_2\text{Au}_4^{0/-}$. C_{3v} Ga_2Au_4 present strong interactions between a Ga^+ cation and the face of a tetrahedral GaAu_4^- anion. AdNDP and NLMO analyses demonstrate that a Ga–Au–Ga 3c–2e bond exists in these global minima. Detailed orbital analyses indicate that Au 6s and Ga 4p principally contribute to the Ga–Au–Ga bond in the Ga_2Au_n ($n = 1-3$) complex. In $\text{Ga}^+(\text{GaAu}_4)^-$ ionic conformers, besides Au 6s and cationic Ga 4p, tetrahedral Ga 4s and 4p also contribute significantly to the Ga–Au–Ga bond in Ga_2Au_4 ; here, the tetracoordinate unit has a greater influence than the cationic unit on the total 3c–2e orbital atomic contribution. The predicted ADE and VDE values of GaAu_n^- and Ga_2Au_n^- ($n = 1-4$) may facilitate future PES experiments to confirm these species. Bridging Au interactions addressed in this work provide an interesting bonding mode for covalent and ionic deficient systems and will help design new materials and catalysis with highly dispersed Au atoms.

Conflict of Interests

The authors declare that there is no conflict of interests regarding the publication of this paper.

Acknowledgments

This work was financially supported by the North China University of Water Conservancy and Electric Power High-Level Experts Scientific Research Foundation (no. 201114) and the Science and Technology Research Project of Henan Provincial Education Department (no. 14A150024). The computational resources utilized in this research were provided by Shanghai Supercomputer Center.

References

- [1] P. Pyykkö, “Relativity, gold, closed-shell interactions, and CsAu.NH_3 ,” *Angewandte Chemie International Edition*, vol. 41, no. 19, pp. 3573–3578, 2002.
- [2] F. A. Cotton, G. Wilkinson, C. A. Murillo, and M. Bochmann, *Advanced Inorganic Chemistry*, Wiley, New York, NY, USA, 6th edition, 1999.
- [3] H. Schwarz, “Relativistic effects in gas-phase ion chemistry: an experimentalist’s view,” *Angewandte Chemie: International Edition*, vol. 42, no. 37, pp. 4442–4454, 2003.
- [4] L. Gagliardi, “When does gold behave as a halogen? Predicted uranium tetraauride and other MAu_4 tetrahedral species, (M = Ti, Zr, Hf, Th),” *Journal of the American Chemical Society*, vol. 125, no. 25, pp. 7504–7505, 2003.
- [5] K. P. Hall and D. M. P. Mingos, “International tables for X-ray crystallography,” *Progress Inorganic Chemistry*, vol. 32, no. 5, pp. 237–325, 1984.
- [6] J. K. Burdett, O. Eisenstein, and W. B. Schweizer, “Are strong gold-gold interactions possible in main group $\text{XnA}(\text{AuPR}_3)_m$ molecules?” *Inorganic Chemistry*, vol. 33, no. 15, pp. 3261–3268, 1994.
- [7] B. Kiran, X. Li, H.-J. Zhai, L.-F. Cui, and L.-S. Wang, “ SiAu_4 : aurosilane,” *Angewandte Chemie: International Edition*, vol. 43, no. 16, pp. 2125–2129, 2004.
- [8] X. Li, B. Kiran, and L.-S. Wang, “Gold as hydrogen. An experimental and theoretical study of the structures and bonding in disilicon gold clusters Si_2Au_n^- and Si_2Au_n ($n = 2$ and 4) and comparisons to Si_2H_2 and Si_2H_4 ,” *Journal of Physical Chemistry A*, vol. 109, no. 19, pp. 4366–4374, 2005.
- [9] B. Kiran, X. Li, H.-J. Zhai, and L.-S. Wang, “Gold as hydrogen: Structural and electronic properties and chemical bonding in $\text{Si}_3\text{Au}_3^{+/0/-}$ and comparisons to $\text{Si}_3\text{H}_3^{+/0/-}$,” *Journal of Chemical Physics*, vol. 125, no. 13, Article ID 133204, 7 pages, 2006.
- [10] H.-J. Zhai, L.-S. Wang, D. Y. Zubarev, and A. I. Boldyrev, “Gold apes hydrogen: the structure and bonding in the planar B_7Au_2 and B_7Au_2 clusters,” *Journal of Physical Chemistry A*, vol. 110, no. 5, pp. 1689–1693, 2006.
- [11] Q. Chen, H.-J. Zhai, S.-D. Li, and L.-S. Wang, “On the structures and bonding in boron-gold alloy clusters: B_6Au_n^- and B_6Au_n ($n = 1-3$),” *Journal of Chemical Physics*, vol. 138, Article ID 084306, pp. 1–8, 2013.
- [12] H.-J. Zhai, C.-Q. Miao, S.-D. Li, and L.-S. Wang, “On the analogy of B–BO and B–Au chemical bonding in B_{11}O - and B_{10}Au -Clusters,” *Journal of Physical Chemistry A*, vol. 114, no. 46, pp. 12155–12161, 2010.
- [13] D. Y. Zubarev, J. Li, L.-S. Wang, and A. I. Boldyrev, “Theoretical probing of deltahedral closo-auroboranes $\text{B}_x\text{Au}_x^{2-}$ ($X = 5-12$),” *Inorganic Chemistry*, vol. 45, no. 14, pp. 5269–5271, 2006.
- [14] J. W. Lauher and K. Wald, “Gold derivatives as structural analogs of hydrides,” *Journal of American Chemical Society*, vol. 103, no. 25, pp. 7648–7650, 1981.
- [15] A. Grohmann, J. Riede, and H. Schmidbaur, “Electron-deficient bonding at pentacoordinate nitrogen,” *Nature*, vol. 345, no. 2, pp. 140–142, 1990.
- [16] G. Feng, C.-F. Huo, C.-M. Deng et al., “Isopropanol adsorption on $\gamma\text{-Al}_2\text{O}_3$ surfaces: a computational study,” *Journal of Molecular Catalysis A: Chemical*, vol. 304, no. 1-2, pp. 58–64, 2009.
- [17] O. D. Häberlen, H. Schmidbaur, and N. Rösch, “Stability of main-group element-centered gold cluster cations,” *Journal of the American Chemical Society*, vol. 116, no. 18, pp. 8241–8248, 1994.
- [18] P. Pyykkö and Y. Zhao, “Relativistic pseudopotential calculation of bonding trends in XAu_m+n clusters ($X = \text{B} - \text{N}$, $\text{Al} - \text{S}$; $n = 4 - 6$),” *Chemical Physics Letters*, vol. 177, no. 1, pp. 103–106, 1991.
- [19] R. Ma and Y. Bando, “Uniform MgO nanobelts formed from in situ Mg_3N_2 precursor,” *Chemical Physics Letters*, vol. 370, no. 5-6, pp. 770–773, 2003.
- [20] D.-Z. Li and S.-D. Li, “An Ab initio theoretical investigation on the geometrical and electronic structures of $\text{BAu}_n^{0/-}$ ($n = 1-4$) clusters,” *International Journal of Quantum Chemistry*, vol. 111, no. 15, pp. 4418–4424, 2011.

- [21] W.-Z. Yao, D.-Z. Li, and S.-D. Li, "Bridging gold: B-Au-B three-center-two-electron bonds in electron-deficient $B_2Au_n^{-/0}$ ($n = 1, 3, 5$) and mixed analogues," *Journal of Computational Chemistry*, vol. 32, no. 2, pp. 218–225, 2011.
- [22] W.-Z. Yao, J.-B. Yao, X.-B. Li, and S.-D. Li, " $B_2Au_2^{0/-/2-}$: multiple boron-boron bonds in diboron aurides," *Acta Physico-Chimica Sinica*, vol. 29, no. 6, pp. 1219–1224, 2013.
- [23] W.-Z. Yao, J.-B. Yao, and S.-D. Li, "Ab Initio theoretical investigation on the geometrical and electronic structures of $AlAu_n^{-/0}$ ($n = 2-4$) clusters," *Chinese Journal of Structural Chemistry*, vol. 31, no. 11, pp. 1549–1556, 2012.
- [24] W.-Z. Yao, B.-T. Liu, Z.-H. Lu, and S.-D. Li, "Bridging gold in electron-deficient $Al_2Au_n^{0/-}$ and $BAlAu_n^{0/-}$ ($n = 1-3$) clusters," *Journal of Physical Chemistry A*, vol. 117, no. 24, pp. 5178–5183, 2013.
- [25] B. Silvi and A. Savin, "Classification of chemical bonds based on topological analysis of electron localization functions," *Nature*, vol. 371, no. 6499, pp. 683–686, 1994.
- [26] A. D. Becke and K. E. Edgecombe, "A simple measure of electron localization in atomic and molecular systems," *Journal of Chemical Physics*, vol. 92, no. 9, pp. 5397–5403, 1990.
- [27] D. Y. Zubarev and A. I. Boldyrev, "Developing paradigms of chemical bonding: adaptive natural density partitioning," *Physical Chemistry Chemical Physics*, vol. 10, no. 34, pp. 5207–5217, 2008.
- [28] A. D. Becke, "Density-functional thermochemistry. III. The role of exact exchange," *The Journal of Chemical Physics*, vol. 98, no. 7, pp. 5648–5652, 1993.
- [29] C. Lee, W. Yang, and R. G. Parr, "Development of the Colle-Salvetti correlation-energy formula into a functional of the electron density," *Physical Review B*, vol. 37, no. 2, pp. 785–789, 1988.
- [30] M. Head-Gordon, J. A. Pople, and M. J. Frisch, "MP2 energy evaluation by direct methods," *Chemical Physics Letters*, vol. 153, no. 6, pp. 503–506, 1988.
- [31] M. Head-Gordon and T. Head-Gordon, "Analytic MP2 frequencies without fifth-order storage: theory and application to bifurcated hydrogen bonds in the water hexamer," *Chemical Physics Letters*, vol. 220, no. 1-2, pp. 122–128, 1994.
- [32] G. E. Scuseria and H. F. Schaefer III, "Is coupled cluster singles and doubles (CCSD) more computationally intensive than quadratic configuration interaction (QCISD)?" *The Journal of Chemical Physics*, vol. 90, no. 7, pp. 3700–3703, 1989.
- [33] J. M. L. Martin and A. Sundermann, "Correlation consistent valence basis sets for use with the Stuttgart-Dresden-Bonn relativistic effective core potentials: the atoms Ga-Kr and In-Xe," *Journal of Chemical Physics*, vol. 114, no. 8, pp. 3408–3420, 2001.
- [34] R. A. Kendall, T. H. Dunning Jr., and R. J. Harrison, "Electron affinities of the first-row atoms revisited: systematic basis sets and wave functions," *Journal of Chemical Physics*, vol. 96, no. 9, pp. 6796–6806, 1992.
- [35] M. J. Frisch, G. W. Trucks, H. B. Schlegel et al., *Gaussian 09, Revision B.01*, Gaussian, Inc., Wallingford, Conn, USA, 2010.
- [36] T. Lu and F. Chen, "Multiwfn: a multifunctional wavefunction analyzer," *Journal of Computational Chemistry*, vol. 33, no. 5, pp. 580–592, 2012.
- [37] E. D. Glendening, J. K. Badenhoop, A. E. Reed et al., *NBO 5.0*, Theoretical Chemistry Institute: University of Wisconsin, Madison, Wis, USA, 2001.
- [38] X. F. Wang and L. Andrews, "Infrared spectra of gallium hydrides in solid hydrogen: $GaH_{1,2,3}$, $Ga_2H_{2,4,6}$ and the $GaH_{2,4}^-$ anions," *Journal of Physical Chemistry A*, vol. 107, no. 51, pp. 11371–11379, 2003.
- [39] K. Lammertsma and J. Leszczyński, "Ab initio study on digallane(4), Ga_2H_4 ," *Journal of Physical Chemistry*, vol. 94, no. 14, pp. 5543–5548, 1990.

Research Article

Microstructure and Thermal Properties of Polypropylene/Clay Nanocomposites with $\text{TiCl}_4/\text{MgCl}_2/\text{Clay}$ Compound Catalyst

Limei Wang¹ and Aihua He²

¹Key Laboratory of Coordination Chemistry and Functional Materials in Universities of Shandong, College of Chemistry and Chemical Engineering, Dezhou University, Dezhou 253023, China

²Key Laboratory of Rubber-Plastics (Ministry of Education), School of Polymer Science and Engineering, Qingdao University of Science and Technology, Qingdao 266042, China

Correspondence should be addressed to Limei Wang; wlm916@126.com

Received 16 October 2014; Accepted 24 December 2014

Academic Editor: Baowang Lu

Copyright © 2015 L. Wang and A. He. This is an open access article distributed under the Creative Commons Attribution License, which permits unrestricted use, distribution, and reproduction in any medium, provided the original work is properly cited.

Polypropylene (PP)/clay nanocomposites were synthesized by in situ intercalative polymerization with $\text{TiCl}_4/\text{MgCl}_2/\text{clay}$ compound catalyst. Microstructure and thermal properties of PP/clay nanocomposites were studied in detail. Fourier transform infrared (FTIR) spectra indicated that PP/clay nanocomposites were successfully prepared. Both wide-angle X-ray diffraction (XRD) and transmission electron microscopy (TEM) examination proved that clay layers are homogeneously distributed in PP matrix. XRD patterns also showed that the α phase was the dominate crystal phase of PP in the nanocomposites. Thermogravimetric analysis (TGA) examinations confirmed that thermal stability of PP/clay nanocomposites was markedly superior to pure PP. Differential scanning calorimetry (DSC) scans showed that the melt temperature and the crystallinity of nanocomposites were slightly lower than those of pure PP due to crystals imperfections.

1. Introduction

Since the nylon-6/clay nanocomposites with some excellent properties [1–4], such as enhanced mechanical properties [1, 2], increased heat distortion temperature, and decreased gas/vapor permeability [3], were successfully prepared by Toyota researchers in the late 1980s [4], many researchers from both academic and industrial labs have been focused on the polymer/clay nanocomposites [5–8].

Polypropylene (PP), as one of the most widely used plastics, possesses a relatively high performance-to-price ratio. However, inferior properties of PP, such as toughness [9], thermal stability, and barrier properties [10], hinder its application as high performance materials and special materials. Clay is one of very abundant phyllosilicate resources [11]. To improve PP properties, clay layers were hoped to disperse uniformly in PP matrix, exerting its rigidity, heat resistance, and dimension stability. However, it is difficult to prepare exfoliated PP/clay nanocomposites because of the incompatibility of hydrophobic PP and hydrophilic clay.

In order to improve the compatibility of clay and PP, surfactants have been used to modify clay [12]. However, it was found that some surfactants at the PP processing temperature not only accelerated the aging and decomposition of PP [13], but also led to the restacking of the silicate sheets [14]. Therefore, the design of surfactants with higher thermal stability is becoming more and more crucial.

In our previous work, 1-hexadecane-3-methylimidazolium bromine with relatively high thermal stability had been designed and synthesized as clay modification surfactants. Organically modified clay was used to prepare $\text{TiCl}_4/\text{MgCl}_2/\text{clay}$ compound catalyst by chemical reaction method and PP/clay composites were successfully synthesized by intercalative polymerization. Effects of polymerization conditions, such as temperature and time, on activity and catalytic stereospecificity of compound catalyst were studied in detail [15].

In this paper, the microstructure and thermal properties of PP/clay nanocomposites were studied at length. Fourier transform infrared (FTIR) was used to clarify the dispersion

of clay layers in PP matrix. The dispersion of clay layers in PP matrix was investigated by wide-angle X-ray diffraction (XRD) patterns and transmission electron microscopy (TEM). The thermal stability of PP/clay nanocomposites was estimated by thermogravimetric analysis (TGA). The melting process and nonisothermal crystallization kinetics of PP/clay nanocomposites were tested by differential scanning calorimetry (DSC).

2. Experimental

2.1. Materials. Clay was supplied by Zhangjiakou Qinghe Chemical Factory with 90~100 mmol/100 g cation exchange capacity (CEC). 1-Methylimidazole, 1-bromohexadecane (>95% purity), and diphenyldimethoxylenesilane (DDS, >95% purity) were purchased from Sigma-Aldrich Co. Anhydrous magnesium dichloride (MgCl_2 , >95% purity) was kindly supplied by Yingkou Science Chemical Co. Titanium tetrachloride (TiCl_4) was supplied by Beijing Yili Fine Chemicals Limited Co. Toluene (Beijing Chemical Factory) was refluxed continuously over Na under argon for 24 h and was withdrawn from the still immediately before use. Triethylaluminum (AlEt_3) and propylene were supplied by Yanshan Petrochemical Co. Argon (99.99% purity) was dried by passing it over a P_2O_5 column.

FTIR spectra were analyzed with a Perkin-Elmer System 2000 Fourier transform infrared in a wave number range of 4000–400 cm^{-1} . FTIR spectra were obtained on samples mixed with KBr and molded into pellicle. XRD analysis was performed on a Japan Rigaku D/max-2500 diffractometer with $\text{Cu K}\alpha$ radiation ($\lambda = 0.1540 \text{ nm}$) at a generator voltage of 40 kV and generator current of 100 mA. Scanning was performed in a step of 0.02° at a speed of $2^\circ/\text{min}$. The interlayer spacing (d_{001}) of clay was calculated in accordance with the Bragg equation: $2d \cdot \sin \theta = \lambda$. TEM was carried out on a Jeol JEM 2010 transmission electron microscope using an acceleration voltage of 100 kV. Samples for TEM were prepared by molding into specimens at 200°C and turned into ultrathin membrane by plasma cutting. TGA was performed with Perkin-Elmer TGA at a heating rate of $20^\circ\text{C}/\text{min}$ under nitrogen atmosphere. DSC was conducted using a Perkin-Elmer DSC-7 thermal analyzer under nitrogen atmosphere with a heating rate of $10^\circ\text{C}/\text{min}$ in a temperature range of 40– 200°C for dynamic scanning, and melting enthalpy (ΔH_m) and melting temperature (T_m) were determined in the second scan. The crystallinity (X_c) was calculated with the following equation:

$$X_c = \Delta H_m \times \frac{100\%}{[\Delta H^* \times (1 - \text{wt.}\% (\text{MMT}))]}, \quad (1)$$

where ΔH^* is melting enthalpy of PP whose crystallinity is 100%, equal to 240.5 J/g [8].

2.2. Synthesis of $\text{TiCl}_4/\text{MgCl}_2/\text{Clay}$ Compound Catalyst. Synthesis of 1-hexadecane-3-methylimidazolium bromine, preparation of organically modified clay, and preparation of $\text{TiCl}_4/\text{MgCl}_2/\text{clay}$ compound catalyst are as described in [15].

2.3. Preparation of PP/Clay Nanocomposites. 2000 mL stainless autoclave was degassed and purified with propylene, and then toluene, AlEt_3 , DDS, and the pretreated catalyst slurry or powder were added successively to start polymerization. After predetermined reaction time, polymerization was quenched with diluted hydrochloric solution of ethanol. Composites (PP1 and PP2) were washed with ethanol three times, filtered, and dried in a vacuum oven at 70°C for 8 h.

3. Results and Discussion

3.1. Characterization of PP in PP/Clay Nanocomposites. PP was synthesized with $\text{TiCl}_4/\text{MgCl}_2/\text{clay}$ compound catalyst in combination with AlEt_3 as cocatalyst and DDS as an external donor in the slurry phase batch process. Some atactic activity centres can turn inactive because of DDS as an external donor in the slurry polymerization [16]. PP obtained in PP/clay nanocomposites might be stereospecific PP. Isotactic index (I.I) of PP was carried out as follows: 1-2 g dried PP/clay nanocomposites were wrapped with the filter paper. The package was extracted with boiling normal heptane for 10 h in Soxhlet's extractor and was dried in a vacuum oven until its mass was constant. Isotactic index was calculated with the following equation:

$$\text{I.I} = (w_3 - w_1) \times \frac{100\%}{(w_2 - w_1)}, \quad (2)$$

where w_1 is the weight of the dried filter paper, w_2 is the weight of PP/clay nanocomposites and the filter paper, and w_3 is the weight of package after being extracted and dried. On average, the I.I value of PP obtained in composites was 94%, which was close to I.I of PP synthesized by the commercial CS-2 catalyst (98%), indicating that PP obtained is high isotacticity PP.

3.2. Structure Characterization of the PP/Clay Nanocomposites. To prove clay in the resulting PP matrix, an infrared dichroism technique was carried out. Figure 1 shows the FTIR spectra of the PP/clay nanocomposites. The absorption bands at 1460 cm^{-1} and 1375 cm^{-1} are C–H bending vibration of PP. The broad peak around 3000 cm^{-1} is C–H symmetrical stretching and anamorphic vibration. It also can be seen that dual kurtosis of Si–O stretching vibration of clay appears at 1095 cm^{-1} and 1035 cm^{-1} , and bending vibration bands of Si–O–Fe and Si–O–Mg appear at 463 cm^{-1} and 515 cm^{-1} . The results revealed that the PP/clay composites were successfully prepared.

XRD was used to prove the dispersion of clay sheets in PP matrix. Figure 2 shows XRD patterns of PP/clay composites. The XRD patterns display no (001) diffraction peak from the clay, indicating that the average interlayer spacing of the clay in PP/clay nanocomposites is larger than 5.8 nm according to the Bragg equation and indicating that the silicate layers of clay are fully exfoliated during in situ intercalative polymerization. At the same time, it could be seen from Figure 2 that the diffraction peaks at $2\theta = 13.9, 16.8, 18.4,$ and 21.8 corresponded to the planes (110), (040), (130), and (111) of α -phase crystallite, respectively. α -phase

TABLE 1: Thermal properties of PP/clay nanocomposites.

| Run | T_m ($^{\circ}\text{C}$) | H_m (J/g) | T_c ($^{\circ}\text{C}$) | H_c (J/g) | $T_{0.01}$ ($^{\circ}\text{C}$) | $T_{0.05}$ ($^{\circ}\text{C}$) | T_{onset} ($^{\circ}\text{C}$) |
|-----|------------------------------|-------------|------------------------------|-------------|-----------------------------------|-----------------------------------|---|
| PP0 | 162.8 | 100 | 117.2 | 98 | 298.6 | 330 | 379 |
| PP1 | 158.7 | 82.7 | 116.5 | 82.3 | 308.8 | 343.6 | 443.2 |
| PP2 | 160.0 | 80.8 | 118.3 | 80.3 | 323.0 | 366.3 | 452.3 |

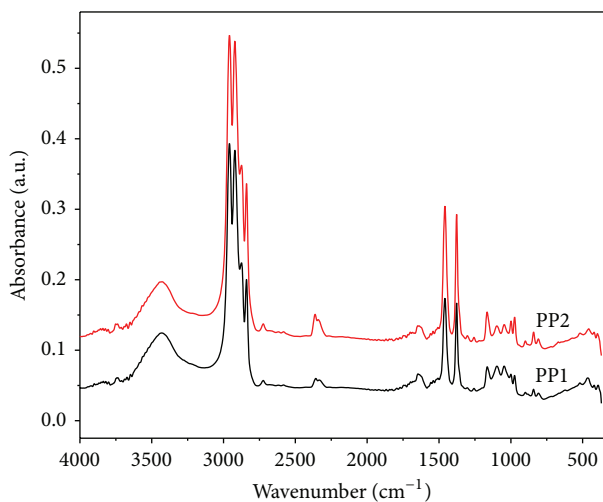


FIGURE 1: FTIR spectra of PP/clay nanocomposites.

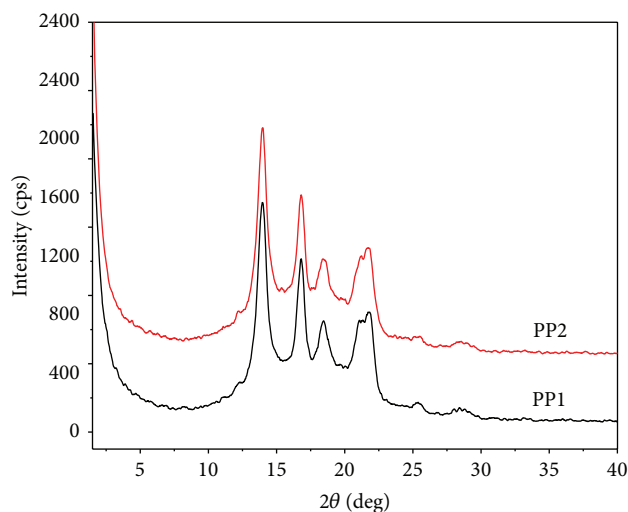


FIGURE 2: XRD patterns of PP/clay nanocomposites.

crystallite was still the main crystallite of PP in PP/clay nanocomposites. Diffraction peaks of β -phase and γ -phase crystallite were not observed in XRD patterns of PP/clay nanocomposites. This conclusion agreed with former work, and the dominate crystal phase of PP did not change because of the change of imidazolium and the existence of clay [8].

However, TEM is a powerful technique to prove the extent of silicate dispersion. Figure 3 shows TEM image of PP/clay nanocomposites. The TEM micrograph showed that the silicate layers were well dispersed in the whole PP



FIGURE 3: TEM image of PP/clay nanocomposites.

matrix. The average thickness of the clay layers was less than 20 nm, corresponding to about 10 silicate layers of stacking. It could be concluded from TEM measurements that exfoliated PP/clay nanocomposites were prepared via in situ polymerization.

3.3. Thermal Properties of PP/Clay Nanocomposites. DSC is a technique used to study what happens to the nanocomposites when they are heated. Figure 4 shows DSC curves of PP/clay nanocomposites and pure PP, and Table 1 lists the data of thermal properties of PP/clay nanocomposites. It can be seen in Figure 4 and Table 1 that the melting temperature (T_m) of PP/clay nanocomposites is about 160°C , slightly lower than 162.8°C of pure PP, indicating an increase of crystals imperfections because of the presence of clay layers. The degree of crystallization (X_c) of PP/clay nanocomposites was lower than that of pure PP, as shown in Table 1, which also proved the existence of crystals imperfections. However, the crystallization temperature (T_c) of nanocomposites was 116.5°C to 118.3°C , close to 117.2°C of pure PP (PP0).

Thermal stability of PP/clay nanocomposites was measured by using TGA. Figure 5 shows the TGA curves of PP/clay nanocomposites and pure PP. The initial decomposition temperature (temperature at 1 wt.% weight loss $T_{0.01}$ and temperature at 5 wt.% weight loss $T_{0.05}$) and the maximum decomposition temperature (T_{onset}) were shown in Table 1. In comparison of the thermal decomposition temperature of PP/clay nanocomposites (PP1 and PP2) with that of pure PP (PP0), the thermal stability of PP/clay nanocomposites was much higher than that of pure PP. In a word, the effect of

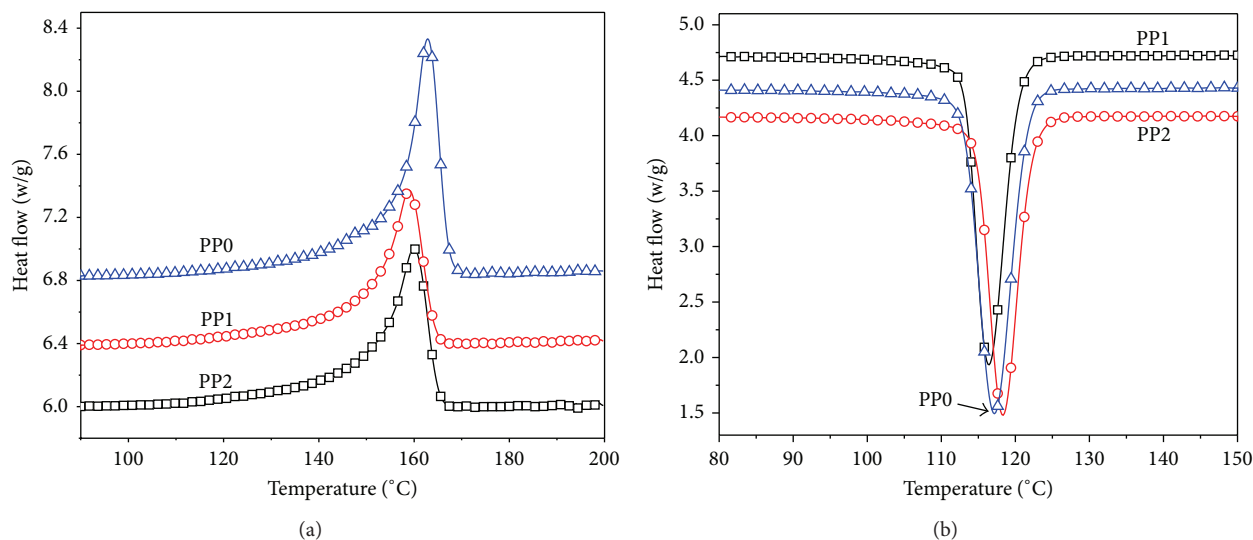


FIGURE 4: DSC curves of pure PP and PP/clay nanocomposites: (a) DSC heating thermograms; (b) DSC cooling thermograms.

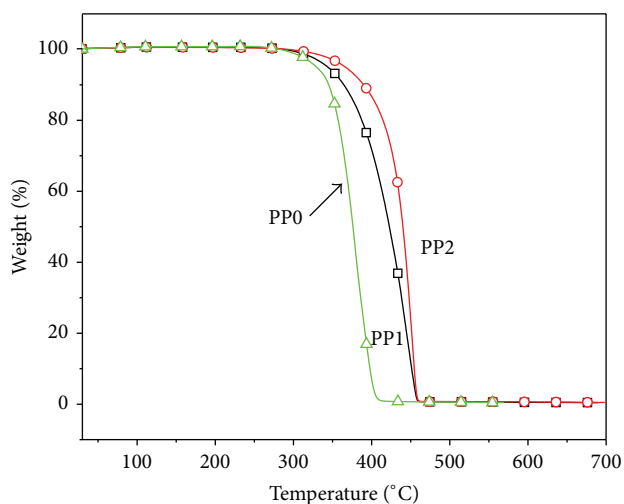


FIGURE 5: TGA curves of pure PP and PP/clay nanocomposites.

clay on the thermal stability of the nanocomposites was much pronounced.

4. Conclusions

PP/clay composites were successfully synthesized by in situ intercalative polymerization with $\text{TiCl}_4/\text{MgCl}_2/\text{clay}$ compound catalyst, in accordance with FTIR spectra. XRD patterns and TEM image showed that clay layers in composites were exfoliated into nanometer size and dispersed uniformly in the PP matrix. The clay enhanced the thermal stability of PP materials. PP obtained in the nanocomposites had high isotacticity. The effect of clay on melting temperature and the crystallization temperature of PP/clay nanocomposites was slight.

Conflict of Interests

The authors declare that there is no conflict of interests regarding the publication of this paper.

Acknowledgments

The authors are grateful to the National Natural Science Foundation of China (nos. 20774098 and 51273033), Shandong University Technology Research Development Programme of China (no. J13LE12), Shandong Dezhou Science and Technology Projects of China (no. 2012B13), and Shandong Provincial Engineering Laboratory of Novel Pharmaceutical Excipients, Sustained and Controlled Release Preparations (no. 311713).

References

- [1] Y. Kojima, A. Usuki, M. Kawasumi et al., "Mechanical properties of nylon 6-clay hybrid," *Journal of Materials Research*, vol. 8, no. 5, pp. 1185–1189, 1993.
- [2] A. Oya, Y. Kurokawa, and H. Yasuda, "Factors controlling mechanical properties of clay mineral/polypropylene nanocomposites," *Journal of Materials Science*, vol. 35, no. 5, pp. 1045–1050, 2000.
- [3] J. W. Gilman, "Flammability and thermal stability studies of polymer layered-silicate (clay) nanocomposites," *Applied Clay Science*, vol. 15, no. 1-2, pp. 31–49, 1999.
- [4] A. Okada and M. Kawasumi, "Synthesis and characterization of a nylon 6-clay hybrid," *Polymeric Preprints*, vol. 28, no. 2, pp. 447–448, 1987.
- [5] S. S. Sinha Ray and M. Okamoto, "Polymer/layered silicate nanocomposites: a review from preparation to processing," *Progress in Polymer Science*, vol. 28, no. 11, pp. 1539–1641, 2003.
- [6] Y. J. Huang, K. F. Yang, and J. Y. Dong, "Copolymerization of ethylene and 10-undecen-1-ol using a montmorillonite-intercalated metallocene catalyst: synthesis of polyethylene/montmorillonite nanocomposites with enhanced structural

- stability,” *Macromolecular Rapid Communications*, vol. 27, no. 15, pp. 1278–1283, 2006.
- [7] A. He, H. Hu, Y. Huang, J. Y. Dong, and C. C. Han, “Isotactic poly(propylene)/monoalkylimidazolium-modified montmorillonite nanocomposites: preparation by intercalative Polymerization and Thermal Stability Study,” *Macromolecular Rapid Communications*, vol. 25, no. 24, pp. 2008–2013, 2004.
- [8] L.-M. Wang, A.-H. He, K. Du, Y.-Q. Huang, J.-Y. Dong, and Z.-C. Han, “Structure characterization and physical properties of exfoliated polypropylene/montmorillonite nanocomposites synthesized via in situ polymerization,” *Journal of Chemical Engineering of Chinese Universities*, vol. 24, no. 1, pp. 132–137, 2010.
- [9] F. Rault, C. Campagne, M. Rochery, S. Giraud, and E. Devaux, “Polypropylene multifilament yarn filled with clay and/or graphite: study of a potential synergy,” *Journal of Polymer Science, Part B: Polymer Physics*, vol. 48, no. 11, pp. 1185–1195, 2010.
- [10] H. Qiao, Y. Cai, F. Chen et al., “Influences of organic-modified Fe-montmorillonite on structure, morphology and properties of polyacrylonitrile nanocomposite fibers,” *Fibers and Polymers*, vol. 10, no. 6, pp. 750–755, 2010.
- [11] M. Kato, A. Usuki, and A. Okada, “Synthesis of polypropylene oligomer-clay intercalation compounds,” *Journal of Applied Polymer Science*, vol. 66, no. 9, pp. 1781–1785, 1997.
- [12] A. H. He, L. M. Wang, W. Yao, B. C. Huang, D. J. Wang, and C. C. Han, “Structural design of imidazolium and its application in PP/montmorillonite nanocomposites,” *Polymer Degradation and Stability*, vol. 95, no. 4, pp. 651–655, 2010.
- [13] M. Zanetti, G. Camino, P. Reichert, and R. Mülhaupt, “Thermal behaviour of poly(propylene) layered silicate nanocomposites,” *Macromolecular Rapid Communications*, vol. 22, no. 3, pp. 176–180, 2001.
- [14] H. L. Qin, S. M. Zhang, C. G. Zhao et al., “Thermal stability and flammability of polypropylene/montmorillonite composites,” *Polymer Degradation and Stability*, vol. 85, no. 2, pp. 807–813, 2004.
- [15] L.-M. Wang and A.-H. He, “Preparation of polypropylene/clay nanocomposites by in situ polymerization with $\text{TiCl}_4/\text{MgCl}_2$ /clay compound catalyst,” *Chinese Journal of Polymer Science*, vol. 29, no. 5, pp. 597–601, 2011.
- [16] X. J. Wen, M. Ji, L. Lu, H. Niu, and J. Y. Dong, “Progress in electron donor research for heterogeneous Ziegler-Natta catalysts of isotactic polypropylene,” *Chinese Polymer Bulletin*, no. 6, pp. 53–60, 2010.